# INFLUENCE OF SURROUNDING BOUNDARY WALLS ON THE EXTERNAL WIND PRESSURE OF A LOW-RISE GABLE-ROOFED BUILDING

Don Pasindu Piumal Meddage

208044E

Degree of Master of Science

Department of Civil Engineering

University of Moratuwa

Sri Lanka

June 2021

# INFLUENCE OF SURROUNDING BOUNDARY WALLS ON THE EXTERNAL WIND PRESSURE OF A LOW-RISE GABLE-ROOFED BUILDING

Don Pasindu Piumal Meddage

208044E

Thesis submitted in partial fulfillment of the requirements for the degree Master of Science in Civil Engineering

Department of Civil Engineering

University of Moratuwa

Sri Lanka

June 2021

## DECLARATION

I hereby witness that this thesis represents my original research work conducted after registration for the degree of M.Sc. at the Department of Civil Engineering, University of Moratuwa. It has not been submitted elsewhere or for any degree or diploma and the collaborative contributions and previous work related to the current study have been stated and properly acknowledged.

Also, I hereby grant a non-exclusive right to the University of Moratuwa and its agents to archive and make accessible this dissertation, in whole or in part in print electronic, or another medium. However, I retain all the ownership to use this content in whole or part in publications (Article/ Book).

Signature: Date: 10.06.2021

The above candidate has carried out research for the Masters under my supervision

Name of the supervisor: Dr. C. S. Lewangamage

Signature of the supervisor: Date: 10.06.2021

Name of the supervisor: Dr. A. U. Weerasuriya

Signature of the supervisor: *UOM Verified Signature* Date: 10.06.2021

## ACKNOWLEDGEMENT

Foremost, gratitude should be given to my postgraduate supervisors, Dr. C. S. Lewangamage and Dr. A. U. Weerasuriya for advice and criticism throughout the research work. Dr. C.S. Lewangamage has contributed to the wind tunnel study and Dr. A. U. Weerasuriya provided expert advice on CFD modelling. Their immense support was the main pillar of success in this research. Further, I would like to thank Prof. M. T. R. Jayasinghe, who encouraged me to research studies.

This research study was funded by National Science Foundation, Sri Lanka, through grant No. OSTP/2019/17. We are much grateful to the technical staff at the Cyclone testing station, James Cook University, Townsville, Australia for facilitating the wind tunnel experiment. As well, Prof.John Ginger and Dr. Korah Parackal for providing expert advice on wind tunnel modeling sequence. In addition, the advice given by Prof. John Holmes was helpful for this research study.

Head, Department of Civil Engineering Prof. Athula Kulathilaka should be mentioned who allowed us required facilities to be used during the research work. I would like to convey my gratefulness to Eng. Imesh Ekanayake and Eng. Sahan Wickramage for assisting me with the research work.

Finally, I wish to thank my parents and my friends who gave me their wholehearted support throughout the research project.

D. P. P. Meddage

Department of civil engineering

University of Moratuwa

## ABSTRACT

Low-rise structures are not often subjected to rigorous structural analysis, despite their omnipresence. Estimating wind loads on low buildings is moderately complicated compared to high-rise structures due to the effect of the roughness layer. Therefore, an accurate modelling sequence is required to obtain reliable results. Recent wind tunnel experiments revealed that the interference of surroundings affects the wind pressure characteristics in contrast to the isolated environment. Compared to large-scale objects, smaller objects have been given relatively less attention. One such example is a boundary wall that obstructs the wind flow, forming a wake behind. This research presents a detailed analysis of the effect of boundary walls on external pressure coefficients of low-rise gable-roofed buildings. Wind tunnel experiments were conducted on 1/50 scaled-down gable-roofed low-rise buildings. It was observed, the mean and peak pressure tend to decrease particularly near the perimeter zones at eaves' height in the presence of boundary walls. Moreover, a reduction was observed in the intensity of diagonal vortices formed along with oblique wind attacks. Interestingly, the boundary walls not only altered the magnitude of external pressure but also its variation, notably. The wind tunnel results were in good agreement with the performed CFD modelling. There it directs to revise current wind loading standards related to low-rise buildings, considering provisions on shielding effect in the presence of boundary walls.



**Keywords:** Low-rise gable-roofed building, Boundary wall, Wind tunnel test, External pressure coefficient

# TABLE OF CONTENTS

## LIST OF FIGURES

## LIST OF TABLES

## LIST OF ABBREVIATIONS

$\overline{C_P}$ – Mean pressure coefficient

$\widehat{C_P}$ – Maximum pressure coefficient

$\widetilde{C_P}$ – Minimum pressure coefficient

$C_{\sigma P}$– RMS pressure coefficient

ABL – Atmospheric Boundary Layer

CFD – Computational Fluid Dynamics

GEV – Generalized Extreme Value

EV – Extreme Value

ACC – Auto Correlation Coefficient

LES – Large Eddy Simulation

RANS – Reynolds Averaged Navier Stokes

FS – Full Scale

DAD – Database Assist Design

WOW – Wall of Wind

ASCE- American Society of Civil Engineers

TTU- Texas Tech University

TPU- Tokyo Polytechnic University

ASHRAE-American Society of Heating, Refrigeration and Air-conditioning Engineers

NIST- National Institute of Standards and Technology

BM- Base Model (Without Boundary walls)

BW1- Boundary Wall 01

BW2- Boundary Wall 02

BW3- Boundary Wall 03

Re – Reynolds Number

Gu- Gust Effect Factor

$I_{uu}$ – Longitudinal Turbulence Intensity

$I_{vv}$ – Lateral Turbulence Intensity

$I_{ww}$ – Vertical Turbulence Intensity

$Z_G$ – Gradient Height

ME – Mean Error

MAE – Mean Absolute Error

RMSE – Root Mean Square Error

$R^2$ – Coefficient of Determination

R – Coefficient of Correlation (Pearson Correlation Coefficient)

SI – Scatter Index

AIC –Akaike Information Criteria

$C_s$ – Sand grain roughness

UDF – User Defined Function

## ANNEXURE

# 1. INTRODUCTION

## 1.1 General

Low-rise structures represent a larger proportion of infrastructure all over the world. Generally, low-rise buildings fall within the boundary layer of the earth. Therefore, it is rational to assume these buildings are subjected to steep velocity gradients and high turbulence. Further, it explains the highly fluctuating nature of wind loading acting on low-buildings. Geometry configurations include a wide range of varieties and wind pressure on the envelopes is spatially heterogeneous. However, the resonance response of low-buildings is not critical due to lower natural frequencies. Both wind and earthquake are the dominant environmental loading that deals with uncertainties. Even though these two have claimed for massive destruction, severe windstorms happen more often than earthquakes (Holmes, 2001). The aforementioned aspects make determining the wind loading on low-rise structures more comprehensive (Alrawashdeh & Stathopoulos, 2015).

Particularly, wind loading standards follow various definitions on low-rise buildings. ASCE (American Society of Civil Engineers) suggests the height limit for a low-rise structure to be 18.3 m. European and Australian and New Zealand standards consider the height should be less than 15 m and 25 m, respectively. Canadian provisions (NBCC 2015) states different values for the threshold height depending on the geometry.

## 1.2 Wind damage on low-buildings

Low-buildings are the single asset in the residential sector and serve commercial and other purposes as well. Therefore, large investments are involved in such structures in society. All over the world, wind damage on low structures reveals a wide range of potential (Jayasinghe, 2012). The structural failure mode and the breakdown are primarily due to their progressive nature. When the load path is considered, building cladding and components are the initial stages. Wind pressure is subsequently transferred to secondary components, structural framework, and the ground through

the foundation. The collapse might transform from localized damage to total collapse. Thus, smaller damages can involve a larger resolution especially due to the progressive initialization. Incoming turbulence, velocity profile, length scales, and geometric features can influence the above phenomena in various tones.

Severe windstorms are categorized as tropical cyclones, tornados, gales, and thunderstorms. Thunderstorms and tornados are short localized events that can be extended up to tens of kilometers. Cyclones are generally observed in the coastal regions and tropics, extending hundreds of kilometers. Case studies that were done in Australia, reported wind damage on the low-structures cannot be neglected (Boughton et al., 2011; Henderson et al., 2006; Leitch et al., 2010; Reardon et al., 1986; Walker, 1995). Boughton et al., (2011) emphasized the advancement in the designs and constructions could reduce the level of damage considerably. Full-scale experiments have identified usually the roof structure is highly susceptible to wind-induced damage. The local failure zones allow the wind to enter through the roof, increasing the inside pressure together with the roof suction particularly at perimeter regions. This can usually induce high lift forces ended up with total destruction. In addition, the damage surveys done by Walker, (1995) and the experimental data from (Boughton & Reardon, 1982, 1983, 1984) described the progressive failure initiated on roof structures.

In the events of severe storms, costly damages are highlighted where the engineers should pay due attention. Exposure to wind damage indicates the importance of adhering to design principles for these non-engineered structures. The proper idealization of wind effects is required to make low-buildings safe and economical.

### 1.3 Thesis background

There exist unaddressed issues by the wind engineering research community to provide specifications on generic low-buildings. Series wind-tunnel and full-scale experiments have been conducting, involving numerous geometric configurations (Holmes, 1983; Stathopoulos, 1984; Tieleman, 2003; Uematsu & Isyumov, 1999). In

the case of instrumentation and field constraints, wind tunnel experiments have definite advantages over full-scale tests. However, most of the wind tunnel tests on low-buildings have been conducted in an isolated environment. It was investigated, the deviation of pressure characteristics according to different heights, plan dimensions, roof pitches, and internal openings. The wind direction had a significant impact on the pressure distribution especially, in the perimeter zones (Jayasinghe, 2012).

On the other hand, several authors highlighted the importance of surrounding interference to the effective pressure distribution. Detailed explanations of the above factors are presented in chapter two. Subsequently, the experiments changed from seldom configurations to a complex environment. A disagreement among the results existed for a low building surrounded by a group of buildings in contrast to the isolated conditions. It was observed the surrounding features affect the changes in the former flow field. Compared to large-scale objects, effect smaller objects had been very rarely focussed. For instance, one such feature is a boundary wall which acts as a ground-mounted barrier. Many of the low-building occupants use this feature as a land subdivision and a windbreaker. According to the previous work, one attempt has been made to distinguish the effect of surrounding boundary walls on the pressure coefficients over flat-roofed buildings (John et al., 2009). However, it was not sufficient to predict the spatial variation and distinguish the effect on flow attributes. None of the design standards compensate the effect on pressure coefficients (external) characteristics in the presence of boundary walls. They provide the design attributes based on basic isolated configurations.

## 1.4 Scope and Objectives

A boundary wall can act as a shielding object when it is constructed around low buildings. The wind interaction due to the shielding effect is essential to provide insights into the absence of specifications. The objective of this experimental study is to investigate the characteristics of the external pressure of low-buildings in the presence of boundary walls. The scope of this study is limited to the gable-roofed low-buildings. A wind tunnel experiment is conducted to simulate the flow field using scaled-down models. This study provides detailed insights on the existing external pressure values on international wind design standards. Moreover, computational fluid dynamics (CFD) models will be developed based on the wind tunnel results to perform parametric studies. We shall divide the main objective into specific objectives as follows.

- To examine effects due to the boundary walls on the design specification provided by international wind loading standards
- To investigate the effect of boundary walls on the spatial resolution of the mean external pressure of a low-rise gable-roofed building. Hence the changes in external wind pressure on the critical zones will be assessed.
- To investigate the effect on the peak pressure coefficients in the presence of boundary walls. Extreme value analysis will be a continuation of the former objective on predetermined vulnerable zones.
- To provide recommendations on the external pressure of gable-roofed low-rise buildings with boundary walls.

## 1.5 Methodology

- An extensive literature survey was carried out to identify the wind pressure attributes related to low-rise structures. Detailed explanations on simulating boundary layer conditions with surrounding interference were discussed.
- A wind tunnel experiment was conducted on a scaled-down low-rise gable-roofed building. The experiments were done under two phases; building without boundary walls and building with three distinct boundary wall patterns.
- Wind tunnel results were analyzed concerning the values provided in international wind standards. The existing external pressure coefficients available in (ASCE/SEI 7, 2016; AS/NZS 1170.2 (2011); EN 1991-1-4, 2005; NBC2015, 2015) have been reviewed concerning the observations made during the wind tunnel experiment.
- Afterward, the spatial resolution of the mean external pressure coefficient was examined. We employed critical zones for the analysis. Subsequently, the effect due to boundary walls was addressed.
- The traditional methods to estimate extreme values were deeply reviewed. Thereby, the analysis of peak pressure coefficients was performed concerning boundary wall patterns.
- CFD (Computational Fluid Dynamics) models were employed to simulate the flow characteristics in the wind tunnel. After the calibration process, the parametric studies were performed to verify the modifications obtained from the wind tunnel experiment.

## 1.6 Outcome of the study

It was emphasized the necessity of recent revisions of current wind loading guidelines related to low-rise structures. There was only one related study that had been conducted on this area of research (John et al., 2009). However, it did not provide any insight into the spatial distribution of pressure coefficients. Therefore, this study assists to provide a base for such wind loading guidelines in the presence of boundary walls. Even though a proper modification should be provided through series of wind tunnel studies, it does not rule out this study to provide detailed insights on pressure coefficients of low-rise buildings.

## 1.7 Arrangement of the Thesis

**Chapter 1** and **Chapter 2** include the genral introduction, motivation of the study and the related work. The main research gaps were emphasized and has been elaborated in the present study. The remaining body of the thesis is divided into four major parts.

**Chapter 3** presents the wind tunnel experimental work carried out. The wind tunnel configuration, the scaling process, and flow simulation are discussed within the chapter.

**Chapter 4** includes an analysis of the results. The comparison primarily consists of several subheadings. Foremost, it presents the analogy of pressure coefficients related to the codes of practice perspective. Afterward, it provides a detailed comparison of the mean pressure coefficient. The methods of estimating peak values and their comparison in the case of boundary walls are presented in the latter part.

**Chapter 5** presents the CFD modelling of the experimental study. The chapter primarily focuses on the calibration process and subsequently, assist the judgments obtained on wind tunnel experiment

**Chapter 6** delivers the conclusion of the research study and possible further extensions.

# 2. LITERATURE REVIEW

## 2.1 Wind Engineering

The logical treatment method of the interaction between the people and their work and the boundary layer wind is known as wind engineering (Cermak, 1975). It is a revolutionary process of acquiring the pressure, loads on the component on the envelope considering the airflow as a fluid. It's essential to have a sound understanding of the properties of fluids and the mechanics of structures to deal with the complex nature of wind events. Civil engineering infrastructures, as well as mechanical engineering, are associated with the effect of wind interaction.

The wind is a random act that cannot be followed easily. The flow field is spatially heterogeneous and depends on the attributes we mentioned before in the introductory chapter. Generally, the airflow near the surface is very turbulent (Gusty) when the effect of surface roughness is dominant. Once the wind comes across ground-mounted objects, separation of flow can occur. In essence, it increases the unsteadiness of the flow field. Thus, highly fluctuating wind flow regimes are often observed closer to structures. Therefore, the surrounding environment plays a significant role in accomplishing precise experimental results.

The primary methods of obtaining wind pressure can be introduced as full-scale, wind tunnel, and CFD modelling. Though, the results from a wind tunnel and the CFD model itself should be verified using reliable data. Design guidelines were based on both wind tunnel and full-scale experiments done several decades back. In particular, many wind tunnel experiments were carried out in an isolated environment. There, it could not explain the interference of the surrounding geometries and features. Hence, the values on the design codes might not be the exact representation of its parent condition. Heretofore, tests are being performed based on the neighboring interference on the effective pressure distribution of the envelope that is elaborated in the latter part of this chapter.

## 2.2 Atmospheric boundary layer

Near the surface of the earth, the frictional effects dominate the forces on the moving air. This region can be extended up to a considerable level of height. This region where the friction dominates is called the atmospheric boundary layer (Simiu & Yeo, 2019). *Coriolis component* of the wind becomes low in this region. Friction forces generated from the boundary layer are perpendicular to the Coriolis component. These two forces should be resolved with force generated due to the pressure gradient. No longer is the direction of wind parallel with isobars. At lower altitudes, these friction effects become significant with the reduced wind speed at the surface. The height of ABL usually is defined as the gradient height $Z_g$. Logarithmic law shall be used to describe the profile of wind speed in strong wind conditions inside ABL. Other models such as power low and *Deaves and Harris model* are also used in practice. Australian/New Zealand codes on wind standards have defined the velocity profiles based on *Deaves and Harris* model. Inside the boundary layer, the velocity of the approaching wind starts from zero at the surface, representing the viscous flow with no-slip behavior. Over the height above the ground, the velocity is released from the effect of roughness. Over the full height of the boundary layer, the wind speed increases exponentially. Afterward, it will reach its initial mean value at a height where the influence of roughness is no longer present, called the gradient height ($Z_G$). Above the gradient height, the velocity of approaching wind is assumed to be uniform (See Figure 2.1).

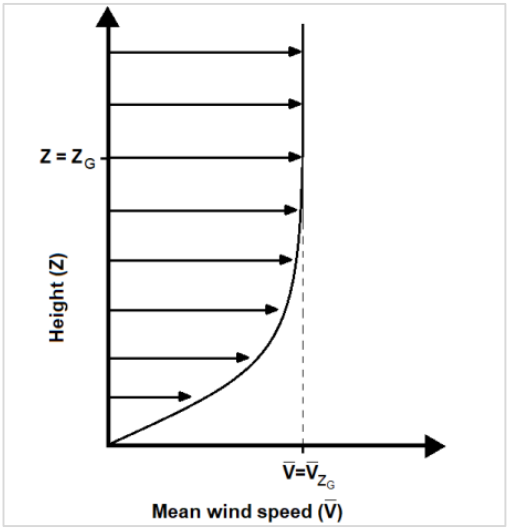


Figure 2.1: Boundary layer velocity profile

## 2.3 Velocity and turbulence

### 2.3.1 Wind velocity

As shown in Figure 2.21, the wind speed profile can be visualized over pre-defined terrain depending on the roughness length. These roughness values are available over different terrain profiles, as updated by Wieringa, (1992). Two different laws explicitly describe the variation of wind speed, called logarithmic law and power law. The power law is sometimes used by engineers even though it is an empirical formula. Eq.(2.1) expresses the equation for power law. Table 2.1 provides a summary of the power-law exponents over various terrains (Stathopoulos & Baniotopoulos, 2007).

$$\frac{V}{V_G} = \left(\frac{Z}{Z_G}\right)^{\alpha} \tag{2.1}$$

The term 'V' denotes the velocity and the subscript 'G' is referred to as gradient height. Alpha values change with the type of terrain. It is noted that, for a rougher terrain exposure, the values of both gradient height and alpha are higher. Eq.(2.2) describes the logarithmic law which has been using by meteorologists and engineers to estimate the wind speed profile. Log law is explicitly valid in the lower part of the boundary layer up to 30% of the gradient height. The equation considers the roughness length ($Z_o$) to be uniform over the terrain. When the experimental results of velocity and height are linearly arranged, the corresponding value of roughness length can be obtained.

$$\frac{U}{U^*} = \frac{1}{k}\ln\left(\frac{Z}{Z_o}\right) \tag{2.2}$$

Terms 'U' and 'Z' represent the velocity and the height above the ground, respectively. The von-Karman constant (k) is approximated to 0.4 and '$U^{*}$' denotes the friction velocity. The roughness length depends on the terrain exposure, having a positive correlation.

Table 2.1: Characteristics of different terrains

| Terrain Category | Corresponding profile | Gradient height (km) | Roughness length (mm) | Mean speed exponent α |
|---|---|---|---|---|
| I | Desert, ice, tundra, sea | 0.25 | 1 | 0.11 |
| II | Open country (low scrub / scattered trees) | 0.3 | 30 | 0.15 |
| III | Suburban terrain, small towns, well wooded areas | 0.4 | 300 | 0.25 |
| IV | Tall buildings, city centers, Developed industrial zones | 0.5 | 3000 | 0.35 |

### 2.3.2 Turbulence intensity

Turbulence is known as the 'gustiness' of the wind flow. It can be related to the fluctuations of wind speed. The usual method is to remove the mean (slowly varying) component and then quantify the resulting deviations. The ratio of the standard deviation to its mean value is defined as the *turbulence intensity* in all three orthogonal directions.

$I_{uu} = \sigma_u / \bar{U}$ ……. Longitudinal direction

$I_{vv} = \sigma_v / \bar{U}$ ……. Lateral direction

$I_{ww} = \sigma_w / \bar{U}$ …….Vertical direction

As measured, turbulence intensity is referred to as the surface roughness related to roughness length ($Z_o$). It has been stated that the vertical and the lateral components are generally low in value compared to the corresponding longitudinal intensity. For well-developed boundary layer winds, simple formulations have been established between standard deviation and friction velocity. Turbulence intensity is likewise a function of roughness length over the terrain. However, turbulence intensity is higher near to the earth and decays over height.

Gustiness does not repeat itself generally. Hence, the variation of the wind speed in ABL is very random. The vortices and eddies in the moving airflow are never identical. For this reason, statistics should be incorporated to describe the gusty nature of the wind flow. Apart from the intensity, turbulence can be explained using the size of the eddies, called the integral length scale. It represents the average size of the large vortices in the flow in all three orthogonal directions. The size of the gusts is insignificant in vertical and transverse directions compared to the longitudinal gusts. Eq.(2.3) describes the longitudinal component of the integral length scale ($L^x$).

$$L^X = \frac{\int_0^\infty R_U(\tau)\, d\tau}{U} \tag{2.3}$$

In the above equation, $R_U$ $(\tau)$ is the auto-covariance function of the fluctuating component of the velocity and U is the mean wind speed. According to Celik, (1999), the theoretical prediction of turbulence is the challenge in fluid dynamics and computational fluid dynamics (chaotic nature of the flow). Due to the above complication, no equations can be derived to predict or quantify turbulence as a function of time or space. The existing models are only considered as a theoretical approximation to the process of turbulence. The absence of such an explicit model leads to initiate turbulence and wind load predictions using CFD techniques.

### 2.3.3 Turbulence spectrum

Wind speed fluctuations consist of different ranges of frequencies. The spectrum of wind represents such frequencies. The following Eq.(2.4) is the turbulence model of Von-Karman to explain the spectrum in wind tunnels. Initial signals correspond to the time domain, can be transformed into the frequency domain using Fourier transformation.

$$\frac{nS(n)}{\sigma^2} = \frac{\frac{4nL_U^x}{U}}{\left[1+70.8\left(\frac{4nL_U^x}{U}\right)\right]^{\frac{5}{6}}} \tag{2.4}$$

The term ‘n’ is referred to as frequency and S(n) represents the spectral density function. Hoven, (1957) introduced the full spectrum of wind, shown in Figure 2.2. Two peaks called ‘macro-meteorological’ and ‘micro-meteorological’ were highlighted on the power spectrum that lasts four days and one minute, respectively. The macro peak is referred to as energy concentration due to the global circulation and the large-scale climate system movements. The micro peak is formed by turbulence due to topography and terrain roughness. The micro-meteorological peak is considered when evaluating dynamic wind forces in structural designs. Low-frequency range wind fluctuations are considered in designs as the fluctuation of the mean wind.

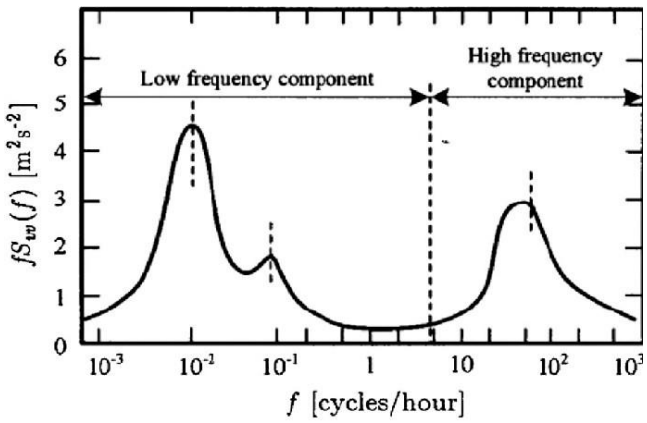


Figure 2.2: Frequency spectrum of wind; Source: Hoven, (1957)

Between the two peaks, a clear gap is distinguished that contains low energy. It is defined as the spectral gap. Accordingly, mean speeds and gusts are characterized. It is significant to notice that within the spectral gap, stable average values can be obtained.

## 2.4 Boundary layer wind tunnel

In the first stage of wind tunnel experiments related to buildings, aeronautical wind tunnels had been utilized. Thus, it was failed to differentiate the actual wind effects near the earth's surface. Jenson, (1958) emphasized the Boundary Layer Wind Tunnels (BLWT) should be used to correctly model the conditions inside the earth's boundary layer. As well the model law was introduced to scale the boundary layer with regards

to the velocity profile. A BLWT usually consists of longer test sections to facilitate the boundary layer to be grown in the tunnel. Davenport & Isyumov, (1967) suggests that the intensity of turbulence, spectra of turbulence and Reynolds stresses, and probability distributions should be included in the simulation criteria. The actual velocity distribution and turbulence characteristics should be matched with the wind tunnel. Testing in the wind tunnels should be acquired with reduced-scale models. The factor used to scale down is called the geometric length scale. Further, the velocity scale and time scale are also associated with the modeling process. The main aim is to reproduce reliable information on the wind effect of structures.

## 2.5 Wind loads on low-buildings

All over the world, a higher percentage of existing structures are low-rise buildings. Those are immersed in the earth's boundary layer and subjected to high turbulence. It indicates the calculation of wind loads must be directed comprehensively. Moreover, the wide varieties of geometric configurations influence complex pressure distributions over the structure. Stathopoulos, (1979) has confirmed, determining the wind loads on a low-rise building is more complicated than in the tall structures due to former reasons.

Wind loading on the components and cladding is higher than such on the major structural system. Because the building-induced turbulence is intense can be observed as localized concentrations. The wind loads correspond to the main structural frame is surface averaged pressure that lacks spatial and temporal fluctuations. Similar conclusions had been made in the study done by Kopp & Morrison, (2018).

### 2.5.1 Flow characteristics around a bluff body

The viscosity of air makes a significant impact on the formation of boundary layers despite its numerical value. "Air has a mass", indicates the inertial characteristics according to Newton's laws and the applicability with Navier-Stokes equations. The

non-dimensional *Reynolds number* is defined as the ratio of inertia forces to viscous forces. Either inertia forces or viscous effects predominate depending on the Reynolds number. If the kinetic energy of the particles is incapable of overcoming the increasing pressure gradient, flow separation occurs, producing adverse pressure gradients. Downstream turbulence behind a bluff body is generally known as the *wake region*, consist of discrete vortices fed by shear layers. These shear layers include the region with considerable velocity gradient and viscous shear effects. It is possible to observe the shear layer when a fluid is passing over a solid boundary. The particles which carry high-momentum will be injected into the separated regions due to the turbulent oscillations, providing a *Reattached flow*. These mechanisms are displayed in Figure 2.3. In contrast to bluff bodies, streamlined bodies usually have narrow separation zones.

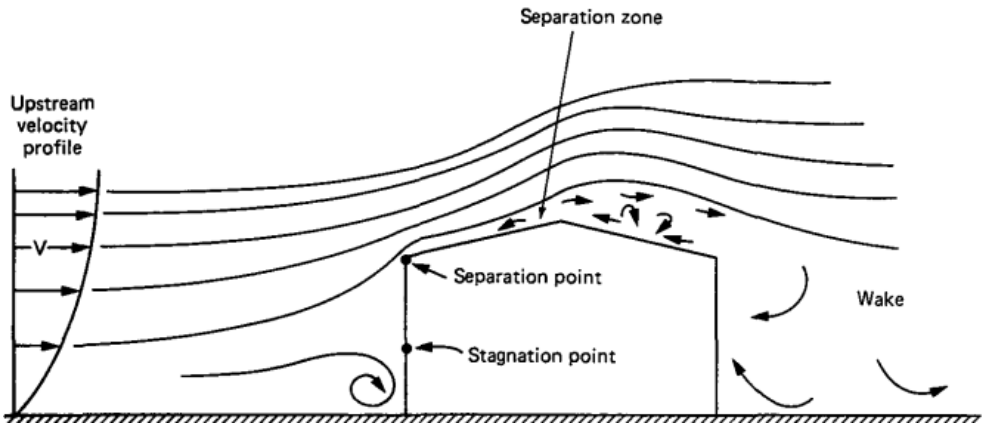


Figure 2.3: Bluff body flow characteristics Source: (Liu, 1991)

Eq.(2.5) depicts Bernoulli's principle of estimating total pressure at a particular point for an inviscid, steady, and irrotational flow. It should be noted, the elevation head has been neglected on either side. Besides, the wake region is not compatible with Bernoulli's equations. Because the sum of static and dynamic heads is less than those of the free stream flow due to the conversion of energy to form turbulence. P, ρ, and V corresponds to pressure, the density of air, and the stream velocity at reference height. Denoting two points in the stream ($P_1$, $U_1$) and the point outside the influence of the body ($P_o$, $U_o$). Bernoulli's equation shouldn't be used in the separated flow section or wake region.

Most of the wind loading standards state these pressure estimations as a non-dimensional quantity, called the coefficient of pressure. Using the following steps, the equation for the pressure coefficients can be derived as in Eq.(2.6).

$$P_o + \frac{1}{2}\rho V_o^2 = P_1 + \frac{1}{2}\rho V_1^2 \tag{2.5}$$

$$P_1 - P_o = \frac{1}{2}\rho V_o^2 - \frac{1}{2}\rho V_1^2$$

$$C_P = \frac{P_1 - P_o}{\frac{1}{2}\rho V_o^2} = 1 - \frac{U_1^2}{U_o^2} \tag{2.6}$$

The mean pressure coefficients and peak pressure coefficients are used to explain the statistical components of the pressure fluctuation. These quantities can be expressed in a similar manner as follows in Eq.(2.7-2.9). The denominator is called the mean dynamic pressure at the reference height.

$$\bar{C}_P = \frac{\Delta P_{mean}}{\frac{1}{2}\rho V_o^2} \tag{2.7}$$

$$\widehat{C_P} \text{ or } \widetilde{C_P} = \frac{\Delta P_{Peak}}{\frac{1}{2}\rho V_o^2} \tag{2.8}$$

$$C_{\sigma P} = \frac{\Delta P_{rms}}{\frac{1}{2}\rho V_o^2} \tag{2.9}$$

The surface interaction of wind and earth is generally consequential. Forces exerted on the ground surfaces due to wind acting across roughness elements where the frictional drag is generated. Estimating these individual components is not easy, and leads us to determine the drag over a particular area. This is generally known as the *surface shear stress*, the force transmitted over the unit area of the ground. The term called *friction velocity* is originated from this shear stress component as follows in Eq. (2.10).

$$U^* = \sqrt{\frac{\Gamma_o}{\rho}} \tag{2.10}$$

$\Gamma_o$ = surface shear stress

$\rho$ = density of air

Even though vertical mass transportation is absent, there is downward transportation of horizontal momentum. It can be observed by the exchanging of two eddies of the same size. This momentum exchange was named after the *Reynolds stress* which will vanish upon the height from the ground surface.

### 2.5.2 The pattern of wind loading on the envelope

Generally, the wind that flows over a building produces relatively large negative pressures on its roof. The studies were done by Parackal, (2018) had identified that failures are more likely to initiate on the roof. Thus, it will redistribute the forces once the localized failures occurred, causing progressive failures.

The reason for negative pressures is the flow separation and steep velocity gradients usually occur near sharped edges and discontinuities. Especially the perimeter zones of the roof and wall, and discontinuity at ridgeline could be identified as the suction-prone regions. Visually, the roof can be divided into three zones such as corner zone, perimeter zones, and interior zone and the pressure exerts on the interior zones are low. In essence, the pressure variation is influenced by the dimensions of the buildings. A recent study done by Kopp & Morrison, (2018) found the zones of pressure on the roofs entirely depend on the height of the building for the mild pitched roofs.

Pressure on the walls is also affected by flow separation at vertical edges up to a certain extent. However, it is not severe compared to the corner roof zones. Pressure values on the walls are also important, especially in the cladding design. Generally, negative pressure entirely dominates the walls facing leeward direction.

## 2.6 Wind pressure attributes on low-buildings

Stathopoulos, (1979) examined the wind pressure on low-rise buildings employing nine different geometry configurations. This experiment provided sufficient wind loading data for codification purposes. The author emphasized, the importance of the height of the building as a critical factor when determining wind loads associated with low structures. Stathopoulos & Surry, (1983) have extended their experiments to investigate the effect of scaling on the wind tunnel measurements of low-buildings. Thereby, a factor of two in the model scale deviated the results by 10% from the former measured values. Deep review studies related to wind effect on low-buildings have been provided by Holmes, (1983); Krishna, (1995); Stathopoulos, (1984); Tieleman, (2003); Uematsu & Isyumov, (1999).

Stathopoulos, (1984) highlighted the importance of wind loading on low-rise buildings since those are associated with relatively large investments. Jenson, (1967) provided valuable aspects to the wind tunnel tests related to low buildings. Benchmarks of stability had been developed by Bounkin & Tcheremoukhin, (1928). Historically, the first full-scale testing was carried out by Bailey, (1933) using a railway car shed. Bailey & Vincent, (1943) undertook a novel series of tunnel experiments that could highlight a good agreement with full-scale test results. Aeronautical type wind tunnels and water flumes, could not sufficiently simulate the turbulent flow and the vertical velocity profile. Later, this issue was addressed by Jenson, (1958) who suggested the similarity between roughness lengths of modeling. The following attributes were emphasized as the factors that govern the effective pressure distribution of low-buildings.

- Effect of geometrical parameters
- Effect of wind direction
- Effect of terrain roughness
- Effect of the tributary area: area loads
- Effect of architectural features
- Effect of large nearby structures
- Effect of internal pressures

Ginger et al., (1999) explained the reason for neglecting the resonant component is that the wind frequency is considerably lower than the natural resonance frequency of a low-rise structure. A house with a gable roof scaled at 1/50 had been tested in the wind tunnel where they had majorly focused on the pressure distribution on the roof. Comparable results were obtained during the experiment with respect to AS/NZS 1170.2 design guidelines. It was found the trusses which subjected to higher loads during a wind event. Generally, due to the suction, these houses should have a vertical load-sharing member. Therefore having a truss fulfills that requirement According to the observations, large suctions are more likely to occur on the gable end for oblique wind approaches and the winds parallel to the ridge.

Tieleman et al., (1981) has conducted a study on two low-rise structures in a wind tunnel using geometric scales of 1:500 and 1:50. The objective was to compare these model scale results with the observations made with a full-scale experiment on building at Aylesbury, UK. From the comparisons, they had made the following statements, the pre-requisites to obtain good relation between $\overline{C_P}$ , $\widehat{C_P}$ , $\widetilde{C_P}$ , and $C_{\sigma P}$. Only a few of those general statements are mentioned below. Mainly, the Reynolds number had affected the discrepancies between the full-scale and wind tunnel.

- Local pressure coefficients should be used for the comparison
- Stream turbulence should be properly modeled up to two building-heights
- Ridges and terrain conditions upstream should be properly modeled with adequate accuracy with nearby surface elevations.

Kanda & Maruta, (1993) examined the mean and peak pressure variation of long low-rise buildings. For ‘d/b’ ratios less than two, it was assumed as the rigid framed roof (‘b’ is the length of longer span, ‘h’ is the height of eaves). For a longer span, this hypothesis is not valid any longer. The results revealed that the wind loads on the end parts of the building are significant from the remaining parts of the structure. Using a visualization test, at θ = 30°, they had identified several types of vortices as shown in Figure 2.4. The scattered pattern over the zones illustrates the reattachments and generated vortices. They have concluded these vortices have been the reason for the large negative pressure coefficients of $\overline{C_P}$ or $\widetilde{C_P}$ on the leeward side. In addition, the

author confirmed that the $\overline{C_P}$ more likely to have uniform values when the reference dynamic pressure is taken along the mid-roof level.

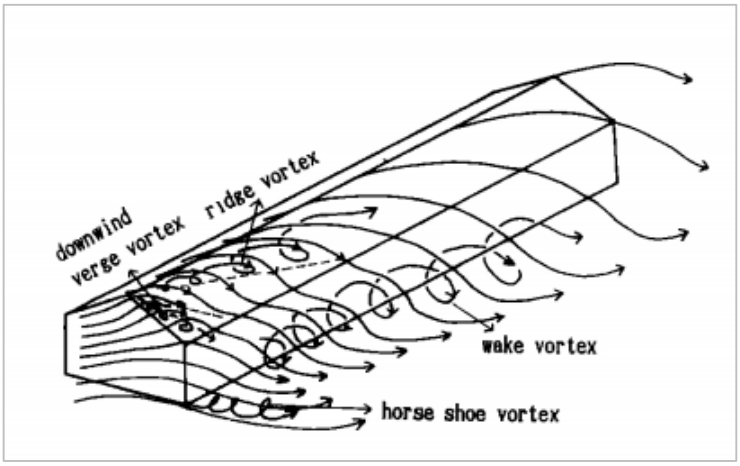


Figure 2.4: Visualization of different vortex formations

Richardson & Surry, (1991) conducted a series of wind tunnel tests using 1:100 models. According to their results, the external pressure coefficient on sidewalls is the closest to full-scale results. The results obtained for the roof exhibited significant deviations from the full-scale due to flow separation. Furthermore, these deviations were identified as roof pitch dependent. Finally, it was concluded that there are occasions where the wind tunnel does not accurately model the flow separation on the windward roof.

Both internal and external pressure is important when estimating the net effect on the envelope. Internal pressure attributes are usually affected by the size, geometry, and location of the openings, volume, shape, flexibility of the building structure, and the characteristics related to external pressure (Habte et al., 2017). Net pressure on the surface is also crucial to determine the force acting on any surface. Negative external pressure can combine with high positive internal pressure to create an adverse pressure difference in severe wind events. This net pressure component is highly affected by the correlation between external and internal pressure. It was found that the internal pressure may contribute to a higher proportion of this net component. Besides, they conducted large-scale testing using a wall of wind (WOW) facility to measure both internal and external pressure with multiple dominant openings. The term, ‘dominant opening’ refers to an opening whose size is two times greater than the total background

leakage area (Holmes & Ginger, 2012). Time histories of the frame forces were evaluated using a database-assisted design (DAD) method. Subsequently, they found, the effect of internal pressure is dependent on the location of a frame, reference to the openings. The intensity is highly dependent on the correlation between the forces exerted due to internal and external pressure. Internal pressure influenced the net response near an opening up to 65% and 45% for single and multiple openings. According to ASCE 7-10, internal pressures have produced significantly conservative results in structures with single and multiple openings.

Studies revealed for a constant roof pitch, elevated houses have had the worst conditions. According to Meecham et al., (1991) hip roofs provided better aerodynamic performance compared to gable roofs. The corresponding peak pressure has reduced by 50% in the hipped roofs. Hoxey, (1991) and Roberston, (1991) concluded that the curved roofs perform much better since suction on the lower 3rd is dropped significantly. The curved surface of the eaves prevented the flow from being separated. However, the negative pressure then appeared near the ridge zone. Overall, the windward roof edge, roof corners, and hip ridge closer to the corner have been identified as the worst loaded zones. They had addressed the effect of a gable roof, hip roof, and flat roof models with adjustable roof pitches through a wind tunnel study. Pressure distribution on the front wall was similar in all three models. The asymmetry of pressure distribution was also observed on several occasions. It was mainly due to vortex shedding and intense mixing closer to the low velocity and high turbulent (near-wake) region. These suction on back walls had eased with increased pitch. Interestingly, the negative pressure on the flat roof was more pronounced compared to the remaining configurations. It was influenced by the separation of flow at the sharp corners. However, the suction reduced considerably after providing a gable roof.

Even if the flow reattaches and reduced the intense negative pressure, the separation next occurred at the ridgeline. If the roof is steep, it bulges into the boundary created by the windward wall. Streamlines are pushed up further, resulting in positive pressure on the windward slope. Gable roofs reduced the maximum suction by a significant proportion compared to a flat roof. The performance was further enhanced by providing a hipped-roof (Prasad et al., 2009).

Parapets were studied to investigate the effect on the net pressure distribution on the roof (Pindado & Meseguer, 2003). Besides, its porosity was also considered as a variable in this study. The effect of porosity was significant. Low porosities lead to a wake region behind the parapets, decreasing the vortex intensity due to the eddy-turbulence. In their conclusion, it was stated that for low relative heights (< 5% of the building height), medium porosity parapets are far more effective than the solid ones to decrease the peak of negative pressure. The net effect reduces when the height of the parapet is increased.

Chang & Meroney, (2003) stated, if the interval between two structures is less than the height of a building, the shielding effect may be dominant and cause to reduce pressures up to 80%. They have considered gable, arched, and dome-shaped roof models to illustrate the pressure distribution. These models have been kept in a tandem arrangement, varying the distance between the model structures. When the gable buildings are closely spaced at a distance equal to the building height, suction could be observed on sidewalls. It verifies a complete vortex formation. However, the effect was eased and positive pressures appeared when the distance between buildings is increased. If we consider the arch buildings and domed-roof structures, the variable spacing between the tandem arrangements has shown that the suction will ease quickly with increased distance. The Dome roof has accounted for the smoothest profile around the structure of all (Chen, 2012).

Bitsuamlak et al., (2013) studied a method to mitigate the negative pressures of roof and wall corners using simple architectural elements. This study has used pergolas, an extension of gable ends, ridgeline extensions, and sideway extension of walls as the key elements. The pergolas (trellis) mechanism works by disrupting the formation of the vortex and shedding at the corners. It was a similar mechanism to fins and corner balconies to reduce the wind on tall structures. Peak suction reduced by 25% while a slight increment was observed on low-suction zones. Ridgeline extension works by moving the vortex away from the corner region. As before, an increment in the suction on the leeward portion was observed. However, this contributed to a 60% reduction in the former peak of the suction. Gable end extensions showed a 65% reduction in the peak negative pressure, having a similar mechanism to the ridgeline extension. Wall extensions have contributed to a 35% reduction in peak suction. It was very significant

to reduce the damage to wall claddings. These components can be easily retrofitted with minimum cost, improving the aerodynamic resilience of the building envelope.

### 2.6.1 Surrounding interference

Subsequently, the experimental works extended further from isolated conditions to actual surrounding conditions to investigate the reliability of results. Wind predictions were conducted on a low-rise structure surrounded by a large group of buildings. Interestingly, it affected the atmospheric boundary layer since each of these building elements can be individually introduced as a roughness element. The flow pattern is the main factor in deciding the wind force attributes and pressure distributions according to Kim et al., (2012).

In the same period, many studies were conducted to simulate complex environments. It was later reflected in the AS/NZS 1170.2 2011 code in terms of shielding factor. Among those, Stathopoulos and his research team did extensive investigations on this area using a wind tunnel and full-scale tests. They investigated, the peak wind loads are more likely to get affected due to these short-distance roughness attributes in contrast to terrain conditions. According to Chang & Meroney, (2003), the impacts of urban street canyons are significant when they are formed narrowly. Such effects tend to be much important in urban zones than in the open country. There are reported cases where shielding effects had contributed to a 100% increment of peak pressure coefficients. One of the deficiencies of these studies was, considering small groups arranged in limited distances. Because the shielding effect is directly proportional to the number of nearby structures.

Afterward, the intense pressure values occur in contrast to isolated conditions. It can be theoretically related if there is a drop in wind pressure ($P_i$ - $P_{static}$). They found the decrement of velocity is significant than the pressure that gives rise to pressure coefficients due to the squared term. Mean wind speed has decreased that might cause turbulence intensity to be increased. In addition, it follows that the variation of the mean wind speed is more sensitive to turbulence intensity. However, this effect will

tend to be insignificant when the $L_{fetch}/B$ close to 15. ($L_{fetch}$ = upstream distance; B = length of a cubical model)

Evaluating the pressure characteristics related to low-rise structures in urban and suburban regions needs a careful review of the complex nature of ABL closer to the earth's surface (Hussain & Lee, 1980). The authors examined the pressure variation caused by the shape and the influence of an array of nearby structures. It was noticed, these structures claim more proportion of the construction budget and susceptible to severe wind damage. Cubic models have been used in an experiment that was scaled into a 1:350 ratio. With the effect of different densities, the drag coefficient reduced and the reduction becomes sudden for higher densities. There are three types of flow regimes that were introduced. The first one is called *isolated roughness flow* where roughness elements are considerably apart from each other. Therefore the object is isolated and the wake region is developed with a fully separated bubble. In the next regime, objects were a bit closer where the separation bubble cannot fully occur. This regime is called a *wake interference flow* regime. The final one is *skimming flow* where the elements are very close to each other. However, stable vortices formed in these rooms between objects. For all arrays and densities, the maximum negative pressure was found to be in the leading edge of the roof. This maximum was strongly dependent on the roughness element spacing. The authors confirmed these nearby interference effects are not present in an isolated environment.

Ho et al., (1991) had investigated the effect of surrounding on wind loads of flat-roof low structures. Initially, there were only a few studies (Hussain & Lee, 1980; Vickery, 1976; Walker & Roy, 1985) that had been conducted on the interference of surrounding structures on wind loads. The discrepancy between the mean wind speed profile and turbulence level should be considered when comparing wind tunnel data from a different source. Among the observations, high positive and negative pressures decreased in complex environments. Reduction in mean loads and increment in dynamic loads was noted caused by increased turbulence. A common conclusion was that the results were substantially different from isolated to complex environment.

Compared to large-scale obstructions, small-scale objects had been less concerned that governs the flow field. For instance, John, (2009); John et al., (2009) have examined boundary walls and their influence on the wind field. The results were compared with full-scale data of the Texas Tech University (TTU) building. Fabrication of model building and boundary walls was done on a geometric scale of 1:25. Testing was performed in two phases: one without boundary walls and the other with boundary walls. Subsequently, the distance to the boundary walls was varied in the experiment as a function of the eave height (H). Most of the results have been in good agreement with the full-scale results of the TTU building. Interestingly, the maximum reduction of pressure coefficient was found on the roof taps when the wall is positioned at 3H away from the building. For short walls, the same happens when the spacing becomes 1.5H. However, this study lacks the spatial resolution of wind pressure to magnify the localized concentrations.

The current study identified this research gap due to the lack of insights on the flow field in the presence of boundary walls. The author needs to highlight, these interference effects are not considered even in international wind loading standards. Low-rise buildings with boundary walls are a common observation in sub-urban zones. Despite its porosity, John et al., (2009) emphasized the pressure coefficients tend to reduce due to the shielding effect using a flat-roofed building model. Therefore, this study aimed to investigate the spatial resolution of the external pressure field over the envelope for a low-rise gable-roofed building.

## 2.7 CFD modelling

### 2.7.1 Governing equations

CFD simulations provide numerical approximations based on basic theories of fluid mechanics. In particular, CFD modelling is preferred to avoid experimental constraints that came across during full-scale or wind tunnel modelling. The choice of CFD modelling for the current study was to assist the observations made during the wind tunnel experiment. The fundamental formulations of CFD modelling can be expressed as follows in Eq. (2.11) to (2.13). Terms p, t, Re, u represent pressure, time, Reynolds number, and velocity, respectively.

Mass conservation

$$\frac{\partial u_i}{\partial x_i} = 0 \tag{2.11}$$

Navier-stokes equation

$$\frac{\partial u_i}{\partial t} + u_i \frac{\partial u_i}{\partial x_j} = \frac{-1}{\rho}\frac{\partial p}{\partial x_i} + \frac{1}{Re}\frac{\partial^2 u_i}{\partial x_i \partial x_j} + f_i \tag{2.12}$$

Burgers Equation

$$\frac{\partial u}{\partial t} + u\frac{\partial u}{\partial x} = \upsilon\frac{\partial^2 u}{\partial x^2} \tag{2.13}$$

Navier stokes equation is difficult to be solved due to the advection term (second term on left). However, this equation can be simplified to one-dimensional as provided in Burgers equation. That has an exact solution and it is generally used to verify the numerical method. Solving the Navier-stokes equation at discrete points is the base of CFD modelling.

### 2.7.2 Turbulence modelling

CFD modeling has been worldwide acknowledged as an advanced technique to study flow features in the lowermost part of the atmosphere. There are numerous applications including wind loads on buildings, pollutant dispersion, pedestrian wind comfort, etc. In this study, as the low-rise structures are fully submerged in turbulent ABL, oncoming flow is always turbulent. Generally, high Reynolds numbers are observed such that finer grid resolutions are necessary to estimate the turbulence dissipation. A proper turbulence model is employed to dissipate the energy of turbulence at higher frequencies in terms of turbulence viscosity. Basic forms of turbulence models are Reynolds Average Navier-Stokes (RANS) and Large Eddy Simulation (LES). RANS solves the numerical equations using the effect of turbulence while LES solves the flow with the sub-grid component. Therefore LES allows us time-dependent simulations even though it is very time-consuming and sensitive to inlet conditions as well (Parente et al., 2019; Rodi, 1997). However, the formula of LES is a simplified version compared to RANS. Further, LES obtain the time series of flow quantities at each grid and evaluate mean, peak, and power spectra as well. Tamura & Kareem, (2013) confirms the numerical solutions of LES are more explainable than the RANS solutions. Moreover, LES generally accounts for larger temporal and spatial turbulent scales that result in improving accuracy (Shah & Ferziger, 1997; Xie & Castro, 2009). LES simulation was much preferred for dynamic behavior despite its computational expense (Ong et al., 2020). However, there were several occasions where it was not properly fit with experimental results. Especially, when the fluctuating component of the wind is considered. Pressure fluctuations are strongly dependent on the incoming turbulence. Moreover, the mesh size and the incoming turbulence can affect the results depending on the location in different ways. Xie & Castro, (2009) presented a detailed analysis on LES and RANS by examining the flow over an array of wall-mounted obstacles. Resutls highlighted that the perfromace of LES can outmatched RANS simulations within the canopy. Detached eddy simulations (DES) represents a solution inbetween LES and RANS which is specifically used for heavily separated flow regimes. The use of RANS modelling is

expected generally for attached boundary layers. Still the computational expense is a constraint associated with DES as well where the alternative is RANS method.

RANS models are observed to be often used in CFD modeling due to the above reason (Gorlé et al., 2009; Longo et al., 2017; Parente et al., 2019). However, their accuracy was not found as the best representative of the parent wind environment. There are several turbulence models, Spalart-Allmaras (S-A), k-ε, and k-ω models which involve generally low-cost computing with turbulence viscosity Li et al., (2015). Strain-based models have provided less pronounced wake regions. Rotations and strain rates decelerate the production of eddy viscosity. S-A models were appeared to be more appropriate for measuring surface pressure. Nevertheless, these models can underestimate or overestimate the turbulence length scale.

In RANS simulations, the effect of roughness is accounted, using sand-grain wall functions (Cebeci, 1987; Parente et al., 2019). For the inlet, the profiles confirmed by (Richards & Hoxey, 1993), (longitudinal velocity (U), turbulent kinetic energy (TKE or k), and dissipation rate of turbulence(ε)) are employed to reproduce the upstream turbulence attributes. However, there might be discrepancies due to the inconsistencies among wall function formulations and fully grown boundary layer inlet profile (Blocken et al., 2007; Franke et al., 2011; Hargreaves & Wright, 2007). The assumption suggested by Richards & Hoxey, (1993), does not actually hold during wind tunnel simulations where the turbulent kinetic energy (TKE) depends on the height above ground.

Later, Blocken et al., (2007) proposed a measure to overcome the former issue, modifying the wall coefficients. However, a completed solution was not obtained even from the modifications. Subsequently, Parente et al., (2010), (2011a), (2011b) suggested a new wall function implementation associated with wall treatments. They specified modification on k-ε model coefficients, proposing a comprehensive approach for the CFD simulations. Using the TKE transport equation, a new profile is obtained for TKE, obtaining a set of inlet conditions for ABL (neutral). This standard k-ε profile was satisfied by those set of profiles.

### 2.7.2.1 Standard (k-ε ) turbulence model

This has the most often employed equations for CFD modelling under homogeneous ABL conditions (Longo et al., 2017; Parente et al., 2019). Those two equations are somewhat complicated, however, can be simplified under the postulations of incompressibility for a stead ABL. $G_k$ is the generation of TKE due to mean gradient of velocity. $\sigma_k$ and $\sigma_\epsilon$ represent turbulent prandtl numbers. $C_{\epsilon 1}$ and $C_{\epsilon 2}$ are taken as constants.

$$\frac{\partial}{\partial z}\left(\frac{\mu_t \partial k}{\sigma_k \partial z}\right) + G_k - \rho\epsilon = 0 \tag{2.14}$$

$$\frac{\partial}{\partial z}\left(\frac{\mu_t \partial \epsilon}{\sigma_\epsilon \partial z}\right) + C_{\epsilon 1} G_k \frac{\epsilon}{k} - C_{\epsilon 2}\rho \frac{\epsilon^2}{k} = 0 \tag{2.15}$$

$$G_k = \mu_t \left(\frac{\partial u}{\partial z}\right)^2 \tag{2.16}$$

$$\mu_t \frac{\partial u}{\partial z} = \Gamma_o \tag{2.17}$$

$\Gamma_o$ is the wall shear denoted in Eq. (2.10). Fully grown inlet profiles can be mathematically expressed as follows (40)

$$\frac{U}{U^*} = \frac{1}{k}\ln\left(\frac{z + z_o}{z_o}\right) \tag{2.18}$$

$$k = \sqrt{A.\ln(Z + Z_o) + B} \tag{2.19}$$

$$C_\mu = \frac{U_*^4}{k^2} \tag{2.20}$$

$$\varepsilon = \frac{{U_*}^3}{\kappa((Z+Z_o)} \tag{2.21}$$

Constants A and B can be determined from the wind tunnel data. The k profile can be expressed as in Eq.(2.19). The term $C_\mu$ should be sufficiently computed to make sure

the required TKE throughout the fluid domain. Gorlé et al., (2009) generalized several equations and expressed $C_\mu$ as given in Eq.(2.20).

### 2.7.3 CFD simulations on low-rise buildings

There is a growing demand in wind engineering applications, to simulate the conditions using CFD techniques. Fouad et al., (2018) have performed a CFD analysis with the aid of full-scale and wind tunnel results. Overall, the CFD model had a good relationship with the results obtained from experiments. However, there existed a discrepancy on the windward sides of the roof. A maximum deviation of about 20% was identified in pitched double roof structures for small roof angles.

On one hand, the CFD technique can provide design data for structures other than those listed in the codes. However, the size of the grid is the most important aspect to be considered when it comes to the accuracy of results. The 2D or 3D grid is created using the following basic elements shown in Table 2.2 and the grid can be categorized into structured or unstructured.

Table 2.2: Common grid elements

| 2 Dimensional | 3 Dimentional |
|---|---|
| 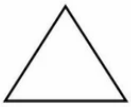 Triangle | 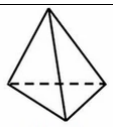 Tetrahedron |
| 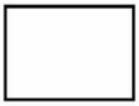 Quadrilateral (2D prism) | 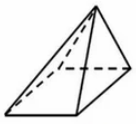 Pyramid |
| | 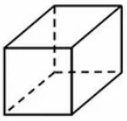 Hexahedron |

| | |
|---|---|
| |  <br>Prism/ wedge (triangular base) |
| | 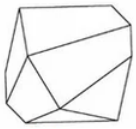 <br>Arbitrary polyhedron |

The general importance of ABL characteristics was investigated by Liu et al., (2018). Many of the researchers have now adopted CFD simulations for their experiments. Normally, these models are classified under either *mesoscale* or *micro-scale* models. Previous investigations did not examine how to simulate urban configurations. Those configurations are more complicated since building density will not be uniform in all directions. The authors made a fair attempt to include surrounding detailing to a considerable level to attain sufficient accuracy in the results.

With increasing surrounding details, the accuracy of the predictions was also increased as stressed in wind tunnel experiments. Sheltering effects were considered to be the reason for the velocity and pressure gradient reduction. Authors confirmed domains of Tominga et al., (2008) and Tong et al., (2016) were the smallest and the largest, respectively. The major difficulty of attaining a fair detailing level was achieved in this study. It was found that after reaching a sufficient level of surrounding detailing, all the predictions were similar to full-scale results. They obtained, within a radius of 3L (L= Length of the building) is the minimum requirement to simulate satisfactory results using CFD models. Likewise, there are a few studies available on the effect of nearby objects on the wind loading on low-rise buildings (Li et al., 2017; Liu et al., 2018).

## 2.8 Summary of the chapter

In this chapter, we highlighted the importance of the accuracy of modeling and the surrounding interference on the results. The required precision of results is dependent on the level of surrounding detailing fed into the analytical model. Full-scale, wind tunnel modeling and CFD simulations were able to deliver satisfactory predictions. Though, the wind loads and the flow characteristics can be significantly altered with surrounding interference.

Current research gaps consist of the importance of small shielding objects that modify the wind flow field rather than the surrounding buildings. Low-buildings are not usually subjected to comprehensive structural analysis and will be mostly constructed, following the design guidelines. It is often observed, contemporary housing compromises boundary walls in the near vicinity. Such ground-mounted objects can influence early flow separation. Therefore, it's essential to investigate the flow modifications due to boundary walls on such structures to improve the design aspects. Therefore, the outcome of this study is significant to emphasize the effect of boundary walls on external pressure fields.

# 3. METHODOLOGY

In this study, a wind tunnel experiment was carried out to investigate the effect of boundary walls on the external pressure. Experiments were performed using a scaled-down building inside the boundary layer wind tunnel at the James Cook University, Townsville, Australia.

Because the study refers to the surface pressure variation, it is required to explore the spatial resolution. The building model has been installed pressure taps by considering critical regions (Refer Annex 2). Besides, the time history data of each pressure tap was recorded to capture the temporal behavior. Further, these time histories are required for the determination of peak pressure coefficients. A set of pressure measurements was carried, changing wind angle in 10° increments. Oncoming velocity and pressure measurements were recorded continuously. Velocity and the turbulence intensity at different heights (z) were captures using the "Cobra probe". Each run was repeated four times to improve the consistency of the results.

## 3.1 The wind tunnel simulation

The experiment was carried out in a 2.5 m wide, 22 long, 2 m tall atmospheric boundary layer wind tunnel (Open circuit). A length scale (Lr) of 1/50 was used to simulate the approaching wind flow. Terrain category was specified between categories II and III as recommended in AS/NSZ 1170.2-2011. The choice of geometric scale is a compromise. The model should be sufficiently large to capture the spatial variation of the external pressure. For the selected scale of 1/50, a model can accommodate sufficient details in the eaves and overhangs (Jayasinghe, 2012). However, it should not be having a notably large dimension that can block the approaching flow. According to the continuity equation, the flow accelerates if the effective cross-section reduces. However, scale fluctuations are not noticeable on the local pressure variation where it is more sensitive to building-induced turbulence. Table 3.1 provides the parameter comparison between the model scale and full scale.

Table 3.1: Comparison of parameters of model scale and full-scale

| Parameter | Full Scale | Models Scale |
|---|---|---|
| Length scale | 1 | $\frac{1}{50}$ |
| Velocity scale | 1 | $\frac{1}{2.5}$ |
| Time scale | 1 | $\frac{1}{20}$ |
| Approached Velocity | 100 Km/h | 11 m/s |
| Sampling Time | 10 Minutes | 30 s |
| Jenson Number | 98 (mid-roof level) | |

The time scale was selected as 1/20 of the full scale. When the sampling is considered, the period of averaging is imperative to minimize sampling errors. World metrological organization has provided 10 minutes averaging period for the standard practice. According to Hoven, (1957), values between 1 hr and 10 minutes correspond to full scale, often used in the wind tunnel experiments as stable values. Velocity scale was obtained from L= VT; as 1/2.5 of the full-scale velocity. Since the resonance effects are negligible in the low structures, a convenient velocity scale can be chosen. However, attention should be paid to the Reynolds number achieved in the wind tunnel. Generally, the bluff body separation is independent of the Reynolds number. A minimum Reynolds number of 15000 is expected to model flow attributes (Meroney & Neff, 1982). Nevertheless, the width covered in the turbulence spectrum depends on the Reynolds number (Re). Re equal to 37000 has been achieved in the wind tunnel at the height of the mid-roof.

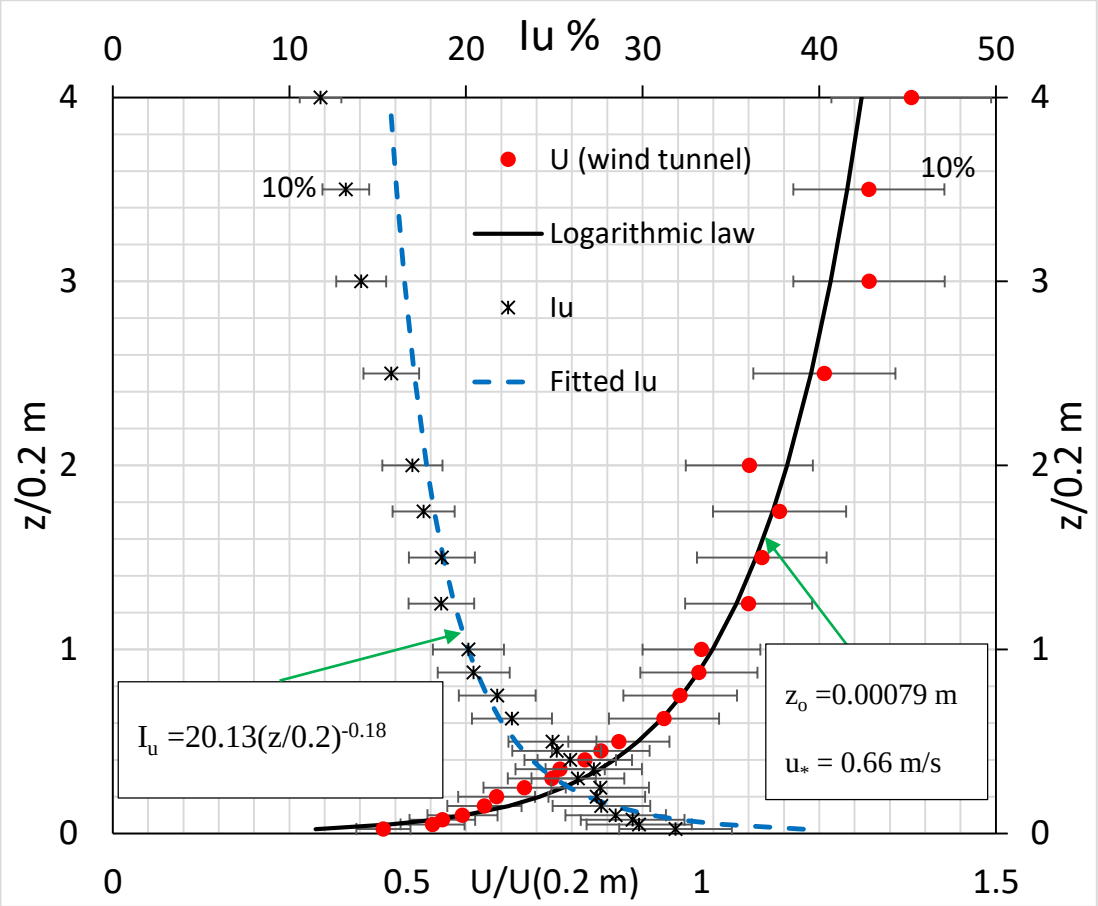


Figure 3.1: Velocity and turbulence profile of approached wind flow

The longitudinal mean speed profile and the turbulence intensity are depicted in Figure 3.1. The wind speed profile appeared to follow the logarithmic wind profile. The roughness length of the upstream fetch was calculated as 0.00079 m on the model scale (Refer Annex 03). Corresponding Jenson number was obtained as 93 at roof-mid height. The simulated turbulence intensity profile fell within the specified profiles for terrain categories II and III in the Australian standard. However, it did not explicitly fit with either of the terrain profile. Therefore, a separate profile was fitted to turbulence intensity values. It depicts a 20.13% reduction in the turbulence intensity at z = 0.2 m in the model scale. The turbulence spectrum displays the integral length scale of 0.35 m at which matches the Von-Karman turbulence spectrum (See Figure 3.2).

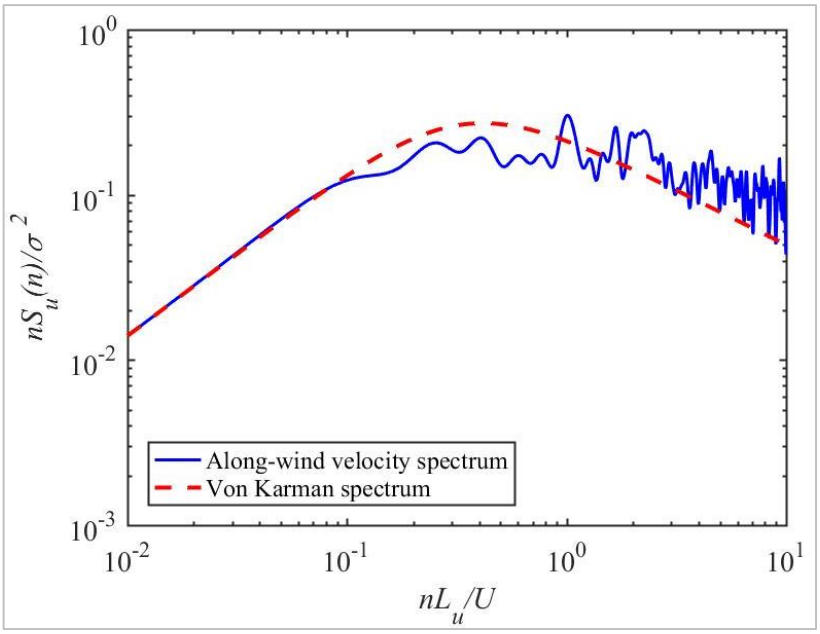


Figure 3.2: Power spectrum of approached wind velocity

### 3.2 The gable house model

The model used for the experiment was made of perspex, installing 248 pressure taps on the external surface as following in Figure 3.3. The building has overhangs extending 0.6 m from either side on the full scale. Therefore, pressure taps were provided on the overhangs as well. Previous studies have shown the pressure distribution with eaves and without eaves significantly differs. A dense tap arrangement near the roof perimeter is required to monitor critical locations, described in Chapter 2. The model geometry and boundary walls are symmetric along the ridgeline and the direction normal to the ridgeline. Boundary wall configurations are exhibited in Figure 3.4 (a-c) and the wind tunnel experimental setup is shown in Figure 3.5. A sample calculation of the $\overline{C_P}$ can be explained as follows which is similar to the calculation of $\widehat{C_P}$ , $\widetilde{C_P}$ and $C_{\sigma P}$. Channel 1 is the reference in all four pressure tap modules. We shall consider $\overline{C_P}$ calculation at channel 2 of 'module A' along zero wind azimuth. The reference dynamic head is considered at the roof-mid height, for the $C_p$ calculation.

Channel 1: 68.3 Pa (Referenced at 500 mm height above the wind tunnel bed)

Channel 2: -13 Pa

$$\bar{C}_{P,500} = \frac{-13}{68.3} = -0.19$$

$$\bar{C}_{P,\text{mid roof}} = \bar{C}_{P,500} \cdot \frac{U_{500}^2}{U_{\text{mid-roof}}^2} = \frac{-0.19 \text{ x } 10.88^2}{7.14^2} = -0.44$$

Gust factor can be estimated as follows:

$$G_U = 1 + 3.4 I_{UU} = 1 + 3.4 \text{x} \frac{26.17}{100} = 1.89$$

A separate script was composed using python programming to handle wind tunnel data more efficiently as provided in Annex 04.

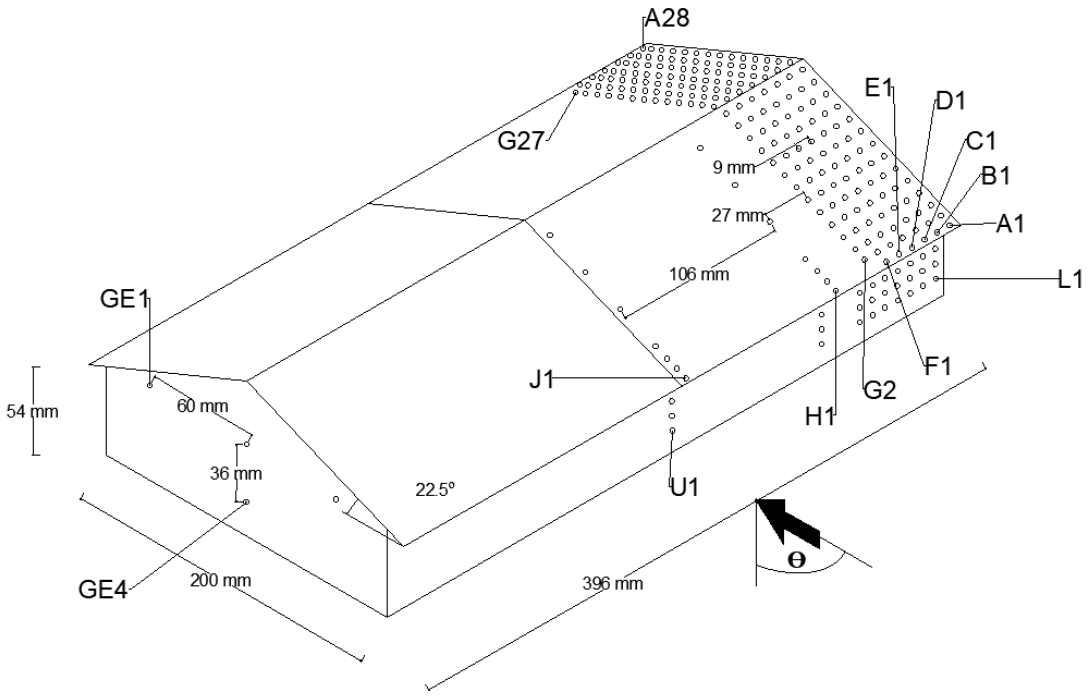


Figure 3.3: Pressure tap arrangement on the model house

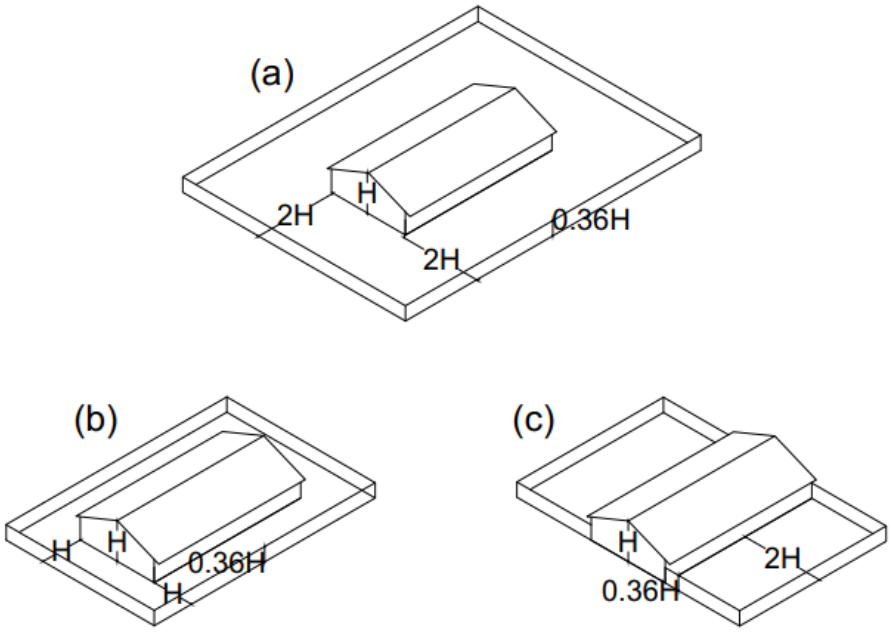


Figure 3.4: Configuration of (a) Boundary wall pattern 01 (BW1); (b) Boundary wall pattern 02 (BW2); (c) Boundary wall pattern 03 (BW3)

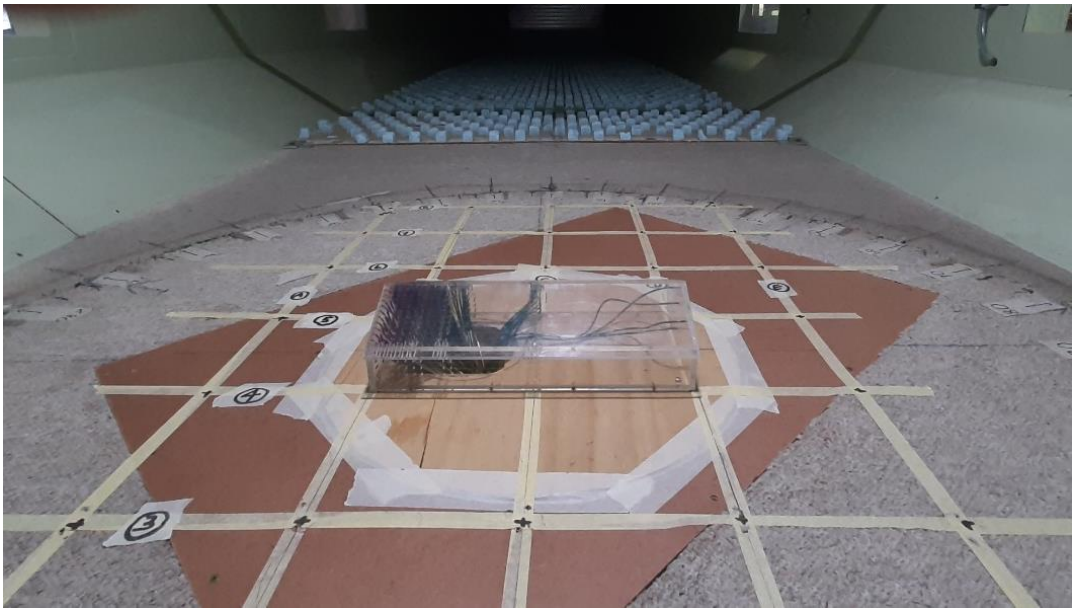

(a)

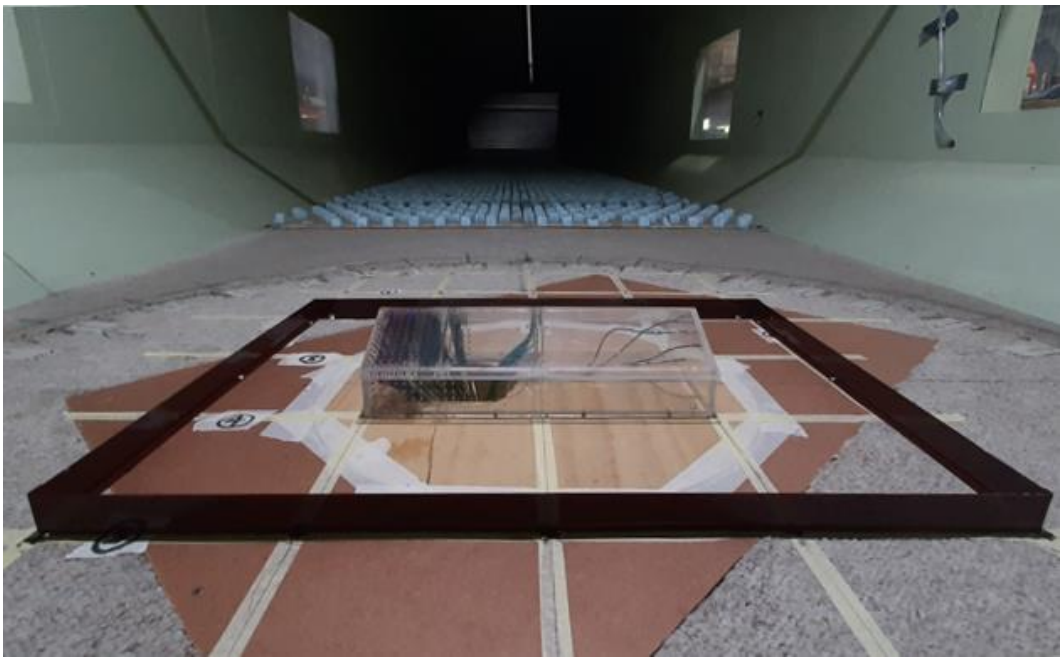

(b)

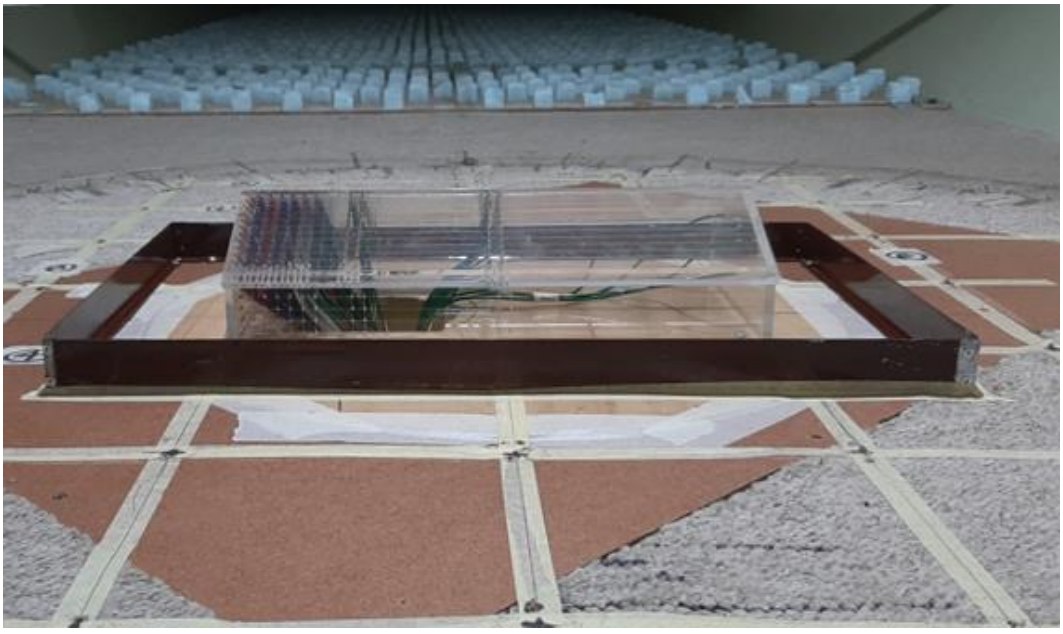

(c)

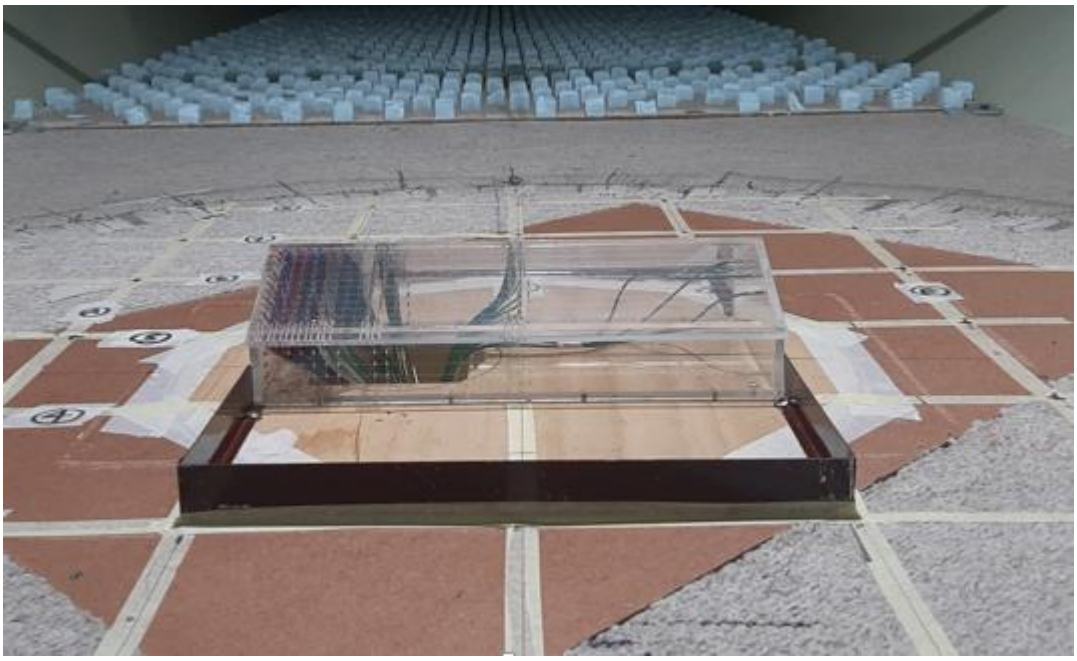

(d)

Figure 3.5: Wind tunnel experimental setup; (a) BM; (b) BW1; (c) BW2; (d) BW3

### 3.3 Verification of wind tunnel data

It is required to verify the wind tunnel data before the analysis, using a reliable database or a similar study. Nowadays, comprehensive databases are available for reference, including a wide variety of geometry configurations. ASHRAE provides a handbook that contains pressure coefficient values. As well, TPU and NIST databases are considered reliable open access platforms. In addition to the low-rise buildings, the TPU database contains the pressure data of high-rise buildings and a group of low-rise buildings. For the current study, we employed the research study done by Parackal, (2018) for verification where the same building model had been used. We obtained a hit rate of 0.8 (See Figure 3.6), between former results and current observations ($R^2$ of 0.98). The hit rate calculation steps are provided in Annex 02.

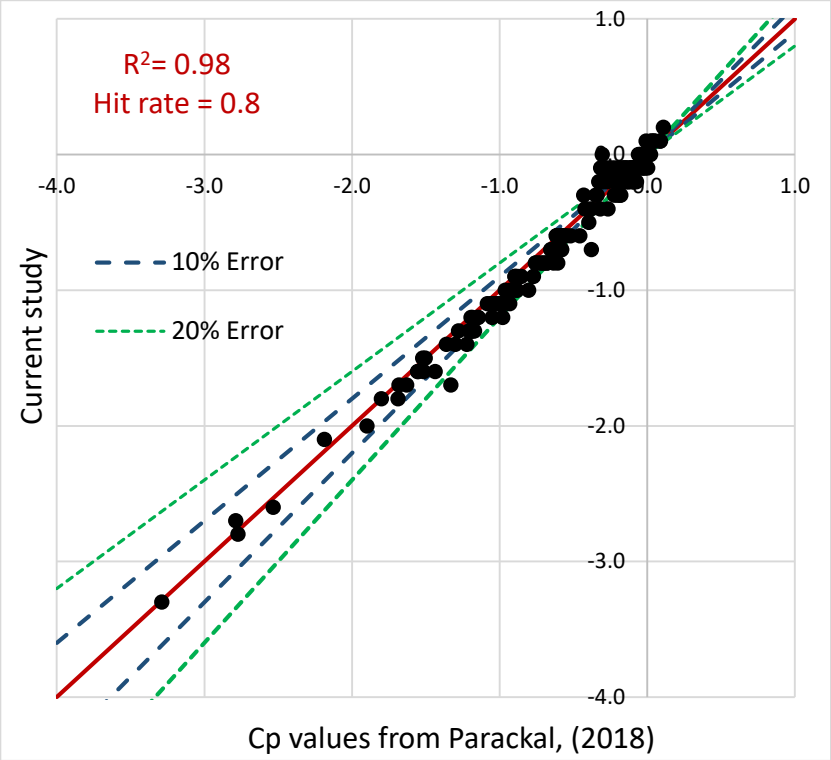


Figure 3.6: Validation of wind tunnel results

### 3.4 Summary of the chapter

This chapter discussed the experimental work carried in order to investigate the pressure distribution. The experimental process was carried out in an open circuit wind tunnel available in the cyclone testing station, James Cook University, Townsville, Australia. The Characteristics of wind profiles such as the velocity and the turbulence intensity were in accordance with the targeted profiles under sub-urban exposure. The roughness length was estimated as 0.00079 m on the model scale. The wind tunnel test was performed for both the isolated model and the model with boundary walls, recording the pressure time histories. Soft computing techniques were employed to analyze the wind tunnel data. The results obtained, follow the observations made by Parackal (2018) with a strong correlation.

# 4. ANALYSIS OF RESULTS

## 4.1 Comparison with codes of provisions

Wind loading standards provide a simplified approach to estimate the design wind pressure on buildings. Therefore, we employed the external mean pressure coefficient ($\bar{C}_p$) for the analysis and to investigate the effect of boundary walls on it. Codes define a zoned arrangement to denote the external pressure coefficient of the envelope. Besides, for the design of the main structural system, each design standard provides pressure coefficients in two directions. The direction of the wind at θ = 0° is called along wind and θ = 90° is called the crosswind. Four international wind loading standards were followed for the analysis as follows. However, none of these design guidelines reflect the effect of boundary walls on the external pressure coefficient (ASCE 07, 2016) (AS/NZS 1170.2,2011) (EN 1991-1-4, 2005) (NBCC, 2015). Further, we assume the quasi-steady-state assumption for the analysis.

- AS/NZS 1170.2 2011 – Australian and New Zealand standard
- EN-1991-1-4 – European standard
- ASCE 07-16 – Australian standard
- NBCC 2015 – Canadian standard

The main objective of code comparison is to investigate the effect of boundary walls on the existing pressure coefficients. The pressure variation is heterogeneous on the envelope and a function of the location. To deal with such random nature, it was extracted from the time histories, the mean, r.m.s, and the peak (minimum/ maximum). All four codes provide $\bar{C}_p$ averaged on pre-defined zoning arrangements. Peak pressure coefficients on cladding and components are provided in NBCC 2015 and ACSE 07-16. The same sign convention will be used to denote pressure coefficients, negative values for suction, and positive values for pressure. The proposed zoning arrangements are illustrated in Figure 4.1.

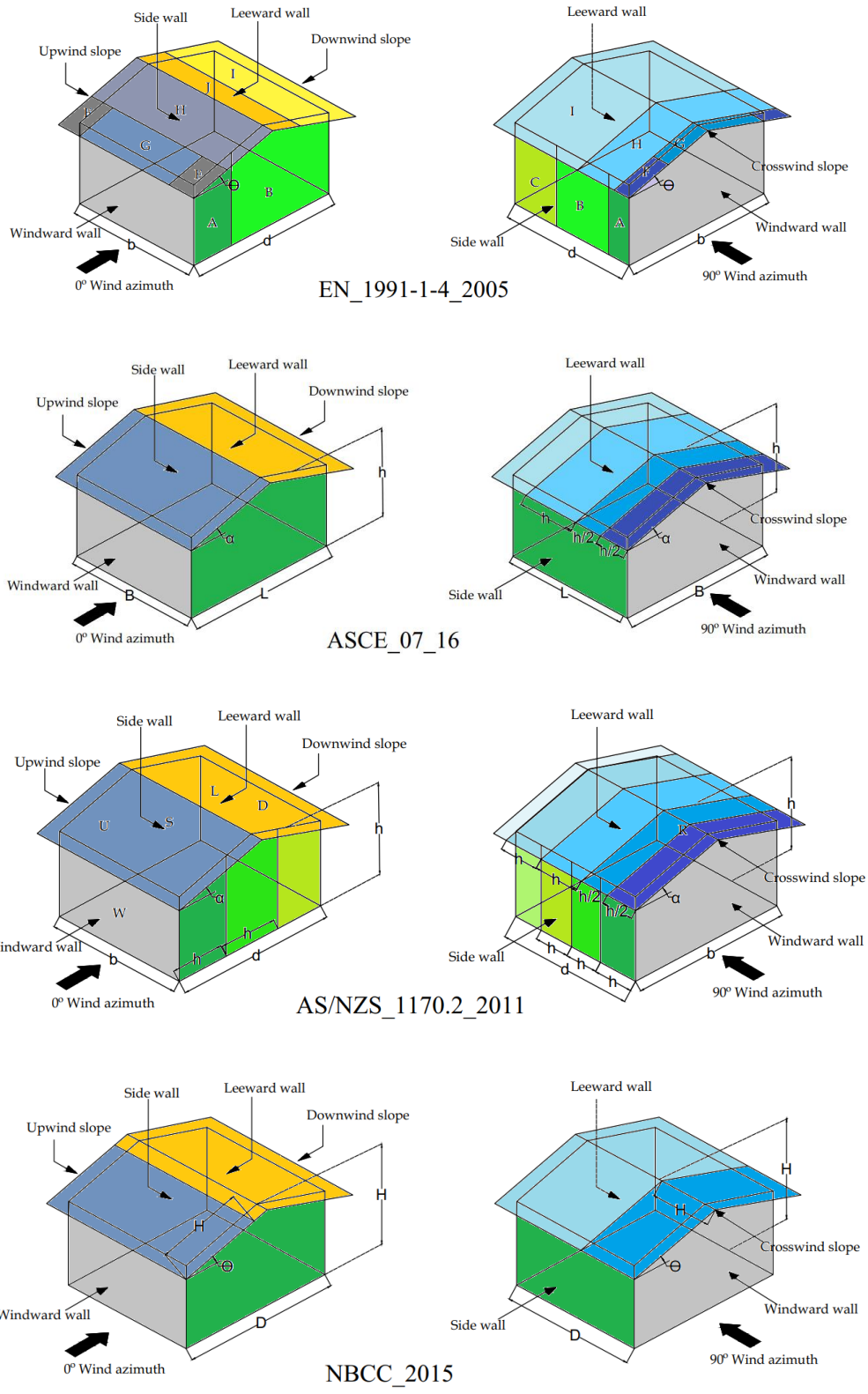


Figure 4.1: Proposed zoning arrangement in wind loading standards

According to the above figure, all the codes except EN-1991-1-4 (2005), defined the roof into only two parts the along wind direction. Australian standard divides the crosswind slope into five segments based on the mid-roof height. European and American recommendations suggest the building roof be divided into four zones starting from the leading edge for crosswinds. However, ASCE 07-16 or NBCC 2015 do not consider segmented zones on the side walls. It is interesting to notice only the European code has dense zoning arrangements for both upwind and downwind slope for the zero wind attack. All four wind loading standards do not demarcate zones on either windward or leeward walls.

Table 4.1: Comparison of $\bar{C}_p$ values at θ = 0°

| Region | Windward wall | Leeward wall | Sidewall | | | Upwind slope | | | Downwind slope | |
|---|---|---|---|---|---|---|---|---|---|---|
| ***Division*** | ***W*** | ***L*** | ***0-1h*** | ***1h-2h*** | ***2h-3h*** | ***U*** | | | ***D*** | |
| **AS/NZS 1170.2 2011** | 0.7 | -0.45 | -0.65 | -0.5 | -0.3 | -0.3 | | | -0.6 | |
| BM | 0.58 | -0.42 | -1 | -0.61 | -0.44 | -0.1 | | | -0.6 | |
| BW1 | 0.21 | -0.27 | -0.64 | -0.42 | -0.35 | 0.18 | | | -0.48 | |
| BW2 | 0.01 | -0.42 | -0.8 | -0.52 | -0.41 | 0.11 | | | -0.54 | |
| BW3 | 0.21 | -0.29 | -0.4 | -0.38 | -0.31 | 0.1 | | | -0.53 | |
| ***Division*** | ***D*** | ***E*** | ***A*** | ***B*** | | ***F*** | ***G*** | ***H*** | ***J*** | ***I*** |
| **EN 1991-1-4 2005** | 0.73 | -0.37 | -1.24 | -0.8 | | -1.32 | -0.65 | -0.25 | -0.75 | -0.4 |
| BM | 0.58 | -0.42 | -1 | -0.56 | | -0.14 | -0.03 | -0.09 | -0.61 | -0.61 |
| BW1 | 0.21 | -0.27 | -0.64 | -0.4 | | 0.4 | 0.51 | 0.11 | -0.52 | -0.46 |
| BW2 | 0.01 | -0.42 | -0.8 | -0.48 | | 0.4 | 0.55 | 0.02 | -0.56 | -0.54 |
| BW3 | 0.21 | -0.29 | -0.4 | -0.36 | | 0.25 | 0.37 | 0.05 | -0.64 | -0.51 |
| ***Division*** | | | | | | | | | | |
| **ASCE 7-16** | 0.69 | -0.43 | -0.61 | | | -0.24 | | | -0.48 | |
| BM | 0.58 | -0.42 | -0.66 | | | -0.1 | | | -0.6 | |
| BW1 | 0.21 | -0.27 | -0.46 | | | 0.18 | | | -0.48 | |
| BW2 | 0.01 | -0.42 | -0.56 | | | 0.11 | | | -0.54 | |
| BW3 | 0.21 | -0.29 | -0.37 | | | 0.1 | | | -0.53 | |
| ***Division*** | | | | | | ***< 1H*** | | | ***>H*** | |
| **NBCC 2015** | 0.67 | -0.37 | -0.7 | | | -1 | | | -0.5 | |
| BM | 0.58 | -0.42 | -0.66 | | | -0.06 | | | -0.55 | |
| BW1 | 0.21 | -0.27 | -0.46 | | | 0.26 | | | -0.41 | |
| BW2 | 0.01 | -0.42 | -0.56 | | | 0.19 | | | -0.48 | |
| BW3 | 0.21 | -0.29 | -0.37 | | | 0.17 | | | -0.47 | |

Tables 4.1 and 4.2 present the summary of the code comparison. Table 4.1 explains the $\bar{C}_p$ for the along wind direction and Table 4.2 includes the $\bar{C}_p$ in orthogonal wind direction (crosswind). Several guidelines recommend two values with different signs

for the roof where the coefficients should be chosen according to the observed in the wind tunnel test.

Table 4.2: Comparison of $\bar{C}_p$ values at θ = 90°

| Region | Windward wall | Leeward wall | Sidewall | | | | Crosswind slope (R) | | | | |
|---|---|---|---|---|---|---|---|---|---|---|---|
| ***Division*** | ***W*** | ***L*** | ***0-1h*** | ***1h-2h*** | ***2h-3h*** | ***>3h*** | ***<0.5h*** | ***0.5h-h*** | ***h-2h*** | ***2h-3h*** | ***>3h*** |
| **AS/NZS 1170.2 2011** | 0.7 | -0.3 | -0.65 | -0.5 | -0.3 | -0.2 | -0.9 | -0.9 | -0.5 | -0.3 | -0.2 |
| BM | 0.86 | -0.18 | -0.52 | -0.29 | -0.05 | -0.06 | -1.11 | -0.68 | -0.33 | -0.1 | -0.12 |
| BW1 | 0.57 | -0.06 | -0.19 | -0.08 | 0.04 | 0.07 | -0.53 | -0.17 | -0.11 | -0.02 | 0 |
| BW2 | 0.55 | -0.17 | -0.29 | -0.2 | 0 | 0.02 | -0.8 | -0.32 | -0.2 | -0.06 | -0.03 |
| BW3 | 0.71 | -0.19 | -0.42 | -0.45 | -0.28 | 0.14 | -1.1 | -0.68 | -0.47 | -0.25 | -0.13 |
| ***Division*** | ***D*** | ***E*** | ***A*** | ***B*** | ***C*** | | ***F*** | ***G*** | ***H*** | ***I*** | |
| **EN 1991-1-4 2005** | 0.7 | -0.3 | -1.31 | -0.8 | -0.5 | | -1.75 | -1.78 | -0.7 | -0.5 | |
| BM | 0.86 | -0.18 | -0.58 | -0.46 | -0.06 | | -1.31 | -1.18 | -0.9 | -0.18 | |
| BW1 | 0.57 | -0.06 | -0.24 | -0.16 | 0.06 | | -0.47 | -1.07 | -0.32 | -0.02 | |
| BW2 | 0.55 | -0.17 | -0.31 | -0.26 | 0.02 | | -0.7 | -1.3 | -0.56 | -0.06 | |
| BW3 | 0.71 | -0.19 | -0.38 | -0.44 | 0.06 | | -1.41 | -1.18 | -0.9 | -0.19 | |
| ***Division*** | | | | | | | ***< 0.5h*** | ***0.5h-h*** | ***h-2h*** | ***>2h*** | |
| **ASCE 7-16** | 0.7 | -0.26 | -0.6 | | | | -0.82 | -0.82 | -0.44 | -0.24 | |
| BM | 0.86 | -0.18 | -0.25 | | | | -1.11 | -0.68 | -0.33 | -0.13 | |
| BW1 | 0.57 | -0.06 | -0.04 | | | | -0.53 | -0.17 | -0.11 | 0.01 | |
| BW2 | 0.55 | -0.17 | -0.11 | | | | -0.8 | -0.32 | -0.2 | -0.03 | |
| BW3 | 0.71 | -0.19 | -0.15 | | | | -1.1 | -0.68 | -0.47 | -0.14 | |
| ***Division*** | | | | | | | ***< 1H*** | | ***> H*** | | |
| **NBCC 2015** | 0.6 | -0.3 | -0.7 | | | | -1 | | -0.5 | | |
| BM | 0.86 | -0.18 | -0.25 | | | | -0.93 | | -0.13 | | |
| BW1 | 0.57 | -0.06 | -0.04 | | | | -0.38 | | -0.01 | | |
| BW2 | 0.55 | -0.17 | -0.11 | | | | -0.6 | | -0.03 | | |
| BW3 | 0.71 | -0.19 | -0.15 | | | | -0.92 | | -0.15 | | |

According to Tables 4.1 and 4.2, the correlation between the pressure coefficients of the code and the base model can be illustrated as in Figures 4.2 to 4.5. The calculated correlation values were 0.94, 0.86, 0.95, and 0.85 following Australian, European, American, and Canadian recommendations. Generally, the Pearson correlation above 0.8 depicts strong linearity. ASCE 07-16 and AS/NZS 1170.2 2011 show a comparatively good agreement with the wind tunnel results. Though, NBCC 2015 and EN 1991-1-4 2005 had deviations greater than 20% of the wind tunnel results.

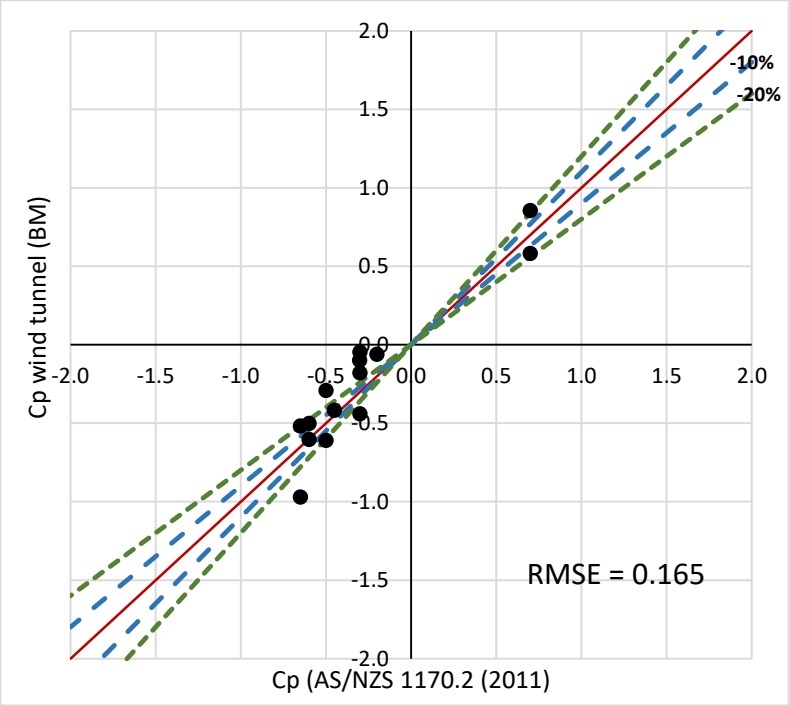


Figure 4.2: Comparison of $\bar{C}_p$ with AS/NZS 1170.2

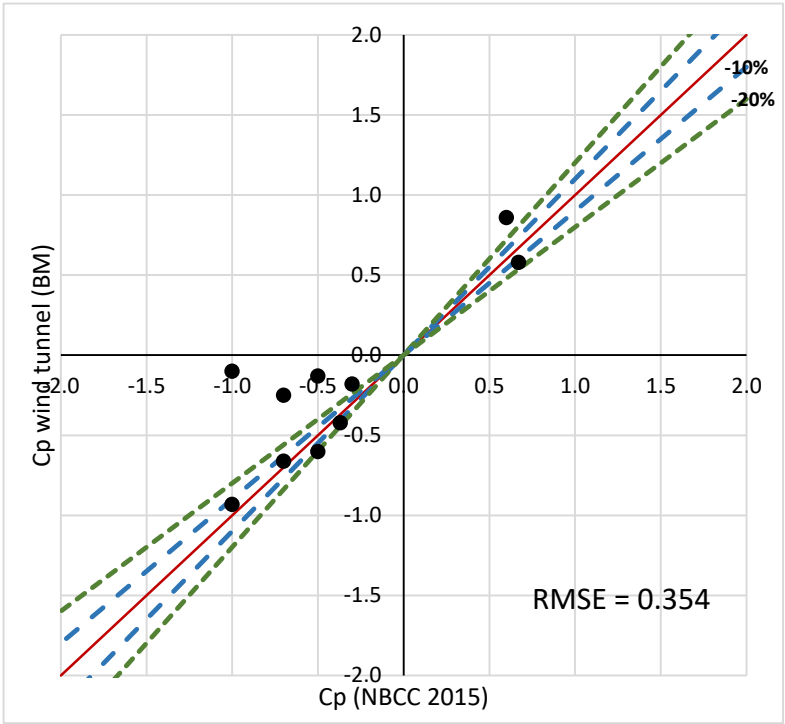


Figure 4.3: Comparison of $\bar{C}_p$ with NBCC 2015

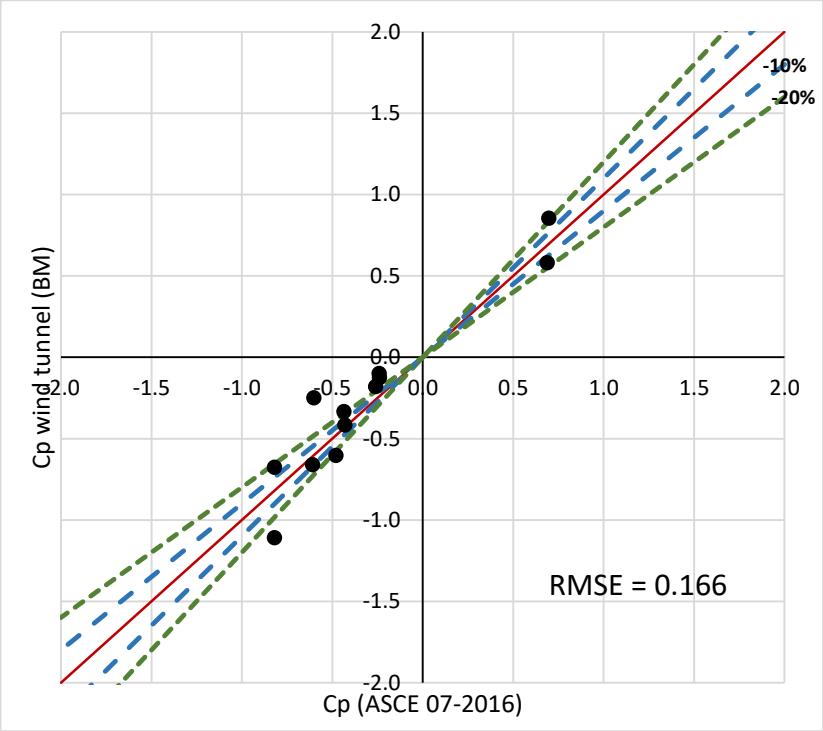


Figure 4.4: Comparison of $\bar{C}_p$ with ASCE 07-16

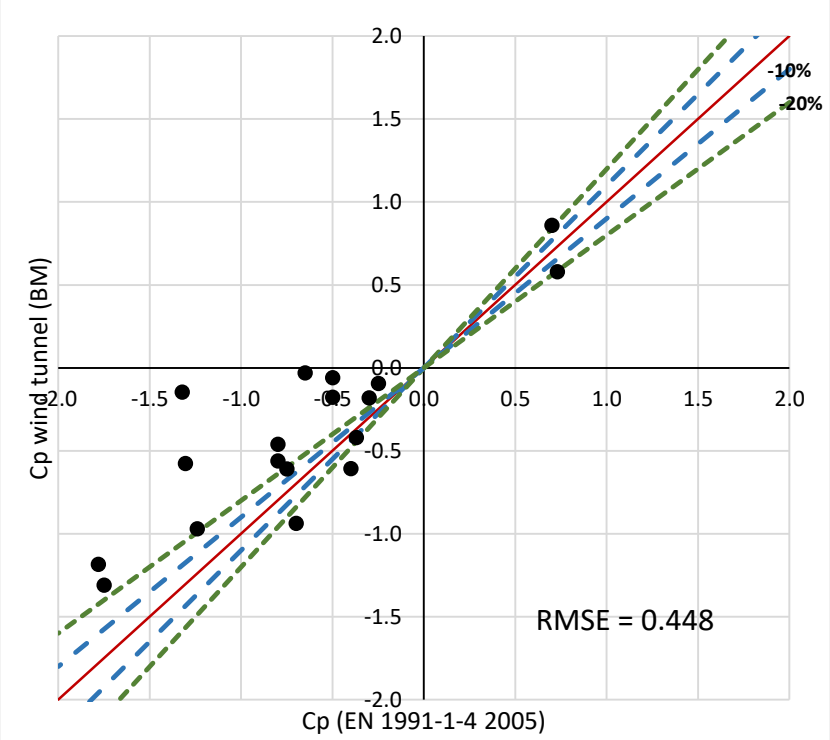


Figure 4.5: Comparison of EN 1991-1-4 2005

### 4.1.1 Effect of boundary walls on the codified recommendations

The $\bar{C}_p$ values obtained from the wind tunnel base model (BM) and the suggested values from the standards are compared here. For the comparison, the area-averaged pressure coefficient was employed. It is the product of the pressure coefficient and its tributary normalized by the total tributary area. Each wind loading standard provides the basis to compare the $\bar{C}_p$ values with the BM. Next, the interrelation between the values is investigated for each wall pattern. The effect of boundary walls is separately discussed on building components.

The change in former values is directly related to the change in boundary wall pattern. Inside a boundary wall pattern, the separation distance from upstream or lateral direction changes. Especially, pattern 03 has a zero lateral separation distance, being similar to the base model. From here onwards, we will denote BW1, BW2, and BW3 for the boundary wall patterns 01, 02, and 03 and the Base Model as BM.

### 4.1.2 Effect on the walls

#### 4.1.2.1 Windward wall (W)

When the walls are considered, the general observation is the positive values below the eave level for direct wind attacks. Stagnation of flow occurs nearly the middle of the wall and it is where the maximum positive pressure values are observed. It was displayed that the $\bar{C}_p$ on the walls will vary from 1 to 0 (windward wall) and the maximum values could be seen near the middle while the values become lesser towards the corners of the wall. (Liu, 1991).

All the selected guidelines have recommended a single value for the entire windward distribution. From wind tunnel results, the $\bar{C}_p$ on the long wall reached 0.58 at $\theta = 0°$. The corresponding values obtained as 0.7 from AS/NZS 1170.2 2011, 0.73 from EN 1991-1-4 2005, 0.69 from ASCE 7-16, and 0.67 from NBCC 2015. For $\theta = 90°$, the

corresponding $\bar{C}_p$ value of BM has reached 0.86. Except for NBCC 2015, all three design standards suggest 0.7 for the windward wall at θ = 90°. Canadian recommendations provide 0.6 as the corresponding $\bar{C}_p$ value. Therefore, we discovered slight disagreements between the BM and the wind loading standards. The $\bar{C}_p$ value on the long walls was lower than the recommendations provided by the standards. However, the codes provide an underestimation for the gable wall.

A considerable reduction of $\bar{C}_p$ was ascertained in the presence of boundary walls. BW1 and BW3 provide the same average value of 0.21 over the longwall at θ = 0°. Former values have decreased 63% in this case. Both patterns have similar upstream separation distances. There it highlights the less impact from the lateral separation of the wall pattern. Besides, the positive pressure on the long wall has almost become zero for BW2.

At θ = 90°, the $\bar{C}_p$ values on the gable wall have decreased from 0.86 to 0.57 for BW1. For BW2, $\bar{C}_p$ becomes 0.55 from 0.86. The zero lateral separation may have caused the value of BW3 to increase in contrast to BW1 and BW2. Since the $\bar{C}_p$ value gives a representative value on each instance, it fails to predict the underlying spatial distribution. Therefore, the distribution of $\bar{C}_p$ on each surface will be helpful to ascertain the change in magnitude as well as the variation. Figure 4.6 depicts the observed variation of pressure coefficient along the windward wall at θ = 0°. Figure 4.7 depicts the observed variation of pressure coefficient along the windward wall at θ = 90°. The same sign convention used in the design standards has been used to denote the $\bar{C}_p$ values. Dotted lines indicate negative pressure (suction) values and solid lines indicate positive values (higher than the ambient pressure).

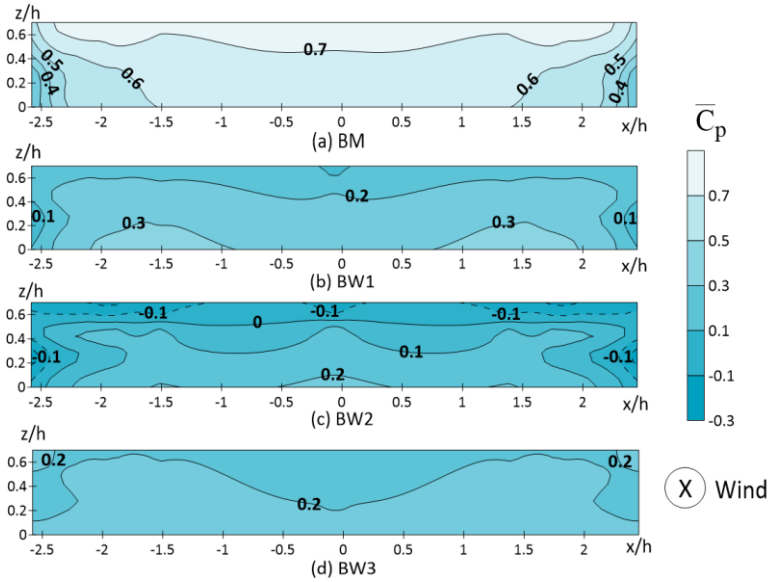


Figure 4.6: $\overline{C}_p$ distribution of the windward wall at θ = 0°

We observed a major portion of the wall is having 0.7. Towards the corner regions, the $\overline{C}_p$ values reduce to 0.3. Also, at the corners, close contours reveal moderately significant pressure gradients. Such pressure gradients got eased in the presence of boundary walls. For BW1 and BW3, a major portion of the wall consists of a value of 0.2. Variation in the distribution is notable in the distribution of BW2. Even the top part of the wall contains negative values. Design standards have failed to predict such considerable variations in the pressure. A value of 0.1 dominates over the windward wall at θ = 0° for BW2. Here, the distributions reveal boundary walls alter not only the magnitude but its spatial resolution.

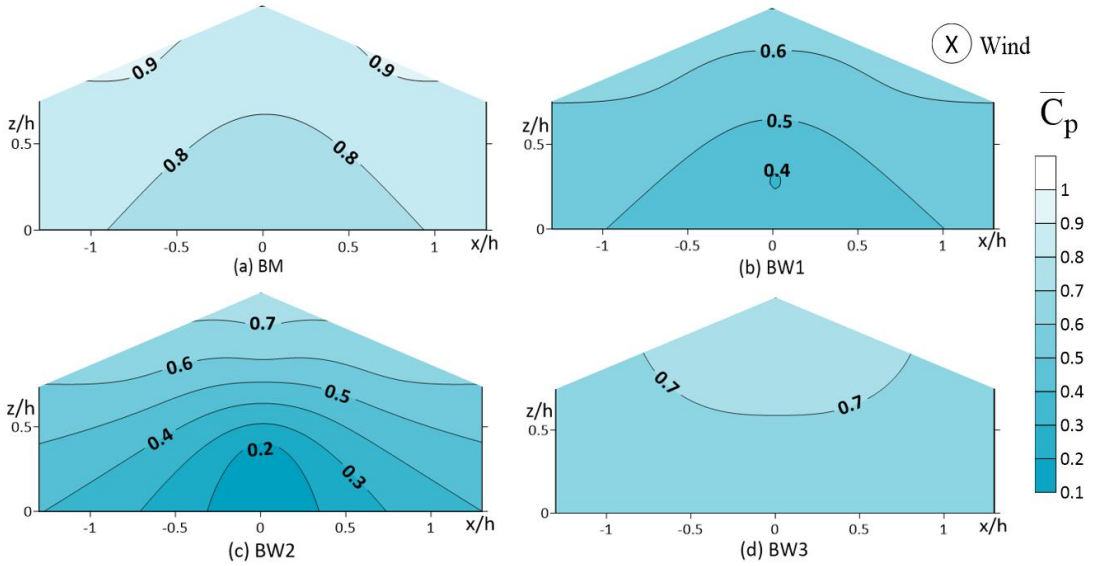


Figure 4.7: $\bar{C}_p$ distribution of the windward wall at θ = 90°

From the above figure, the variation of BM has changed for building with surrounding walls. Interestingly, the effect of lateral separation contributes to higher $\bar{C}_p$ values for BW3. Though, its distribution is markedly different from the distribution obtained for the BM. Repeatedly, BW2 consists of closely spaced contours over the entire windward wall at θ = 90°. The lower part of the wall has reached 0.8 to 0.4 for BW1, 0.2 for BW2, and 0.7 for BW3.

#### 4.1.2.2. Leeward wall (L)

Similarly, codes define the $\bar{C}_p$ values of the leeward wall by using a face-averaged value. The leeward wall faces the recirculating wake formed behind the house. Therefore, negative values of pressure over the entire wall are usual on the leeward surface. Liu, (1991) suggested, $\bar{C}_p$ values could vary from -0.2 to -0.5 on the leeward surface. Further, the values are affected by the depth to breadth and height to breadth ratios.

Codes of practice suggest $\bar{C}_p$ values from -0.37 to -0.43 for the long wall at θ = 0°. For θ = 90°, recommendations are made from -0.26 to -0.3 for the gable wall. Wind tunnel results of BM displayed that the codes have over-evaluated the intensity of negative pressure on the leeward face. It was noticed a 40% reduction in the suction on the gable walls compared to the recommendation on the design guidelines. For θ = 0°, $\bar{C}_p$ values deviated 11% from the suggestions in European and Canadian standards. As well those suggestions were underestimations.

A substantial reduction in the negative pressure could be observed for BW1 and BW3 except for the crosswind direction. The $\bar{C}_p$ value of BM (-0.45) has decreased to -0.27 and -0.29, respectively. However, the $\bar{C}_p$ value shows independence on BW2 where the $\bar{C}_p$ value holds -0.42 similar to BM. At θ = 90°, the $\bar{C}_p$ value of the leeward wall reduced from -0.18 to -0.06 for BW1, -0.17 for BW2, and -0.19 for BW3.

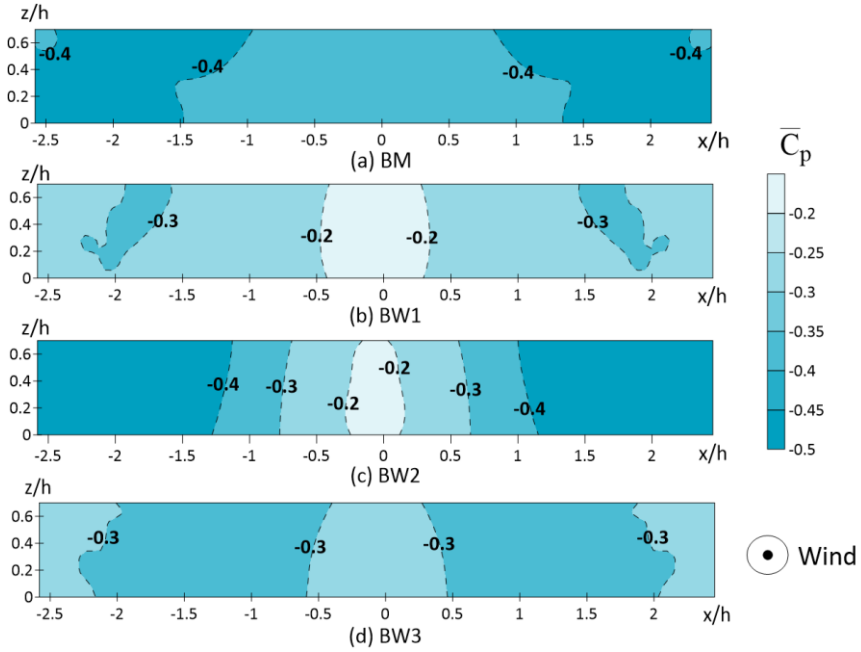


Figure 4.8: $\bar{C}_p$ distribution of the leeward wall at θ = 0°

A uniform value of -0.45 is distributed towards the corners of the leeward wall of BM. In the middle, the $\bar{C}_p$ value becomes -0.4 (See Figure 4.8). With BW1, a larger area of the wall holds -0.25. Minimum and maximum values of $\bar{C}_p$ reached -0.3 and -0.25. Contours spaced nearby for BW2. The entire variation explains a relatively higher pressure gradient that may induce differential loading on wall claddings. Design guidelines have failed in capturing such pressure gradients in the leeward wall. It repeatedly witnesses the statement that the boundary walls can change both magnitude and variation of external wind pressure. With zero lateral separation, the $\bar{C}_p$ value of the BW3 has recorded -0.3 in contrast to BW1.

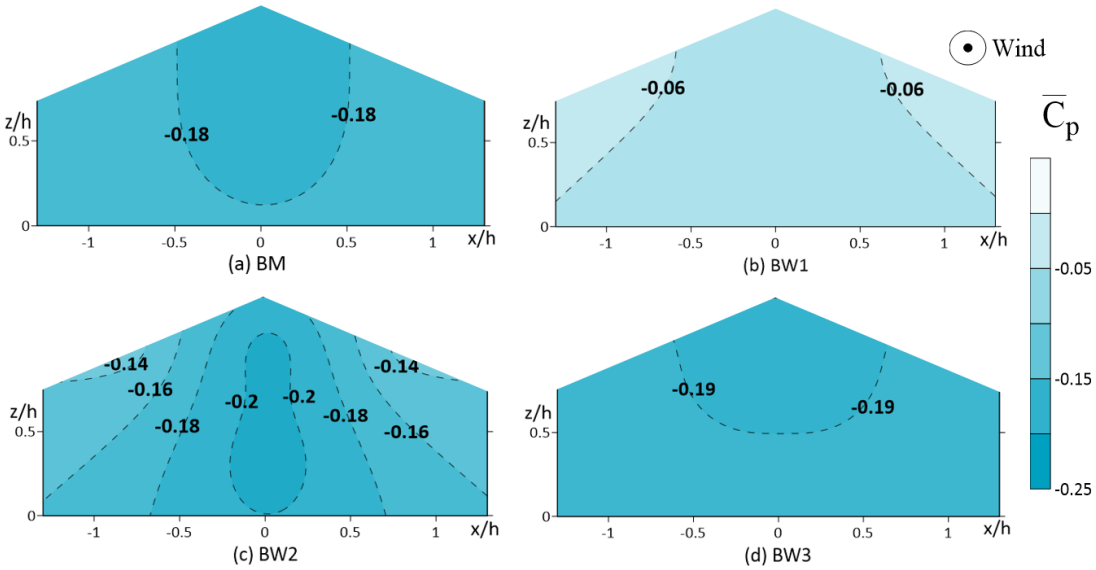


Figure 4.9: $\bar{C}_p$ distribution of the leeward wall at θ =90˚

The variation of $\bar{C}_p$ depicts a similar pressure variation for BM and BW3 at θ = 90° (see Figure 4.9). The reason could be explained as the zero lateral separation distance. A notable difference in the pressure distribution is obtained for BW2. At θ = 0°, markedly different higher pressure gradients were observed on the leeward wall. For BW2, the lateral and upstream separation distances are 1H. Thus, it constricts the recirculating wake zone, creating adverse pressure gradients. Interestingly, the isolated

building exhibited only a uniform $\bar{C}_p$ value throughout the surface. BW1 recorded the lowest values among all experimental cases.

#### 4.1.2.3. Sidewalls (S)

Leeward and windward walls were likewise interpreted using face averaged $\bar{C}_p$. Nevertheless, the $\bar{C}_p$ values on the sidewalls will not be uniformly distributed even for isolated buildings. Wind flow starts separating at leading vertical edges. Thus, it creates a gradual variation from the leading edge to the trailing edge of the sidewall. A continuous reduction in the negative pressure is frequently seen along the side walls. For the BM, $\bar{C}_p$ values exerted on both the longwall and gable wall were negative values.

ASCE 07/16 and NBCC 2015 suggest -0.61 and -0.7 for the side walls at θ = 0°, respectively. Wind tunnel experiment resulted in the pressure coefficient as -0.66 for BM. EN 1991-1-4 2005 suggest two zones on the side walls at θ = 0°. However, the value for zone a (-1.24) is higher than the value observed in the wind tunnel (-1). For zone B, the wind tunnel resulted in -0.56, lower than the recommendation (-0.8). AS/NZS 1170.2 uses segmented widths of mid-roof height (h) along the sidewall. The value for the leading zone is suggested as -0.65. The respective observation made during the wind tunnel was -1. For all three zones, the wind tunnel has repeatedly recorded slightly higher values. Except for the leading zone (<1h), $\bar{C}_p$ values are comparable for the remaining zones.

At θ = 90°, long walls represent the sidewall. The face-averaged $\bar{C}_p$ value has reached -0.25 for the BM. However, ASCE 07-16 and NBCC 2015 suggest overestimations on sidewalls as-0.6 and -0.7, respectively. Besides, EN 1991-1-4 2005 demarcates three zones on the sidewall at θ = 90°. A value of -1.31 was over-conservative than the wind tunnel result (-0.58) for zone A. Even for zones B and C, comparatively high overestimations are seen. Especially, the code suggests a value of -0.5 for zone C, and the actual observation is -0.06. The same effect is present for the recommendation provided by AS/NZS 1170.2. However, Australian and European standards suggest a

rational basis to understand the realistic wind behavior on sidewalls. Near to the leading edge, the Australian standard provides a value of -0.65, which was comparable with (-0.53) in the wind tunnel.

Generally, the zones closer to the leading edge contains higher negative values compared to the remaining zones. Intermittent vortex formation would be a possible reason for such negative values. Considering the value obtained experimentally near the leading edge, a single averaged value appeared as a fair representation.

As the boundary wall are constructed, negative pressure over the sidewalls tends to reduce. Therefore, it seems the flow separation becomes weaker in the presence of boundary walls. At $\theta = 0°$, the face-averaged value of $\bar{C}_p$ becomes -0.46 for BW1 and -0.56 for BW2. The lowest value of -0.37 has been obtained due to BW3. Compared to European specifications, the $\bar{C}_p$ values of zone A becomes -0.64 for BW1 and -0.4 for BW3. However, the lowest reduction in suction is obtained for BW2. The value reduces from -0.56 to -0.4 for BW1 in zone B. Corresponding values for BW2 and BW3 were recorded as -0.48 and -0.36. It implies largely over-conservative values are involved in design standards due to the isolated conditions.

At $\theta = 90°$, the effect of boundary walls was much noticeable. Towards the trailing edge of the wall, positive values of $\bar{C}_p$ are observed. Australian and European standards provide realistic insight about the pressure variation of side walls rather than two remaining wind loading standards. Compared to the BW1 and BW2, BW3 shows relatively pronounced negative pressure values. EN 1991-1-4 seems to overestimate the suction near the leading edges. The $\bar{C}_p$ value of the BM reduces further from -0.58 to -0.24 for BW1, -0.31 for BW2, and -0.38 for BW3. Interestingly, zone C emphasized a fully developed separated bubble on the sidewall. The $\bar{C}_p$ value of the BM (-0.06) has further decreased to 0.06 for BW1 and BW3, and 0.02 for BW2. Therefore the pressure has fully recovered from initial negative values and reattached near to the trailing edge. All four codes failed prediction such possible flow reattachments in the presence of boundary walls.

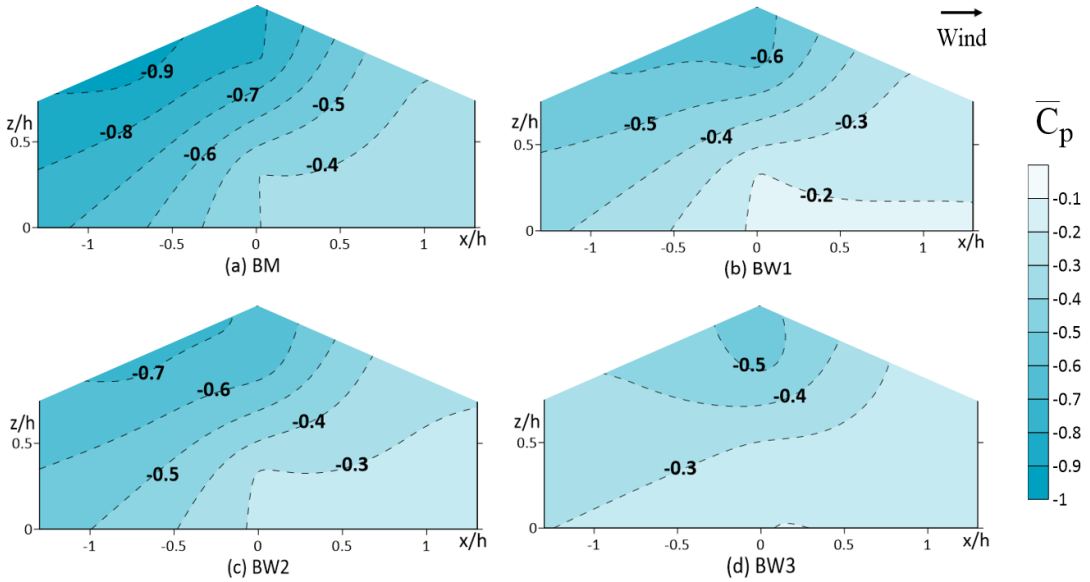


Figure 4.10: $\bar{C}_p$ distribution of the sidewall at θ =0°

The variation of $\bar{C}_p$ on the sidewall of BM appeared to be less affected due to BW1 and BW2 (See Figure 4.10). However, the magnitude changes on each occasion. Underneath the gable edge of the roof, negative pressure values have reached -0.9. It becomes -0.6 for BW1 and -0.7 for BW2. For both BW1 and BW2, the pressure gradients have been slightly reduced on the wall surface. The lower part of the wall consists of -0.4 for the BM and altered as -0.2 for BW1, -0.3 for BW2, and BW3. For BW3, even the distribution changes concerning BM. A value of -0.3 appears along the diagonal direction on the wall. Towards the apex, lesser areas consist of -0.5. Values for BW1 and BW2 stressed that flow separation becomes weak in the presence of surrounding boundary walls.

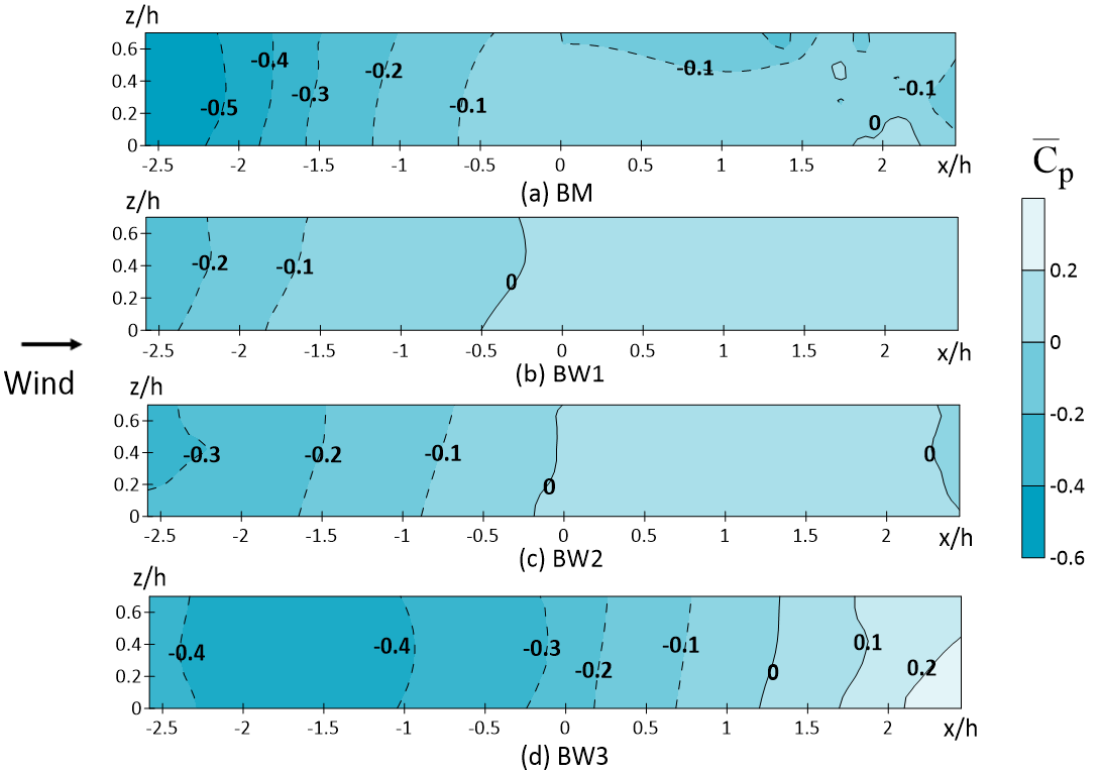


Figure 4.11: $\bar{C}_p$ distribution of the sidewall at θ =90°

Figure 4.11 illustrates that the BM consists of banded contours on the sidewalls near the leading edge. Therefore it holds moderately large pressure gradients. The maximum and the minimum value of $\bar{C}_p$ were recorded as -0.5 and 0. These contours get dispersed for BW1 and BW2. Not only the contour variation but also the magnitude of $\bar{C}_p$ values changes. In particular, the maximum $\bar{C}_p$ value changes from -0.5 to -0.2 for BW1, and -0.3 for BW2. A large stretch of the sidewall consists of 0 for former wall patterns. Repeatedly, it indicates the possibility of flow reattachments due to the boundary walls. On the variation of BW3, the reattachment has grown into positive values as well. Markedly different observations were made near the leading edge within 1H distance for each case.

### 4.1.3 Effect on the roof

Generally, roofs have been emphasized as the vulnerable component experienced moderately higher suction (Habte et al., 2017; Moravej et al., 2017; Parackal et al., 2018; Pindado & Meseguer, 2003; Prasad et al., 2009; Tieleman et al., 2007). Especially the corners and edges were noticed as critical locations where the intensity of vortices is substantial. Liu, (1991) described, the pattern of wind flow over the roof depends comprehensively on geometry, building height, plan dimensions, and flow attributes.

ASCE 07-16 and AS/NZS 1170.2 2011 provide single face-avaraged $\bar{C}_p$ values for both upwind and downwind slopes. EN 1991-1-4 2005 reflects a reasonable judgment based on critical zones, illustrated in Figure 4.1. It is seen that the EN 1991-1-4 2005 particularly isolates the leading edge and corner where steep pressure gradients are frequent. NBCC 2015 divides the roof into two parts, considering the building height. Therefore, either zone may include the ridgeline.

#### 4.1.3.1. Upwind slope (U)

AS/NZS 1170.2 2011 and EN 1991-1-4 2005 specify the $\bar{C}_p$ value of upwind slope to be -0.3 and -0.24, respectively. However, the corresponding $\bar{C}_p$ value for the BM (-0.1) shows the codes are conservative. Besides, a $\bar{C}_p$ value of -0.1 on the upwind half reveals the mild flow separation might have occurred. NBCC anticipates a moderately high negative value over the entire upwind half. The obtained $\bar{C}_p$ value (-0.06) from the wind tunnel exhibits the values are heavily overestimated in the Canadian standard. In essence, within a 1H distance from the eaves level, the $\bar{C}_p$ value is substantially different when the ridgeline is included. It implies another flow separation that occurs near the ridgeline. The flow field over the upwind half is plausibly explained in EN 1991-1-4 2005 recommendations. However, the suggested values are far more conservative than the observed values. For instance, EN 1991-1-4 2005 defines -1.32 for zone F, -0.65 for zone G, and -0.25 for zone H. BM of the wind tunnel has reported

-0.14 for zone F, -0.03 for zone G, and -0.09 for zone H. Thus, design standards seem to expect steep flow separation on the existing upwind configuration.

When the boundary walls are placed, the $\bar{C}_p$ value of the BM is changed to positive. $\bar{C}_p$ value becomes 0.18 for BW1, 0.11 for BW2 and 0.1 for BW3. From comparing BW1 and BW3, a moderate effect from lateral separation is observed at $\theta = 0°$. As per Canadian standard, the $\bar{C}_p$ value becomes 0.26 for BW1, 0.19 for BW2, and 0.17 for BW3. Therefore, the flow reattachment greatly has influenced the $\bar{C}_p$ values within 1H away from the separating edge.

#### 4.1.3.2. Downwind slope (D)

An identical value could be observed on the BM compared to the AS/NZS 1170.2 2011. As well, the $\bar{C}_p$ value provisioned in NBCC 2015 (-0.55) was comparable with the BM. The average suction on the downwind slope (-0.6) is 25% higher than the recommended value in the ASCE 07-16. The zoning arraignment introduced by EN 1991-1-4 2005 proposes two zones on the downwind half. Again, the BM obtained identical values for each zone (-0.61), implying a consistent variation of negative pressure over the downwind slope. Code suggests -0.75 for zone J. However, the euro code specifies a reduction in the value can be made as (-0.4) in the zone I closer to the trailing edge. There, the code leads to overestimate the suction in zone J and underestimate zone I.

From the wind tunnel observations, the $\bar{C}_p$ value obtained was -0.48 for BW1, -0.54 for BW2, and -0.53 for BW3. The $\bar{C}_p$ value due to boundary wall patterns seems less affected compared to BM. Corresponding wind tunnel values were -0.41 for BW1, -0.58 for BW2, and -0.47 for BW3, referring to NBCC 2015.

Wind flow appeared to separate across the ridge-line and haven't been reattached at the downwind region. It could be influenced due to the roof pitch of the selected model. When the roof pitch is increased from mild to steep, Ho et al., (1991) and Holmes, (1986) emphasized that the suction is reduced on the windward half, and flow will

separate at ridge discontinuity. Figure 4.12 depicts the variation of $\bar{C}_p$ over the upwind and downwind halves at θ = 0°.

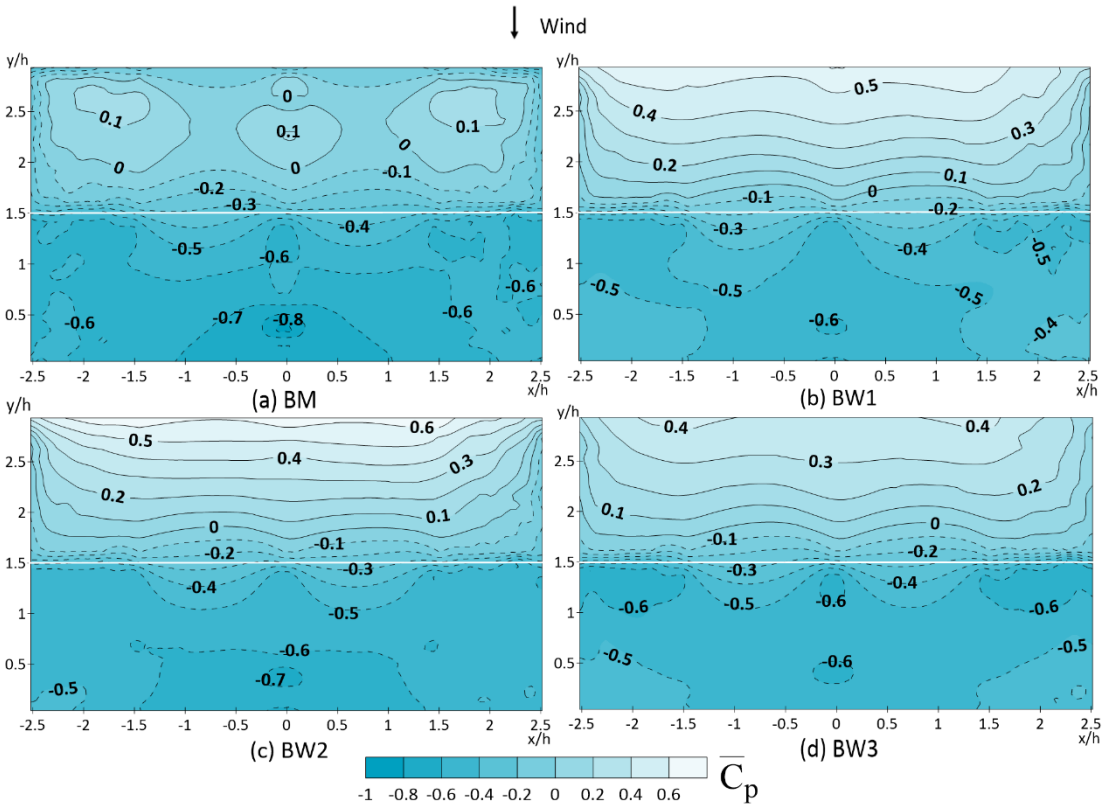


Figure 4.12: $\bar{C}_p$ distribution of the roof at θ =0°

Figure 4-12 illustrates the mean pressure distribution on the building roof at θ = 0°. Especially for BM, less pronounced suction appears near the leading edge at eaves height. Next, visible flow separation occurs near the ridgeline. Less positive values were observed in the upwind region due to the periodic flow reattachment. Figure 4-12 (a) witness a consistent recirculating flow regime in the downwind half where $\bar{C}_p$ values were appeared to be within -0.4 to -0.8.

When the boundary wall is at a 1H distance apart in either direction, positive values reach even 0.6 along the leading edge (BW2). The corresponding value becomes 0.5 for BW1. Figure 4-12 (b and d) explains the importance of lateral separation distance where maximum positive pressure has changed. Therefore, with boundary walls, flow leads to reattach more than in the isolated conditions. Such variations are not covered

in all four design standards. However, the pressure recovery is absent on the downwind half. Even with boundary walls, the consistency of the zone is not greatly affected.

#### 4.1.3.3. Crosswind slope (R)

Similar to along wind direction, NBCC 2015 suggests a two-zone approach for the crosswind slope. It anticipates a $\bar{C}_p$ value of -1 within 1H distance from the leading edge and -0.5 for the remaining zone. Both ACSE 07 16 and EN 1991-1-4 2005 divide the crosswind slope into four regions. Within 0.5h and 0.5h-1h distance, the American standard provides the same $\bar{C}_p$ value of -0.82. For the remaining zones, it suggests values as -0.44 and -0.24, respectively. Interestingly, the $\bar{C}_p$ value within 0.5h obtained from the wind tunnel has exceeded the recommended value. Nevertheless, the rest of the regions have obtained slightly lower values than the recommendations, implying the codified values are conservative.

EN-1991-1-4 takes a different zoning approach compared to the ASCE 07-16. It isolates the corners and forecasts moderately critical negative values. For instance, Eurocode assumes the $\bar{C}_p$ value of zone F to be -1.75. For zone G and H, the $\bar{C}_p$ value becomes -1.78 and -0.7, respectively. The collected results from the wind tunnel state -1.31 for zone F, -1.18 for zone G, and -0.9 for zone H.

Denser zoning arrangement is provided in AS/NZS 110.2 2011, being more comparable to ASCE recommendations. From the first four zones, it is observed the Australian guidelines are conservative than the American specifications. None of the codes provide positive values towards the trailing edge of the crosswind slope.

The maximum reduction in $\bar{C}_p$ values is observed for BW1, where lateral and upstream separation is 2H. The $\bar{C}_p$ value within 0.5h distance changed from -1.11 to -0.53. For zones, F and G, the recommended coefficients became -0.47 and -1.07 for BW1. For zero lateral separation, $\bar{C}_p$ values of the BW3 have shifted closer towards

the BM. Interestingly, a weak flow reattachment is visible near the trailing edge for BW1. Concerning NBCC 2015, it provides overestimations (-0.5) for the isolated model. The boundary walls resulted in lower negative pressures away from the leading zone (BW1 and BW2). The effective pressure distribution of the cross wind slope is illustrated in Figure 4.13.

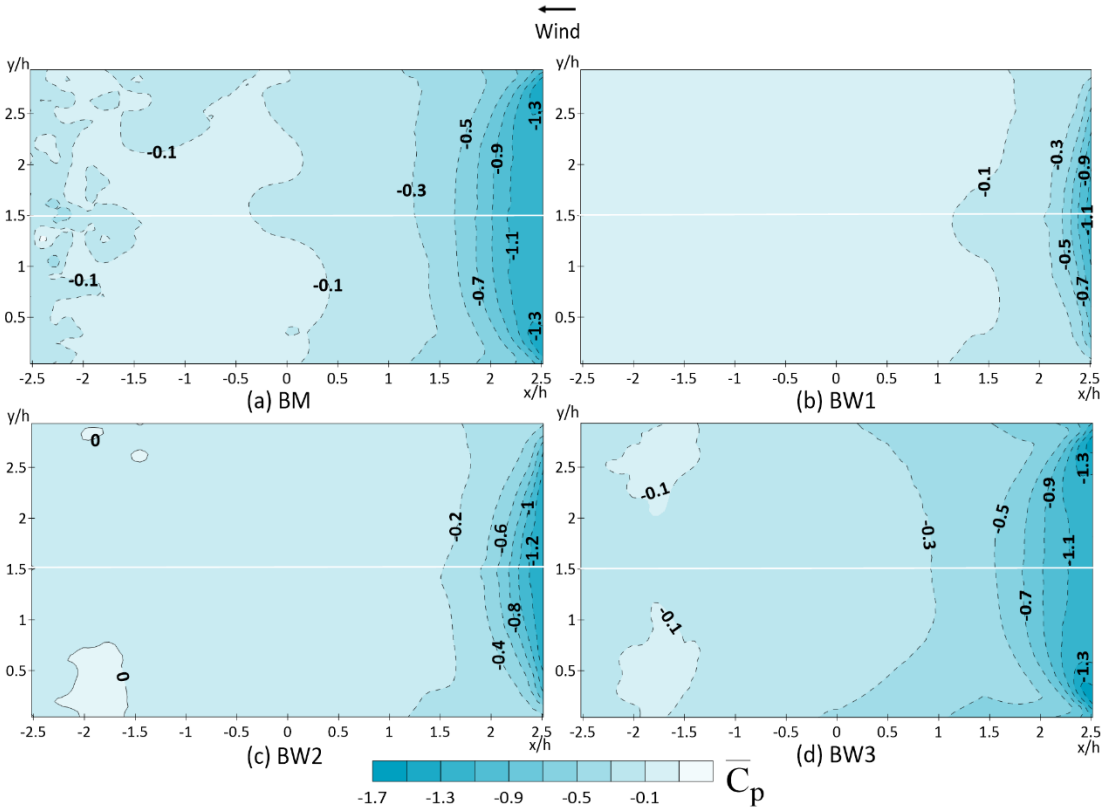


Figure 4.13: $\overline{C}_p$ distribution of the roof at θ =90°

The flow field over the crosswind slope depends on flow separation at the gable edge. However, no discontinuities are present along the crosswind slope towards the trailing edge. Therefore, a reduction of suction values was displayed away from the leading edge. Though, the magnitude of negative pressure is more significant than at θ = 0°.

It was investigated, the same locations, corners and the apex were noticed as critical, according to the study done by Parackal, (2018). A diagonal band of conical vortices could be identified in roof corners and at the apex, intense at oblique wind directions. The addition of boundary walls has caused the negative region to be constricted within

a 0.5h distance. Interestingly, the intensity of the suction at corners is drastically reduced in the presence of BW1 and BW2. However, we noticed a disrupted behavior near the apex, less dependent on the boundary walls. Further, with BW1 and BW2, pressure gradients near the leading edge transformed into critical. Repeatedly, the distribution of BW3 becomes more identical to BM. In addition, BW1 and BW2 influence the latter region of crosswind distribution to be more consistent.

### 4.2 Detailed analysis on the $\bar{C}_p$

For the analysis, we shall consider specifics locations on the roof and walls. Generally, the critical values are observed near sharp edges or discontinuities on low-buildings. Accordingly, the selected positions are marked in Figure 4.14. On the roof, the leading-edge, edge of the gable end, and ridgeline were noted as possible critical locations. For the walls, we have considered the middle and the corner most pressure taps. Each figure will be provided with a 20% error margin compared to BM.

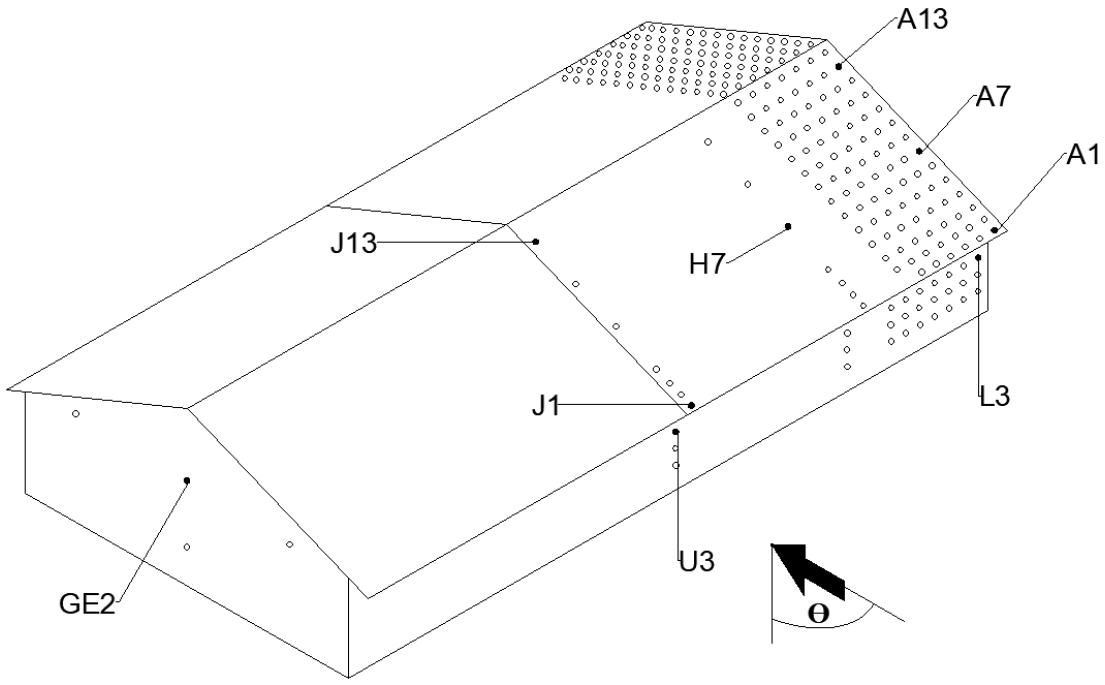


Figure 4.14: Pressure taps, considered for the detailed $\bar{C}_p$ analysis

### 4.2.1 Comparison of $\bar{C}_p$ on roof

It was observed a fair correlation among the corner taps along the leading edge for the Base Model (BM). However, the corner most pressure tap (A1) has recorded moderately pronounced negative $\bar{C}_p$ pressure values for oblique wind directions. Thereby, we shall consider the effect of boundary walls on the pressure tap (A1) shown in Figure 4.15.

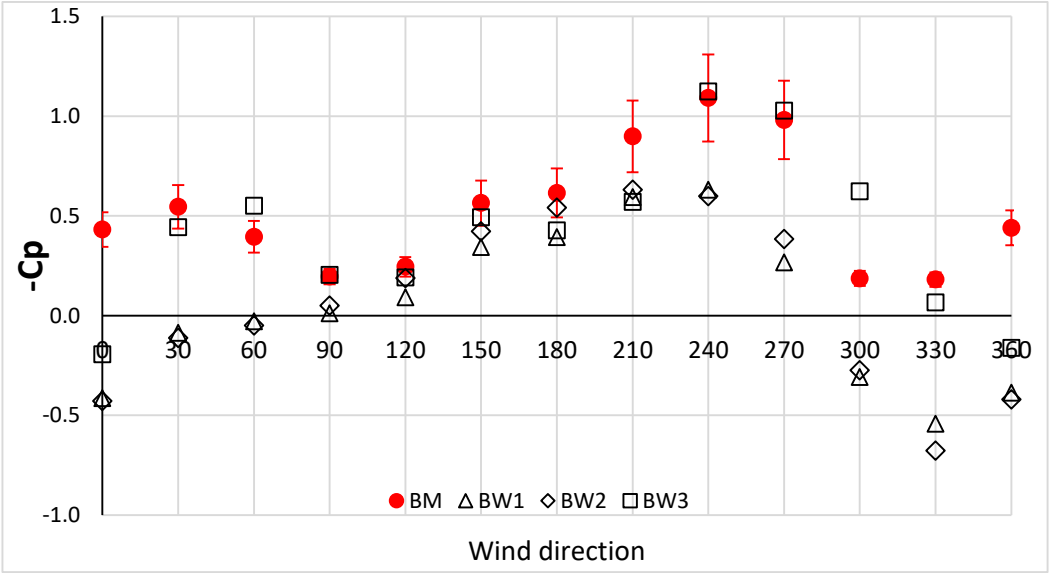


Figure 4.15: Directional variation of $\bar{C}_p$ of A1 tap

Figure 4.15 depicts that the upstream and lateral separation distance has a significant effect on the pressure tap A1. Nevertheless, Boundary Wall 3 (BW3) has caused abrupt variations in the pressure values. For instance, at θ = 0°, all the wall patterns have altered the suction on the BM into a positive value. At θ = 30° it has become a negative value for BW3 similar to BM while BW1 and BW2 recorded slightly pronounced positive values. The critical directions can be identified from θ = 210° to θ = 270° for the low rise building without boundary walls. Except for BW3, BW1 and BW2 have reduced the maximum suction of the BM from -1.1 to -0.6. Further, there exists a strong correlation of the values corresponds to BW1 and BW2 (Pearson correlation coefficient; $R^2$ = 0.98). It implies the pressure coefficients at the corner are less dependent on the separation distance. Overall, the reduction in suction values

explicates that the flow separation is becoming weak in the presence of boundary walls and the effect continues beyond zero to positive values indicating possible flow reattachment. Less pronounced effect on all the patterns can be observed for wind azimuths from θ = 90° to θ = 180°. The pressure tap is located on the recirculating wake for such wind attacks. Even the BW3 has recorded values similar to BM in several directions, the abrupt variations have caused the $R^2$ between the BW3 and BM to become 0.69.

Subsequently, the edge of the gable end was selected to investigate the effect of boundary walls. The isolated model has shown a fair correlation along the gable end from θ = 0° to θ = 180°. Beyond wind azimuth 180°, more disrupt patterns could be observed towards the apex of the ridge. It is witnessed, less pronounced suction values become larger values θ = 210° to θ = 300°. Critical wind direction was found as θ = 210°, where the pressure coefficients have been recorded as -0.89, -1.6, and -3.26 for A1, A7, and A13, respectively. Considering the values exerted, the magnitude of the suction increases towards the ridge, along the gable edge. Except for the correlation at a particular direction, it should be highlighted that the sudden changes are more noticeable than the values observed along the corner most taps of the leading edge. Hence, A7 and A13 taps will have to be investigated to distinguish the influence from boundary walls.

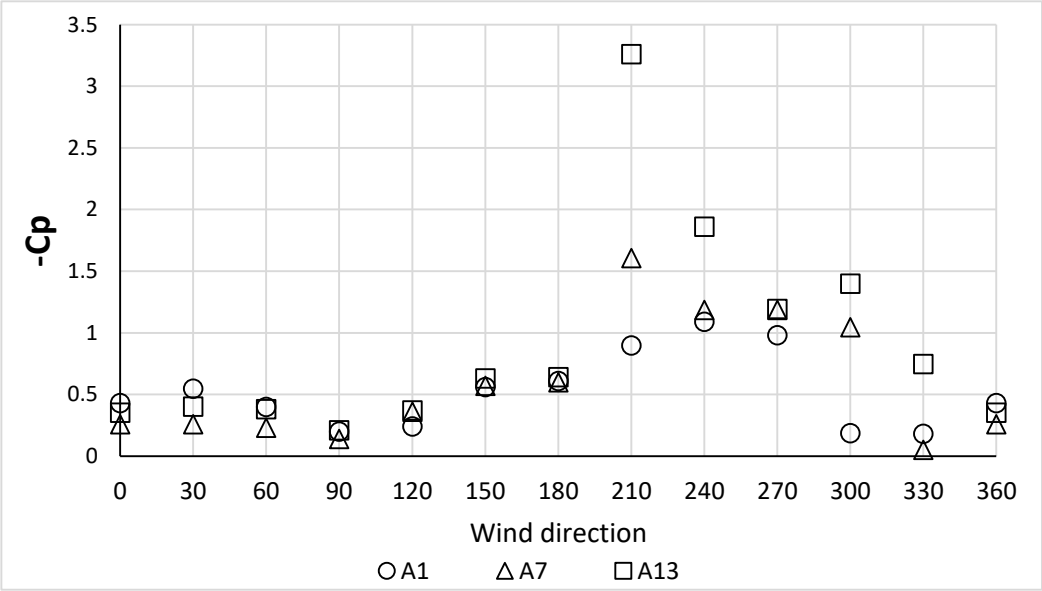

Figure 4.16: Directional variation of $\bar{C}_p$ of A1, A7, and A13 pressure taps of BM

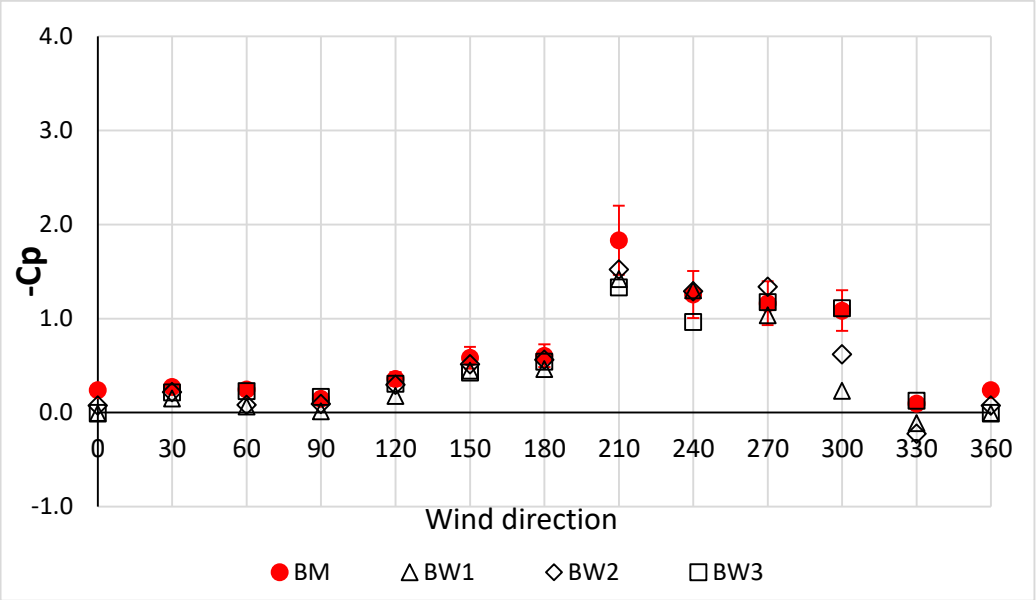


Figure 4.17: Directional variation of $\bar{C}_p$ of A7 tap

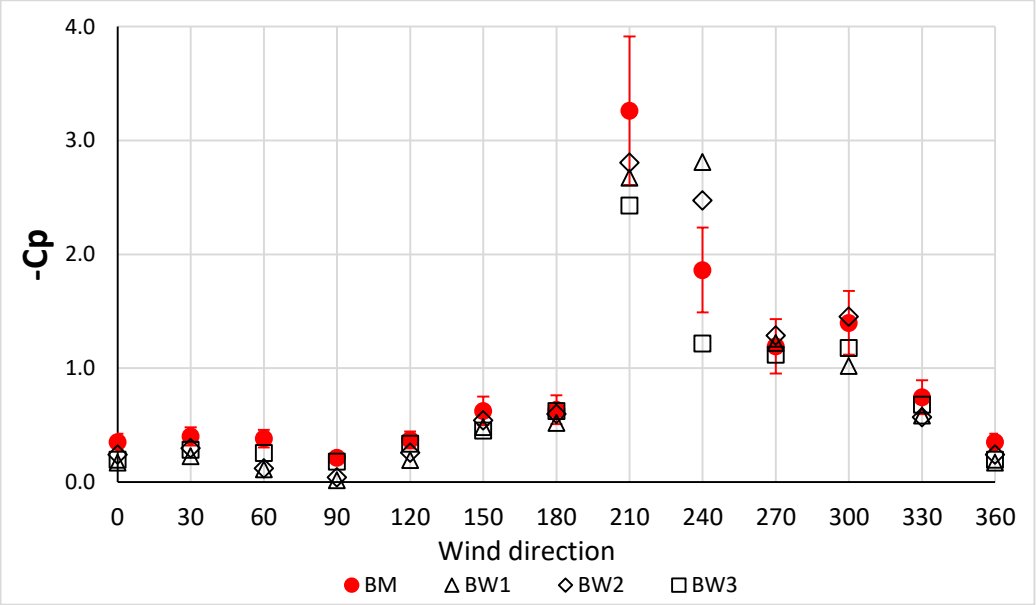


Figure 4.18: Directional variation of $\bar{C}_p$ of A13 tap

Unlike the A1 pressure tap, the effect of boundary walls seems more correlated with the BM from θ = 0° to θ = 180° (Figures 4.17 and 4.18). Here, BW3 has a more

considerable effect on the maximum negative values. Again we would notice a BW1 and BW2 recorded almost similar variation apart from their different lateral and upstream separation distances. Further, the values correspond to wind azimuth 240° of A3 pressure tap have increased in the presence of BW1 and BW2. However, the critical directions are noticed from θ = 210° to θ = 300°. The maximum negative pressure value in the BM for each location lean-to reduces when the boundary walls were placed. Even if the negative values tend to increase toward the ridge, the overall effect of boundary walls appears to become less noticeable compared to the leading edge. It is noteworthy, we have considered half of the roof surface to investigate the modification of the flow field. From pressure taps A1, A7, and A13, it was noticed the critical directions are the oblique wind approaches. Since the pressure tap arrangement near the gable end is symmetric along the ridgeline, a similar variation of $\bar{C}_p$ can be expected on the remaining half for the corresponding locations. However, the critical direction will be flipped across the ridge direction.

Generally, several localized effects had been noticed near the leading edge corner and the apex of the gable end (Parackal, 2018). It would be essential to examine the spatial resolution to distinguish such local effects. Foremost, we shall consider the critical oblique wind attacks from θ = 210° to θ = 300° on both zones simultaneously. Figure 4.19 illustrates the variation of $\bar{C}_p$ on the selected zone. It should be noted, the shaded colour code was defined where the blue colour denotes lower values and the white colour represents higher values. Repeatedly, the variation for BW1 and BW2 signifies a comparable effect on the BM, except for critical wind attacks. Further, the correlation between the BW1 and BW3 has increased in contrast to location A1 along most of the wind direction. It denotes the effect of the lateral separation distance of BW1 might have less effect on the directional variation at the particular location.

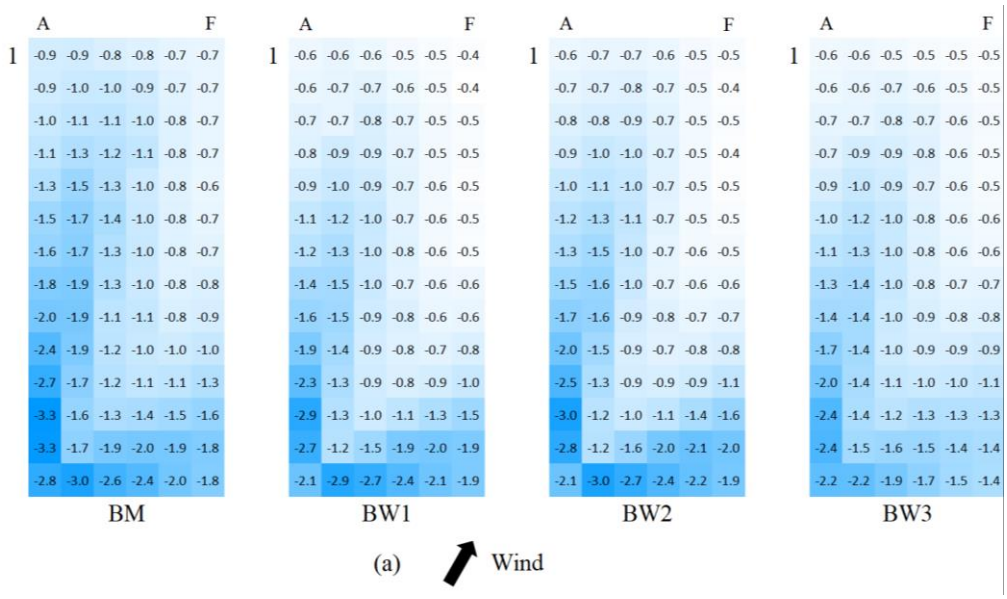
A F
1
-0.9 -0.9 -0.8 -0.8 -0.7 -0.7
-0.9 -1.0 -1.0 -0.9 -0.7 -0.7
-1.0 -1.1 -1.1 -1.0 -0.8 -0.7
-1.1 -1.3 -1.2 -1.1 -0.8 -0.7
-1.3 -1.5 -1.3 -1.0 -0.8 -0.6
-1.5 -1.7 -1.4 -1.0 -0.8 -0.7
-1.6 -1.7 -1.3 -1.0 -0.8 -0.7
-1.8 -1.9 -1.3 -1.0 -0.8 -0.8
-2.0 -1.9 -1.1 -1.1 -0.8 -0.9
-2.4 -1.9 -1.2 -1.0 -1.0 -1.0
-2.7 -1.7 -1.2 -1.1 -1.1 -1.3
-3.3 -1.6 -1.3 -1.4 -1.5 -1.6
-3.3 -1.7 -1.9 -2.0 -1.9 -1.8
-2.8 -3.0 -2.6 -2.4 -2.0 -1.8
BM
-0.6 -0.6 -0.6 -0.5 -0.5 -0.4
-0.6 -0.7 -0.7 -0.6 -0.5 -0.4
-0.7 -0.7 -0.8 -0.7 -0.5 -0.5
-0.8 -0.9 -0.9 -0.7 -0.5 -0.5
-0.9 -1.0 -0.9 -0.7 -0.6 -0.5
-1.1 -1.2 -1.0 -0.7 -0.6 -0.5
-1.2 -1.3 -1.0 -0.8 -0.6 -0.5
-1.4 -1.5 -1.0 -0.7 -0.6 -0.6
-1.6 -1.5 -0.9 -0.8 -0.6 -0.6
-1.9 -1.4 -0.9 -0.8 -0.7 -0.8
-2.3 -1.3 -0.9 -0.8 -0.9 -1.0
-2.9 -1.3 -1.0 -1.1 -1.3 -1.5
-2.7 -1.2 -1.5 -1.9 -2.0 -1.9
-2.1 -2.9 -2.7 -2.4 -2.1 -1.9
BW1
-0.6 -0.7 -0.7 -0.6 -0.5 -0.5
-0.7 -0.7 -0.8 -0.7 -0.5 -0.4
-0.8 -0.8 -0.9 -0.7 -0.5 -0.5
-0.9 -1.0 -1.0 -0.7 -0.5 -0.4
-1.0 -1.1 -1.0 -0.7 -0.5 -0.5
-1.2 -1.3 -1.1 -0.7 -0.5 -0.5
-1.3 -1.5 -1.0 -0.7 -0.6 -0.5
-1.5 -1.6 -1.0 -0.7 -0.6 -0.6
-1.7 -1.6 -0.9 -0.8 -0.7 -0.7
-2.0 -1.5 -0.9 -0.7 -0.8 -0.8
-2.5 -1.3 -0.9 -0.9 -0.9 -1.1
-3.0 -1.2 -1.0 -1.1 -1.4 -1.6
-2.8 -1.2 -1.6 -2.0 -2.1 -2.0
-2.1 -3.0 -2.7 -2.4 -2.2 -1.9
BW2
-0.6 -0.6 -0.5 -0.5 -0.5 -0.5
-0.6 -0.6 -0.7 -0.6 -0.5 -0.5
-0.7 -0.7 -0.8 -0.7 -0.6 -0.5
-0.7 -0.9 -0.9 -0.8 -0.6 -0.5
-0.9 -1.0 -0.9 -0.7 -0.6 -0.5
-1.1 -1.3 -1.0 -0.8 -0.6 -0.6
-1.3 -1.4 -1.0 -0.8 -0.7 -0.7
-1.4 -1.4 -1.0 -0.9 -0.8 -0.8
-1.7 -1.4 -1.0 -0.9 -0.9 -0.9
-2.0 -1.4 -1.1 -1.0 -1.0 -1.1
-2.4 -1.4 -1.2 -1.3 -1.3 -1.3
-2.4 -1.5 -1.6 -1.5 -1.4 -1.4
-2.2 -2.2 -1.9 -1.7 -1.5 -1.4
BW3

(a) Wind

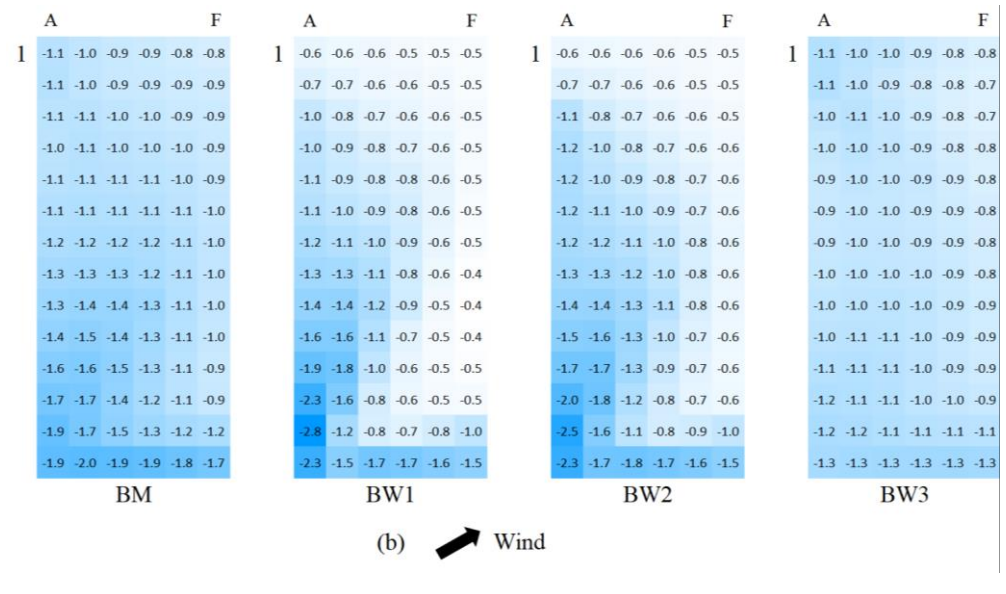
A F
1
-1.1 -1.0 -0.9 -0.9 -0.8 -0.8
-1.1 -1.0 -0.9 -0.9 -0.9 -0.9
-1.1 -1.1 -1.0 -1.0 -0.9 -0.9
-1.0 -1.1 -1.0 -1.0 -1.0 -0.9
-1.1 -1.1 -1.1 -1.1 -1.0 -0.9
-1.1 -1.1 -1.1 -1.1 -1.1 -1.0
-1.2 -1.2 -1.2 -1.2 -1.1 -1.0
-1.3 -1.3 -1.3 -1.2 -1.1 -1.0
-1.3 -1.4 -1.4 -1.3 -1.1 -1.0
-1.4 -1.5 -1.4 -1.3 -1.1 -1.0
-1.6 -1.6 -1.5 -1.3 -1.1 -0.9
-1.7 -1.7 -1.4 -1.2 -1.1 -0.9
-1.9 -1.7 -1.5 -1.3 -1.2 -1.2
-1.9 -2.0 -1.9 -1.9 -1.8 -1.7
BM
-0.6 -0.6 -0.6 -0.5 -0.5 -0.5
-0.7 -0.7 -0.6 -0.6 -0.5 -0.5
-1.0 -0.8 -0.7 -0.6 -0.6 -0.5
-1.0 -0.9 -0.8 -0.7 -0.6 -0.5
-1.1 -0.9 -0.8 -0.8 -0.6 -0.5
-1.1 -1.0 -0.9 -0.8 -0.6 -0.5
-1.2 -1.1 -1.0 -0.9 -0.6 -0.5
-1.3 -1.3 -1.1 -0.8 -0.6 -0.4
-1.4 -1.4 -1.2 -0.9 -0.5 -0.4
-1.6 -1.6 -1.1 -0.7 -0.5 -0.4
-1.9 -1.8 -1.0 -0.6 -0.5 -0.5
-2.3 -1.6 -0.8 -0.6 -0.5 -0.5
-2.8 -1.2 -0.8 -0.7 -0.8 -1.0
-2.3 -1.5 -1.7 -1.7 -1.6 -1.5
BW1
-0.6 -0.6 -0.6 -0.6 -0.5 -0.5
-0.7 -0.7 -0.6 -0.6 -0.5 -0.5
-1.1 -0.8 -0.7 -0.6 -0.6 -0.5
-1.2 -1.0 -0.8 -0.7 -0.6 -0.6
-1.2 -1.0 -0.9 -0.8 -0.7 -0.6
-1.2 -1.1 -1.0 -0.9 -0.7 -0.6
-1.2 -1.2 -1.1 -1.0 -0.8 -0.6
-1.3 -1.3 -1.2 -1.0 -0.8 -0.6
-1.4 -1.4 -1.3 -1.1 -0.8 -0.6
-1.5 -1.6 -1.3 -1.0 -0.7 -0.6
-1.7 -1.7 -1.3 -0.9 -0.7 -0.6
-2.0 -1.8 -1.2 -0.8 -0.7 -0.6
-2.5 -1.6 -1.1 -0.8 -0.9 -1.0
-2.3 -1.7 -1.8 -1.7 -1.6 -1.5
BW2
-1.1 -1.0 -1.0 -0.9 -0.8 -0.8
-1.1 -1.0 -0.9 -0.8 -0.8 -0.7
-1.0 -1.1 -1.0 -0.9 -0.8 -0.7
-1.0 -1.0 -1.0 -0.9 -0.8 -0.8
-0.9 -1.0 -1.0 -0.9 -0.9 -0.8
-0.9 -1.0 -1.0 -0.9 -0.9 -0.8
-0.9 -1.0 -1.0 -0.9 -0.9 -0.8
-1.0 -1.0 -1.0 -1.0 -0.9 -0.8
-1.0 -1.0 -1.0 -1.0 -0.9 -0.9
-1.0 -1.1 -1.1 -1.0 -0.9 -0.9
-1.1 -1.1 -1.1 -1.0 -0.9 -0.9
-1.2 -1.1 -1.1 -1.0 -1.0 -0.9
-1.2 -1.2 -1.1 -1.1 -1.1 -1.1
-1.3 -1.3 -1.3 -1.3 -1.3 -1.3
BW3

(b) Wind

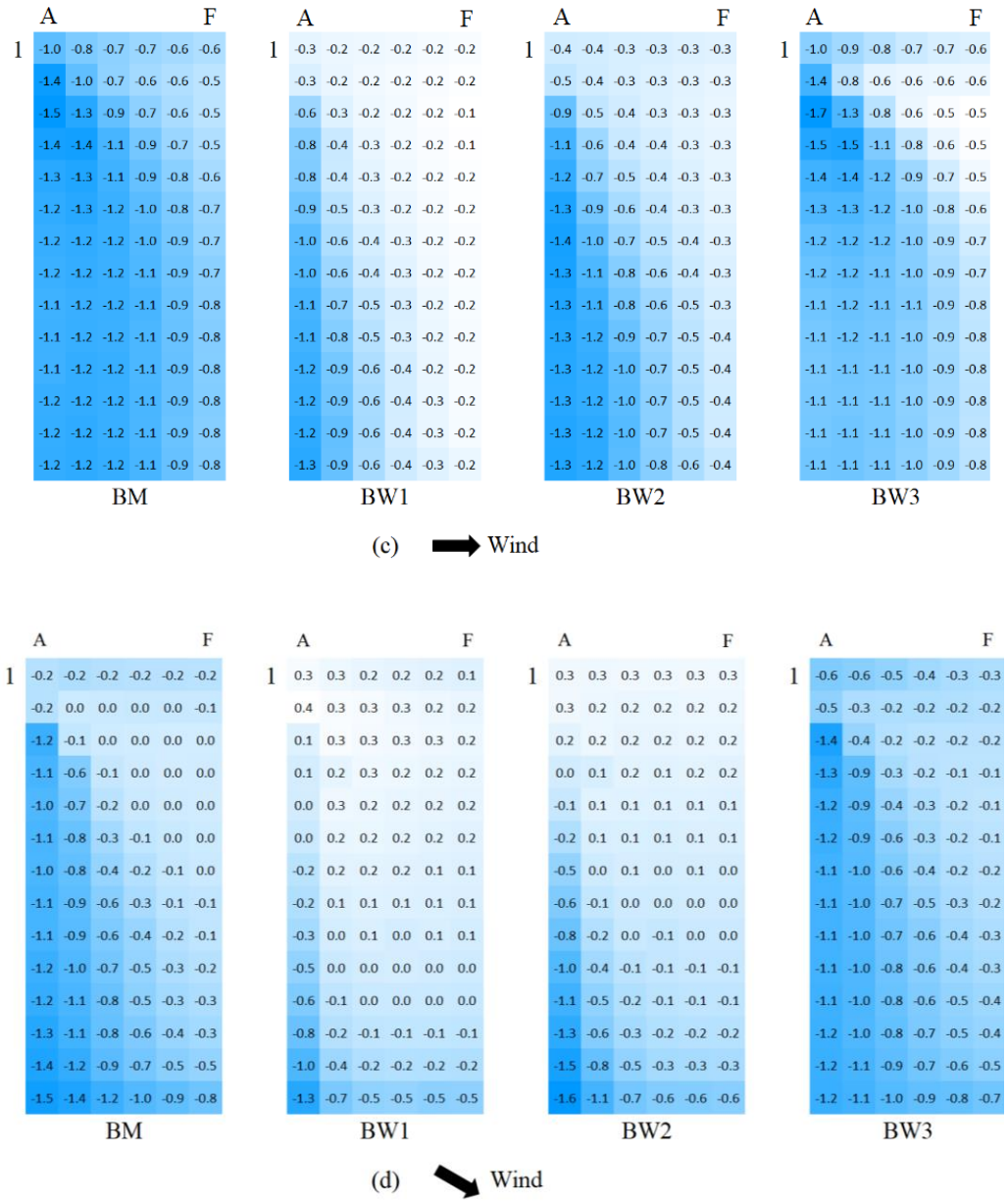


Figure 4.19: Spatial resolution of $\bar{C}_p$ of (a) θ = 210°, (b) θ = 240°, (c) θ = 270°, and (d) θ = 300°

Interestingly, it witnesses the statement that the corner regions are subjected to relatively large negative pressure values. For θ = 210°, the apex of the gable end experienced larger negative pressure values. And the values are appearing to be reduced towards the interior zones. It is possible to observe that the intense negative values are formed in the diagonal direction according to Figure 4.19(a). It has been beheld, it contains a band of vortices formed diagonally. The values reveal a more

disrupted behavior can be observed near the apex. As identified before, the effect of boundary walls appeared to be correlated along the gable ends for several wind attacks. However, we can observe that maximum suction tends to reduce in the presence of boundary walls. The maximum value of the A13 pressure tap, -3.3 for the BM becomes -2.8 when the upstream and lateral separation is equal to 1H. It becomes -2.7 for BW1 whose separation distances are 2H away from the building. Further, the value has decreased up to -2.4 for BW3 which consists of zero lateral separation distance and 2H upstream separation. It shall be noted, boundary walls have not altered the pattern but its magnitude. Overall the intensity of the diagonal band of vortices has a positive effect on the boundary walls. Still, the pressure taps near the A1 pressure tap have experienced less pronounced suction values.

The event noticed at the A13 pressure tap is further explained in Figure 4.19(b) at $\theta$ = 240°. The maximum negative pressure had decreased in the presence of BW1 and BW3. It is visible that the intensity of the diagonal vortices near the apex has reduced for the above two patterns. However, with zero lateral separation distance, BW3 has been able to reduce the maximum negative pressure near the apex. Interestingly, the interior zones of the BW1 and BW2 contain relatively low negative pressure values than those of the BM and BW3. Interior zones of the BW3 have comparable values in contrast to the values of the BM. Therefore, BW1 and BW2 have influenced some relatively large adverse pressure gradients near the apex compared to the BM and even BW3.

For both occasions, $\theta$ = 210° and $\theta$ = 240°, a zone near to the A1 tap has exerted less noticeable negative values concerning the zone near the apex. For the wind azimuth of 270°, both regions become critical simultaneously. Thus it seems, the diagonal bands of vortices are now formed near to the corner of the leading edge at the eave's level. On a contrary, the values tend to reduce towards the apex of the roof. With the effect of BW1 and BW2, the intensity of conical vortices has substantially reduced. The maximum negative pressure at the corner of the leading edge (-1.5) has become -0.6 and -0.9 for the corresponding wall patterns 01 and 02. However, BW3 had very less

effect on the marked variation of BM allowing the formation of diagonal vortices. As well the interior zones of BW3 have a good correlation with the values of the BM.

The same effect was present for the wind direction θ = 300° due to the cornering effect (Figure 4.19(d)). Similar to the variation obtained for θ = 270°, BW1, and BW2 decrease the intense negative values while BW3 has resulted in slightly higher values in contrast to BM. Interestingly, the interior zones of BW1 and BW2 have obtained positive pressure values which were not observed on either of previous occasions. In addition, noticeable negative pressure values could be observed towards the apex of the roof for all building configurations including BM.

Overall, the severity of oblique wind directions was discussed and it was found the apex of the gable end becomes more critical when the critical negative pressure values are considered. In essence, the cornering effect could influence considerable negative values near the leading edge corner but less pronounced compared to the ridge zone. Parackal, (2018) has emphasized the variation of the negative pressure at those two zones could be due to the effect of roof pitch. Due to the height difference between the eave level and the ridge level, more disrupted vortex formation was anticipated near the apex of the gable end along with higher turbulence fluctuations.

Nevertheless, constructing boundary walls could alter the intensity of the negative pressure values. For the ridge zone, the effect of BW3 was identified as the most effective among the other patterns. Near to the leading edge corner, the effect of BW1 and BW2 becomes significant. The reduction of suction could be due to the weaker flow separation induced by the lateral and upstream separation. BW1 and BW3 for θ = 210° indicated, not even the lateral separation distance but the upstream separation could affect the pressure variation induced at oblique wind attacks. The weaker flow separation has contributed to reducing the intensity of intermittent vortex and eddy formation as illustrated in Figure 4.19, especially at the leading corner. The disrupted nature near the apex is witnessed by the less affected suction values. As identified by Parackal, (2018), these vortex formations can induce progressive failures initiating at corners. Therefore, it is highlighted the positive impact of having a boundary wall in the near vicinity and the flow modification.

Next, we considered the effect of the pressure coefficient along the ridgeline towards the interior zone. The interior zone was not entirely installed using pressure taps. Therefore, to represent internal zones, the H7 location was selected. The directional variation of $\bar{C}_p$ is displayed below in Figure 4.20.

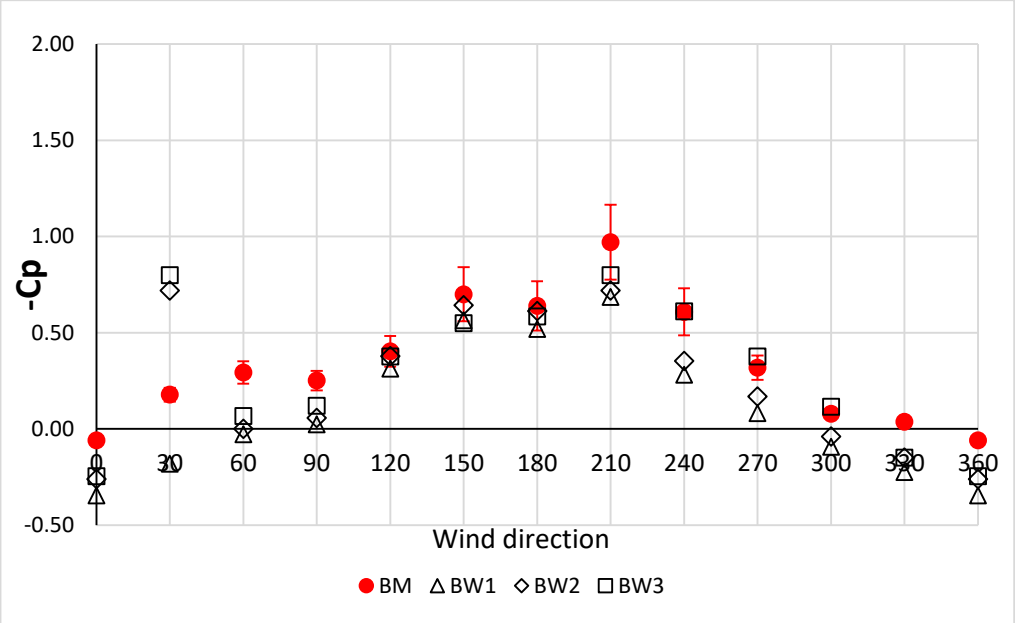


Figure 4.20: Directional variation of $\bar{C}_p$ of H7 tap

From the above figure, the variation of $\bar{C}_p$ shows a comparable difference with location A1. The critical direction remains at θ = 210° for BM and the negative values of other critical directions observed for A1 tend to decrease. As well, the effect of flow separation was observed at the edges for windblown from upstream (θ = 0°). However, towards the interior zones, weaker flow reattachments are seen even for the BM. Pressure taps H7 and A7 tare located on the same horizontal line (parallel to the ridge). The $\bar{C}_p$ values correspond to wind azimuths 210°, 240°, and 270° for the H7 has become -1, -0.6, and -0.38 from the initial values of A7, -1.6, -1.2, and -1.2. Thus it is convinced the pressure variation is altered along the horizontal line for the building without boundary walls.

The effect of boundary walls appeared to be slightly noticeable for the H7 location. The intensity of the weaker flow reattachment is magnified in the presence of all three

wall patterns. For wind azimuth θ = 30°, negative pressure for the BW2 and BW3 has increased abruptly. It was noticed, the effect of all patterns convince the less dependency on the lateral separation and the distance of separation most of the time. However, the overall reduction in the magnitude of $\bar{C}_p$ is more than 20% of the values corresponds to BM. Heretofore we discussed the corner zones and the interior zones using representative pressure taps. Thereafter, location J1 was selected to be investigated. The directional pressure variation is illustrated in Figure 4.21.

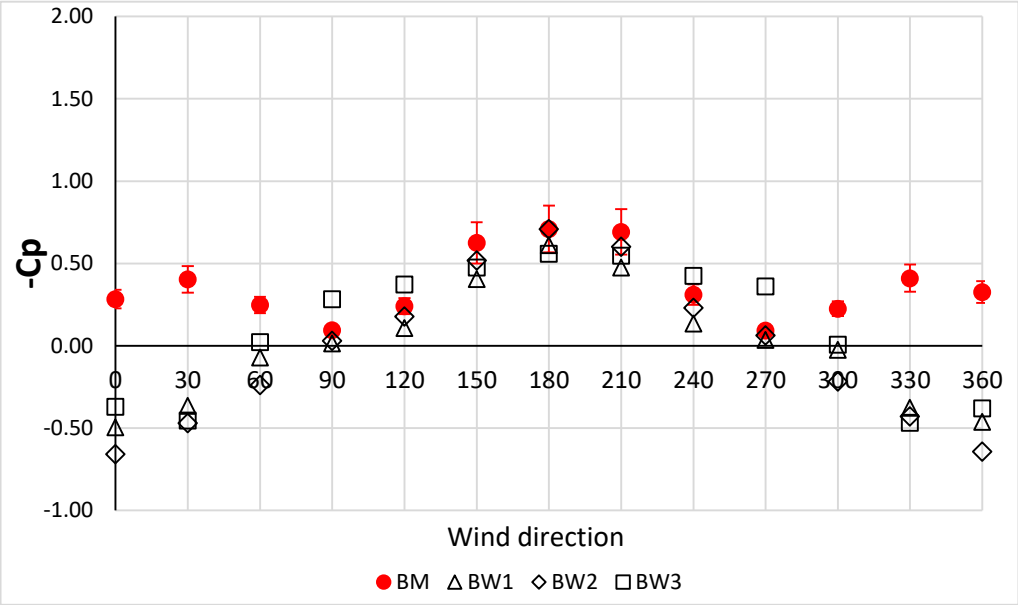


Figure 4.21 Directional variation of $\bar{C}_p$ of J1 pressure tap

Symmetric pressure distribution was observed at the J1 location. Negative pressure entirely dominates the building without any boundary wall. Wind azimuths θ = 0° and θ = 180° induce relatively pronounced negative pressure values. At θ = 180°, the location is placed on the trailing edge of the roof. Moderately, less pronounced suction appeared at θ = 0° wind direction. Corresponding values at A1 (-0.43) and J1 (-0.28) indicate the flow separation becomes weak towards the middle along the leading edge. On a contrary, J1 becomes critical at θ = 180°, indicating the negative pressure higher than at the corners (A1). However, the critical oblique directions identified at A1 were not noticeable here. It is interesting to observe, the near reattachments occur at crosswind directions θ = 90° and θ = 270°. No Sudden variations were noted compared

to earlier locations. From θ = 150° to θ = 210° critical values become more uniform unlike at the interior locations (H7).

For the models with boundary walls, negative values decrease especially at (θ = 0°). The weaker flow separation has transformed into flow reattachment in the presence of boundary walls. The values of BM (-0.28) becomes 0.49 for BW1, 0.66 for BW2 and 0.37 for BW3. Therefore, the 1H upstream and lateral separation has influenced the most effect on the corresponding value of the BM. The effect becomes less significant towards the wind direction θ = 90°. Along the critical directions, a slight reduction in negative pressure is observed for all boundary wall patterns. Especially between θ = 120° and θ = 240° correlation among the wall patterns is high. There it leads to assuming that the effect of separation distance and the lateral separation becomes less considerable. BW3 has recorded several negative values larger than those of BM for crosswinds.

Next, we discuss the effect of boundary walls at the pressure tap J13, located near the ridgeline along the middle frame (see Figure 4.22).

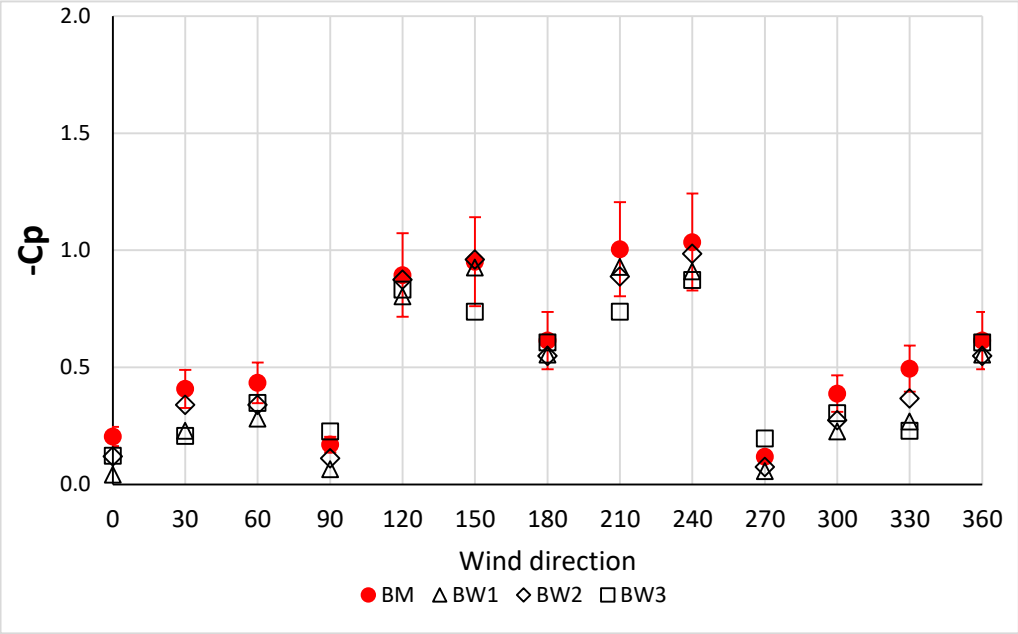


Figure 4.22: Directional variation of $\bar{C}_p$ of J13 pressure tap

Neggative pressure appeared to be forming in all directions for the BM as shown above. From $\theta = 270°$ to $\theta = 90°$ in clockwise direction, the maximum negative values recorded as -0.61. For those wind attacks, the selected pressure tap is located on the upwind half of the roof. From $\theta = 90°$ to $\theta = 270°$ in a clockwise direction, it is located on the downwind half of the roof. There, we identified more noticeable negative values were occurring behind the ridgeline. Further, the variation is almost uniform except at $\theta = 180°$. Compared to the J1 pressure tap, the critical values have even exist beyond -1. It might indicate the separation occurs at the ridgeline. There is a significant drop in the negative pressure after $\theta = 240°$, and almost becomes closer to zero. The pressure taps A13 and J13 are located along the same line parallel to the ridge direction. Hence, it is observed that the more noticeable suction values at the corners become less critical towards the middle frame. Not only the critical values but the critical directions have also changed. Mainly, along winds have become significant towards the middle zones, compared to crosswinds.

Boundary walls have effectively reduced the negative values beyond 20% of the values of BM, most of the time. The correlation of boundary walls with the BM has increased significantly compared to the J1 pressure tap. Thus, it convinces a greater effect of boundary walls is obtained along the leading edge rather than towards the interior zones. Nevertheless, none of the boundary wall patterns has contributed to positive values at the J13 tap.

### 4.2.2 Comparison of mean wind pressure coefficients on walls

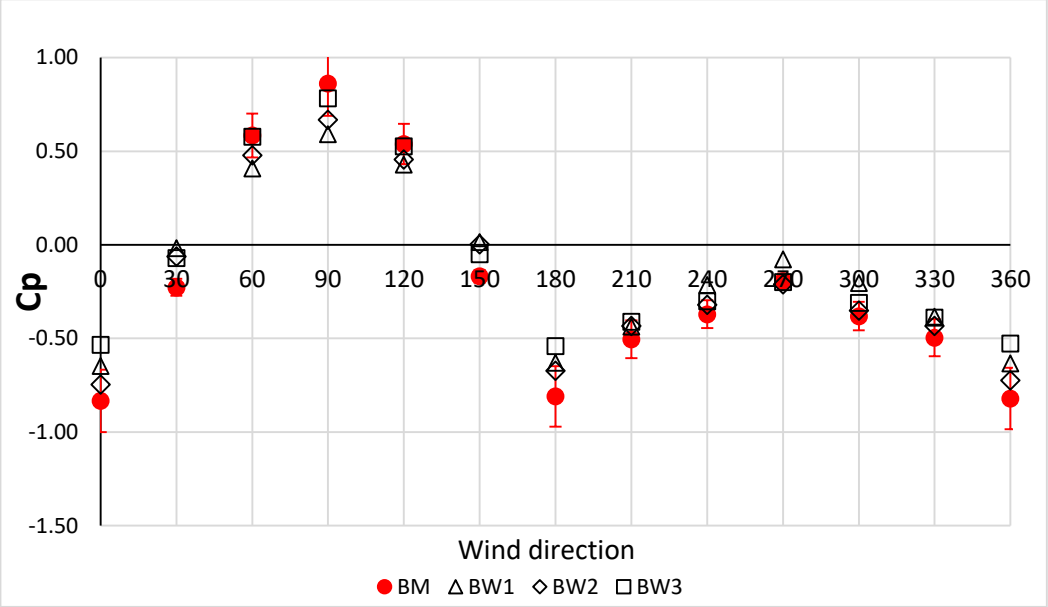


Figure 4.23: Directional variation of $\bar{C}_p$ of GE2 pressure tap

The variation of $\bar{C}_p$ of the middle (GE2 tap) of the gable wall is shown in Figure 4.23 The variation is markedly different from the $\bar{C}_p$ recorded on the roof. At θ = 0° and θ = 180° the maximum negative pressure exert on the middle of the gable wall for the BM. At θ = 90°, maximum positive pressure occurs in the same location. From θ = 180° to θ = 360° in the clockwise direction, a gradual variation of negative pressure is observed. The maximum suction of the BM (-0.81) and becomes -0.96 at the corner of the gable wall.

However, the $\bar{C}_p$ values reduce their magnitude in the presence of boundary walls. At θ = 0°, the corresponding $\bar{C}_p$ values of the base model (-0.83) becomes -0.74 for BW1, -0.64 for BW2 and -0.53 for BW3. According to Figure 4.23, the values have decreased beyond 20% for some instances. In addition, the correlation is above 0.9 between each pattern and BM. Thus, it implies the boundary walls greatly influence the magnitude of the $\bar{C}_p$ rather than the variation of $\bar{C}_p$. Upstream separation distance and lateral separation distance have a less notable effect on them $\bar{C}_p$ at the GE2

location. The above variation was a bit similar to the corner most tap of the gable wall. However, the maximum negative pressure has increased as stated before. Besides, the impact of boundary wall patterns was noticeable compared to the GE2 location. At θ = 180° the $\bar{C}_p$ model of the BM (-0.81) becomes -0.67 for BW1 and BW2, and -0.54 for BW3 at the middle of the wall. The corresponding value of the BM at the corner -0.96 has decreased to -0.74 for BW2, -0.63 for BW1, and -0.42 for BW3.

After analysing the effect on the gable wall, it was continued to the longwall. Figure 4.24 and Figure 4.25 depicts the variation of $\bar{C}_p$ of U3 and L3 locations.

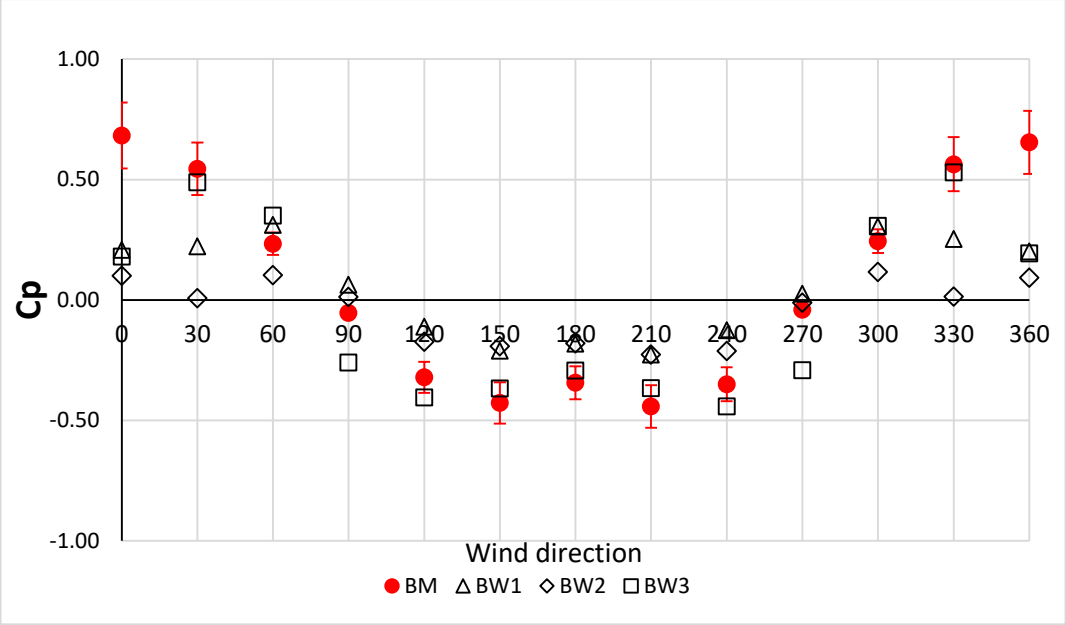


Figure 4.24: Directional variation of $\bar{C}_p$ of U3 pressure tap

Comparable symmetric distribution of $\bar{C}_p$ values was observed on the middle taps of the longwall. From θ = 270° to θ = 90°, positive pressure governs on the surface of the longwall. At θ = 180°, the wall is facing directly to the turbulence wake. It was noted that the negative values are less noticeable at θ = 90° and θ = 270° arrangement. From θ = 120° and θ = 240°, a uniform variation of critical negative values are present.

In the presence of BW1 and BW2, negative pressure tends to reduce. Likewise, the correlation between BW1 and BW2 is higher from θ = 120° and θ = 240°, implying

that near wake distribution is less dependent on the separation distance. Especially for along wind attacks ($\theta = 270°$ to $\theta = 90°$ clockwise) the BW1 and BW2 alter the positive pressure on the BM. However, BW3 follows a similar $\bar{C}_p$ variation to the BM. Interestingly, at $\theta = 0°$, BW1, and BW3 show strong independence on the lateral separation distance. Variations of $\bar{C}_p$ with and without boundary walls on the building walls show good linearity. The cross-correlation coefficients between the BM and patterns have exceeded 0.85.

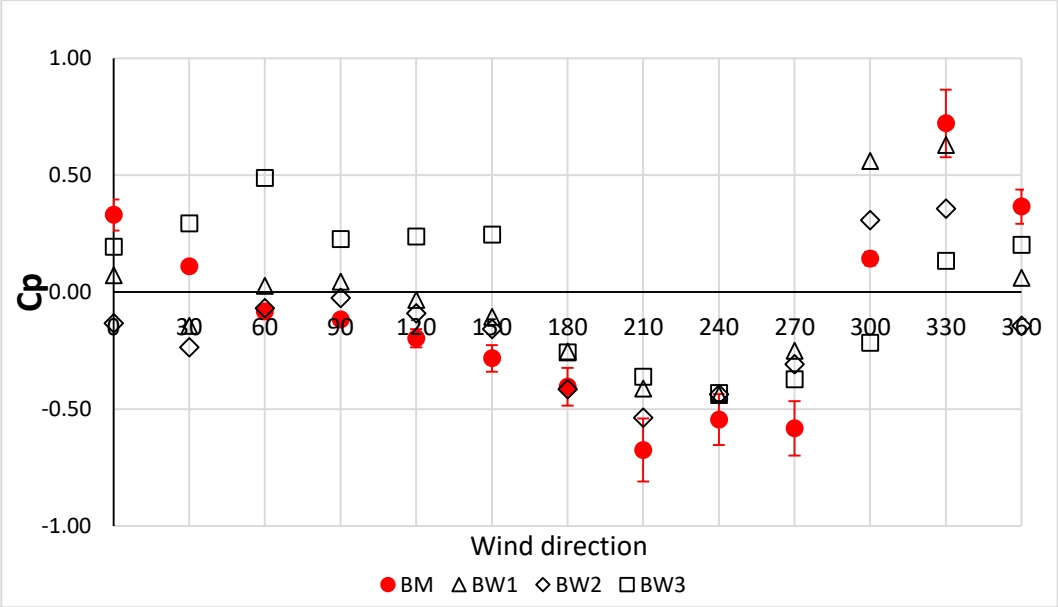


Figure 4.25: Directional variation of $\bar{C}_p$ of L3 pressure tap

A markedly different $\bar{C}_p$ variation was present at the L3 location. Except along several directions, negative pressure values were more often at the corner of the longwall (L3). We noticed the negative pressure becomes critical at $\theta = 210°$ (-0.67).

For the building with boundary walls, negative pressure at the corner decreased. The maximum suction (-0.67) for the BM was reduced to -0.53 for BW2, -0.41 for BW1, and -0.36 for BW3. It is noteworthy the $\bar{C}_p$ values have more disordered behavior for BW3. The correlation with BM becomes 0.83 for BW1, 0.77 for BW2, and 0.57 for BW3. In addition, BW1 and BW2 show less correlation with the values observed for

BW3. Hence, it is evident that the boundary walls alter both distribution and the magnitude of $\bar{C}_p$ at the corner of the longwall. The critical $\bar{C}_p$ values at the corner of the longwall anyway were compared to the observations on the roof.

### 4.3 Time history analysis

The spatial distribution is exhibited by the mean values of the time history for each run. We have taken the ensemble average from the time histories to improve the accuracy. However, the temporal variation is not often analogous to the mean variation on the envelope. The standard deviation and the peak of the time history are crucial in the estimation of design pressure. The peak pressure coefficient ($\widetilde{C_P}$ and $\widehat{C_P}$ )and RMS pressure coefficient $C_{\sigma P}$ can be obtained as given in Eq. (2.8) and (2.9). $C_{\sigma P}$ measures the range of the pressure values at a particular point. Higher RMS values can be expected where high turbulence intensities are occurring. The peak pressure coefficient gives the maximum or the minimum value within the observation period. As similar to mean pressure, the peaks will be defined over a specific interval. This study considered the peak pressures occurring in 10 minutes period in full scale. The analogy of the mean pressure is not applicable for dealing with peak pressure. Because the peak events are not simultaneous in nature. Generally, minimum pressure values are considered on the roofs. The combined effect of internal pressure and external pressure creates large uplift forces. For the comparison of walls, both ($\widetilde{C_P}$ and $\widehat{C_P}$ ) were employed.

### 4.4 Moving peak events

Peak events generally exhibit a rapidly fluctuating nature, both spatially and temporally. The zones which contain peak events are transient and moving on the surface, forming intermittent vortices and eddies. Thus, it witnesses the vulnerability along the building surface due to the moving peak events. These zones primarily

consist of eddies and vortices due to the flow separation. Therefore, negatively pressurized areas are considered in this section.

Peaks have different time lags, which shall be discussed in the latter sections. Foremost we will consider distinct vortex and eddy formations on the roof surface, emphasizing their transient nature. Throughout the mean pressure comparison, the ridgeline, the apex of the gable end, leading-edge corner seemed to have more negative values relative to the rest of the locations. Therefore, it's wise to isolate such areas along the critical direction to study the moving peak events. The following Figures 4.26-30 depict four-time steps of critical events. Each time step is equivalent to 0.2 s in full scale.

Figure 4.26 depicts the critical values for the 180 wind azimuth. These sensors are located in the downwind slope relative to the wind azimuth. Wind flow reaches the ridgeline and passes over it, creating separated bubbles. Such separation can cause high suction near the ridgeline as indicated in time step 01. While the intensity near the ridgeline disappears, the vortices and eddies move down towards the trailing edge. As it is observed, the intensity of the negative peaks is reduced and distributed over the noted area. The eddies can create a band of negative pressure as they move downwards. Thus, it confirms these peak events roll over the surface inducing

differential loading (Blue colour represent lower $\widetilde{C_P}$ values and white colour for higher $\widetilde{C_P}$ values).

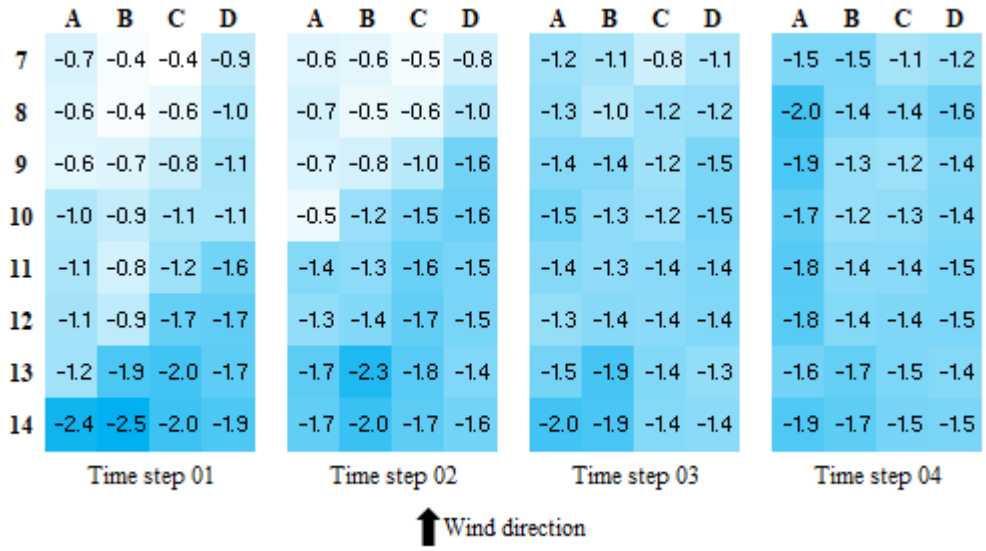


Figure 4.26: Moving peak events near roof corners at θ = 180°

Figure 4.27 depicts the critical values occurring along the gable edge near the apex at θ = 270°. Flow separation starts at the leading edge, forming eddies and vortices moving parallel to the ridge direction. In the 1st time step, a band of negative pressure can be seen to have formed along the edge. Then, it gradually starts moving along the wind direction. However, the peaks become less critical when they move across the roof. Thus, it confirms the gable edge is susceptible to sudden peak events.

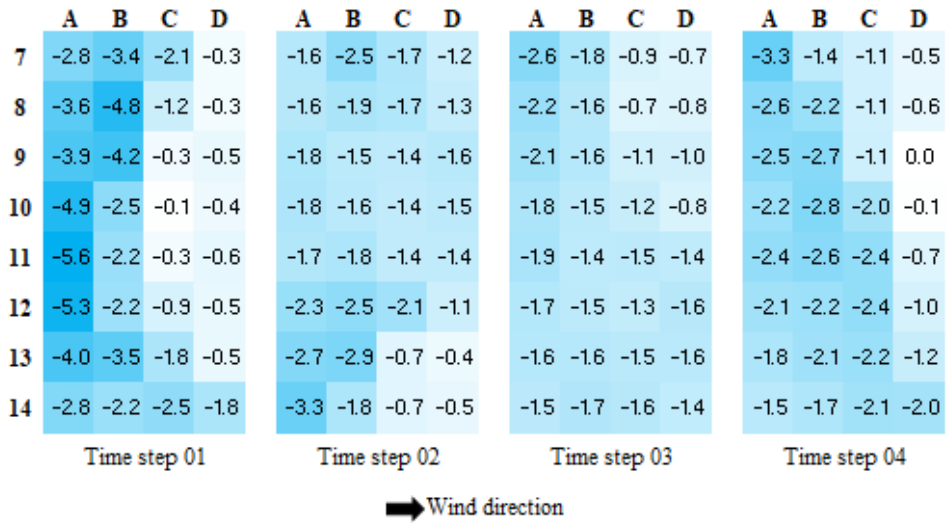


Figure 4.27: Moving peak events near roof corners at θ = 270°

During the analysis, we identified the diagonal bands of vortices along oblique wind directions. Similarly, that variations have been illustrated concerning gradual time steps of 0.2 s (Full-scale), shown in Figures 4.28 and 4.29. Unlike the vortex and moving peak events in the earlier two cases, these formations display a stable diagonal arrangement. Even the peaks occurring near the apex are more disrupt, shown in Figure 4.28. Therefore, these will form a significant pressure gradient in oblique directions on the roof surface. Thus, the wind cannot overcome the large pressure gradient occurring in the diagonal directions.

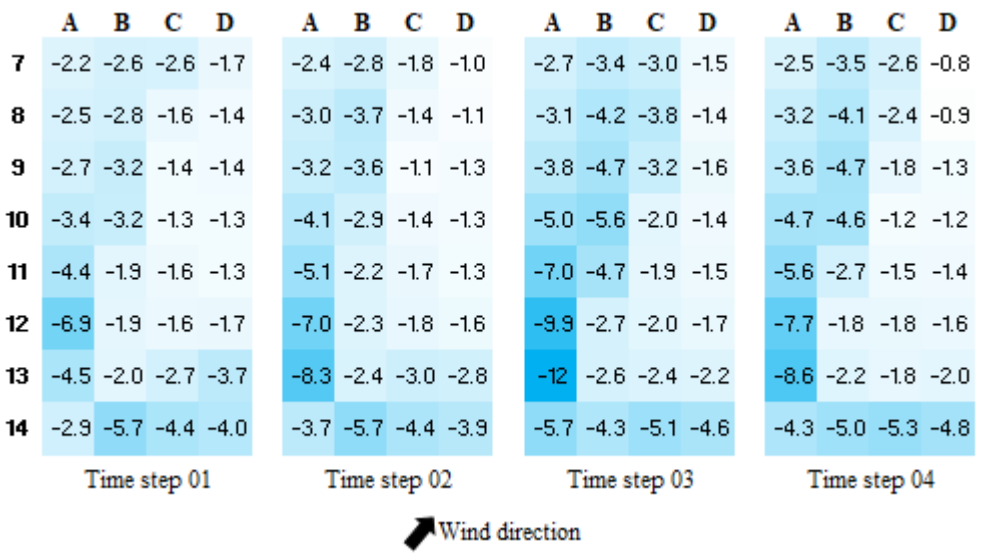


Figure 4.28: Moving peak events near roof corners at θ = 210°

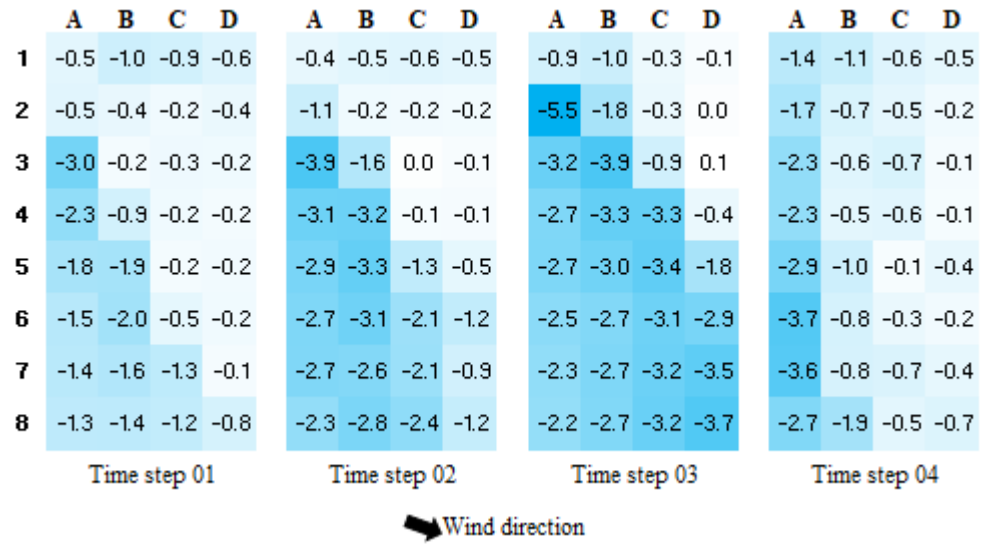


Figure 4.29: Moving peak events near roof corners at θ = 300°

Flow separation and reattachment were observed even on the walls of the low-rise building. Especially, critical values are often perceived for sidewall configuration. Figure 4.30 displays the moving negative pressure on adjacent time steps. The pressure tap line (L) is located closer to the vertical leading edge. Therefore, it could capture moderately large negative pressure values. Besides, these peaks were less significant

in contrast to peak values that appeared on the roof structure. However, the critical values appear to be moving along the surface, parallel to the wind direction. The intensity of the vortex and eddies reduced near to the pressure tap line Q.

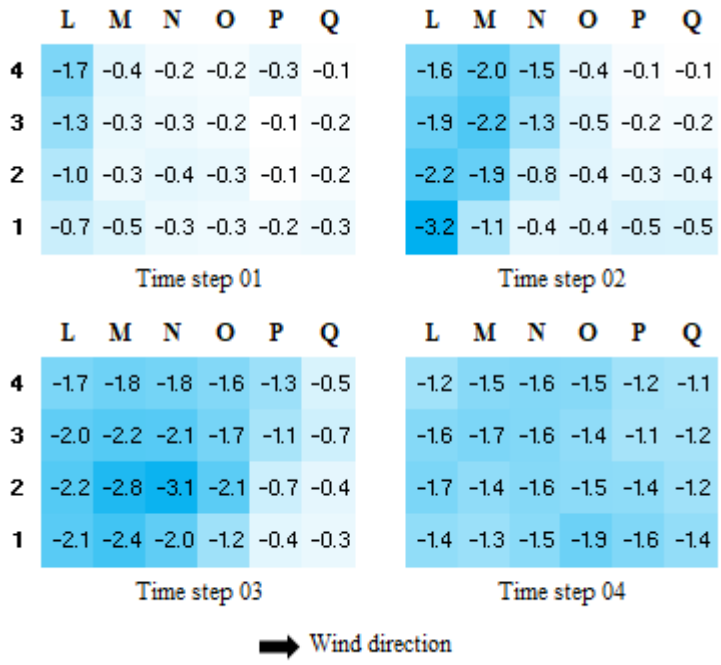


Figure 4.30: Moving peak events on longwall at θ = 270°

The schematic diagram of the above formations are illustrated in following Table 4.3

Table 4.3: Schematic diagram of different vortex formations

| | |
|---|---|
| 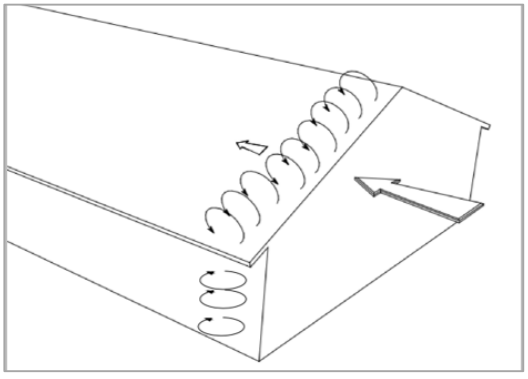 | 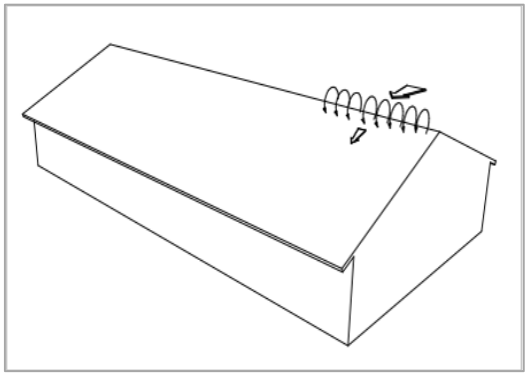 |
| Refer to Figures 4.27 and 4.30 | Refer to Figure 4.26 |

| | |
|---|---|
| 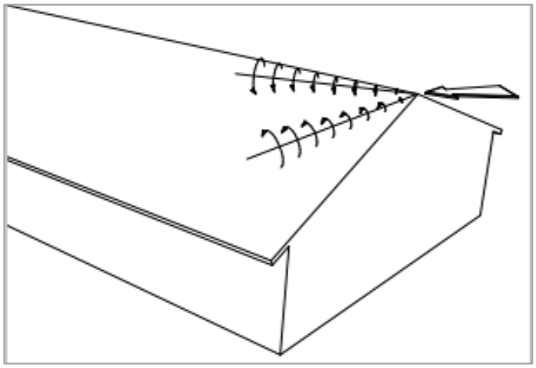 | 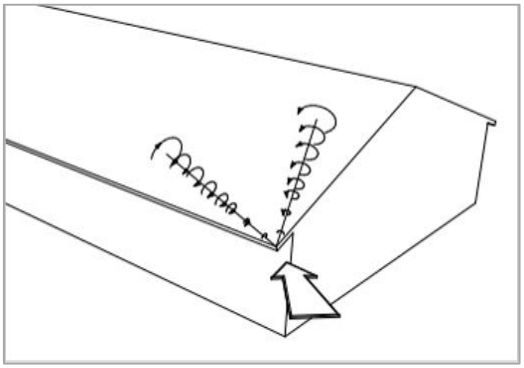 |
| Refer to Figure 4.28 | Refer to Figure 4.29 |

## 4.5 Peak pressure coefficient

Even though time histories provide extreme values, that cannot be sometimes considered as the global peak. Further, the variation of peak events cannot be easily predicted using time histories. The obtained values should be confirmed in an acceptable method as a peak event since the peak events recorded in the time histories can perhaps be noises. Therefore, reliable measures must be taken to extract the maximum or minimum values from the observed events.

Numerous studies were conducted on the peak pressure coefficient related to the low-rise structures (Cook & Mayne, 1979; Dagliesh & Templin, 1980; Davenport, 1964; Gavanski et al., 2016; Holmes & Cochran, 2003; Holmes & Moriarty, 1999; Kasperski, 1997, 2003; Li et al., 2009; Peterka, 1983; Sadek & Simiu, 2002; Sockel, 1980; Stathopoulos, 1979). Though, a significant discrepancy existed among the definition of a peak event and the approaches to estimating the peak values. Gumbel fitting is recognized as the common method of estimating a peak. The Cook and Maynes approach is also a famous and simplified method. Earlier, the standard practice was to obtain a considerable number of repeated time histories to obtain peaks. However, the practical viability of the former approach is extremely difficult. Therefore, the exceptions have been considered to employ single-time history. Following are the methods available to determine peak events.

- Single worst peak
- Peak factor method- Davenport method
- Gust factor approach
- Ensemble average
- Generalized extreme distribution
    - Gumbel method- Type l GEV
    - Type lll GEV
    - Cook and Mayne method – Type I GEV
    - Method of moments
    - Translation method

For the current study, the ensemble-average method will not be applicable due to the number of time histories recorded. Moreover, it does not have a probabilistic base. The peak factor method and gust factor approaches are not used either. The peak factor will only be efficient if the correct peak factor is computed. Gust factor cannot effectively predict the peak pressures along with the directions other than the mean wind direction. Nonetheless, the simple worst peak can be applied to the available set of time histories.

### 4.5.1 Peak pressure coefficient on wind loading standards

Table 4.4 explains how the design standards define their methodology to estimate peak pressure coefficient. Only the ISO, (2009) clearly defines a method of calculating peak coefficient. AS/NZS/1170.2 2011 and AIJ 2004 have provided a guideline in which the recommended methodology is stated (AWES, 1994; BCJ, 2008). No method is suggested in the ASCE 07-16 guideline. Cook and Mayne's approach is employed in the EN 1991-1-4 2005. On the other hand, the peak loads on cladding and components are still estimated using simple worst peaks (Geurts, 2001; Geurts et al., 2013).

Table 4.4: Peak estimation methods in different wind loading standards

| Design standard | Peak estimation method | Possible method | Details of method |
|---|---|---|---|
| AS/NZS 1170.2 2011 | No | Ensemble-average | $t_{pk}$ =10 min – 3 hrs (FS) |
| NBCC | No | Single measured peak | N/A |
| BS-EN 1991-1-4 | No | A single measured peak | N/A |
| ISO, 2009 | 80% fractile of the extreme | N/A | $t_{pk}$ = 10 – 60 min (FS) |
| AIJ, 2004 | No | Ensemble-average | $t_{pk}$ = 10 min (FS) |
| ASCE 07-16 | $C_{p_{max}}=P_{max}/q_{ref}$ | Ensemble-average | $t_{pk}$ =10 min (FS) |

$t_{pk}$ refers to the defined interval for peak pressure coefficient. $C_{pmax}=P_{max}/q_{ref}$ is the maximum instantaneous pressure coefficient observed during the wind tunnel experiment.

### 4.5.2 Estimation of peak pressure

**Generalized extreme values distribution**

Foremost, we employed a single time history to predict the peak pressure values. The period of the peak is equal to 10 minutes in full-scale. The approached methodology is described by Quan et al., (2014) The same approach has now been combined with different methods such as the Gumbel approach and the method of moments. Gaussian distribution was also used for fitting the extreme values of pressure coefficients. However, from the observations, they noticed that the probability distribution of the extremes does not follow symmetric shapes as explained by Gaussian (Holmes, 1985; Massimiliano & Vittorio, 2002). Figure 4.31 witnesses the above statement, indicating the descriptive statistics of randomly selected pressure time histories.

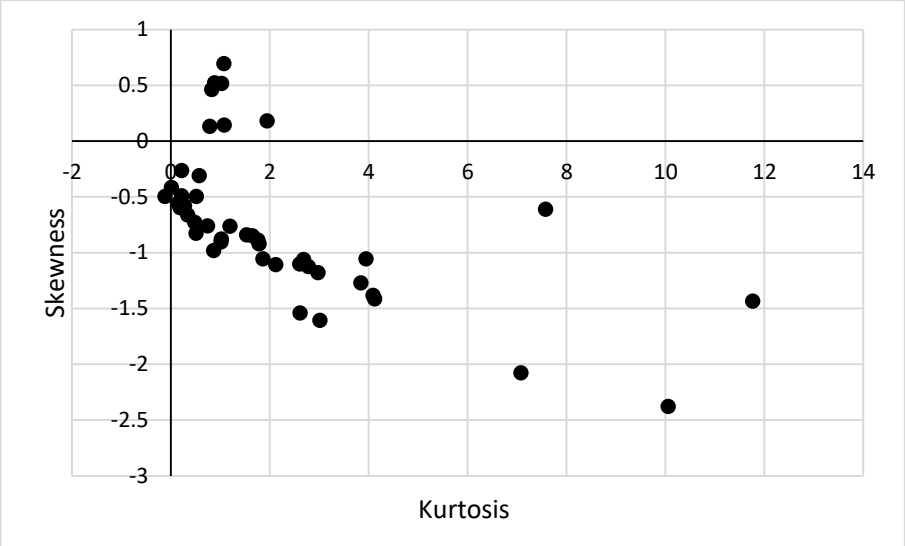


Figure 4.31: Descriptive statistics of random time history samples

Accordingly, the skewness and the kurtosis of some of the time histories significantly deflected from a normal distribution. Therefore, fitting a normal distribution of extreme values will not be a good option. Skewed distributions such as GEV's could perform such tasks effectively. Quan et al., (2014) stated a GEV-associated method for a limited number of time history samples. GEV distribution is characterized by three parameters called, shape ($k$), scale ($\mu$), and location ($\sigma$). Among these, the distribution is divided into several types based on the value of shape (k). This classical approach deals with a large number of independent extreme observations. It considers such peaks will fit one of these distribution types despite the parental probability distribution (Quan et al., 2014). Kasperski, (2003) concludes that the extreme values of wind pressure related to buildings and surfaces usually comply with GEV type I and III distributions. All these three classes can be combined as a single form of the model as follows in Eq.(4.1).

$$F(x_e) = e^{-[\frac{1-k(x_e-\mu)}{\sigma}]^{\frac{1}{k}}} \tag{4.1}$$

If the shape factor (k) is zero, it becomes type I (Gumbel approximation) as follows:

$$F(x_e) = e^{-e^{-[\frac{(x_e-\mu)}{\sigma}]}} \tag{4.2}$$

However, the GEV type I provides moderately over conservative values. Therefore, we estimated the Type I parameters using moment estimators as specified by Tieleman et al., (2007). First, the relationship between the parameters of the distribution and the observed length must be considered. The employed sample time history with a suitable length $t_1$ should be further divided into subsamples with a length of $t_2$. Therefore the relationship between the length of samples can be expressed as $n = t_1/ t_2$, where n is the number of subsamples. The choice of a suitable length $t_2$ should consider the time difference between two consecutive peaks. Therefore, the autocorrelation of the signal must be considered. It will result in the most possible, minimum length of the subset in which the individual peak events can be observed.

Autocorrelation exhibits the correlation between the signal and delayed copy as a function of the lag time. Different sensors at random locations were selected for this purpose. Once the time history was fed into the autocorrelation function, it provides the variation of Auto Correlation Coefficient (ACC) with the lag time. The observed ACC decayed from 1 to 0 within 150-time steps most of the time (equivalent to 6 seconds in full-scale). The resulting ACC's of the A13 sensor is illustrated in Figure 4.32 at $\theta = 270°$.

It shows six seconds interval can be applied as the minimum length of the time interval in which individual peaks have occurred. As well, ACC often reaches zero and gradually increases, leaning toward zero again. Any time interval at which the ACC becomes nearly zero (> 6 seconds) would also be applicable as the length of the sub-sample. However, the precision of the probability plot is dependent on the number of extreme values used. Therefore the sample size with a minimum length is preferred for the peak estimation.

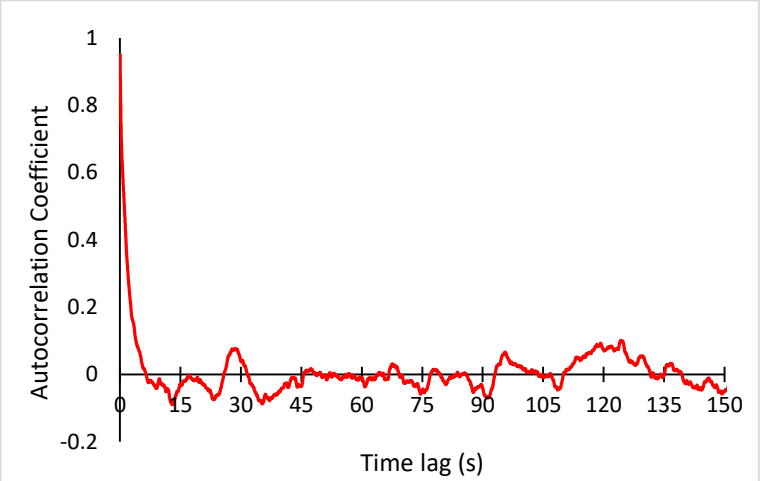


Figure 4.32: ACC of R3 pressure tap of BM at θ = 270°

Subsequently, the extreme values from each sub-sample should be fitted to the extreme value distribution. The type of probability distribution must be considered on the shape factor (Python scripts are provided in Annex 05 and Annex 07). Next, the parameters of the sub-sample should be converted to the parental sample. Finally, the theoretical approximations are present to estimate the upper limit of the extreme values distribution as mentioned below. Subscript 1 and 2 interpret, the parent sample and the subsample, respectively. μ, σ represent the mean and the standard deviation of either the parent sample or the sub-set. ϒ is the Euler number= 0.5772. The extreme value is denoted by $x_e$.

If the shape parameter (k) is non-zero:

$$\sigma_1 = \frac{\sigma_2}{n^k}$$

$$\mu_1 = \mu_2 - [\frac{1 - n^k}{kn^k}]\sigma_2$$

$$x_e = \mu_1 - \sigma_1 \left[\frac{1-\Gamma(k+1)}{k}\right] \quad (4.3)$$

If the shape parameter (k) is zero:

$$\sigma_1 = \sigma_2$$

$$\mu_1 = \mu_2 + \ln(n)\sigma_2$$

$$x_e = \mu_1 + \sigma_1 \Upsilon \tag{4.4}$$

According to Tieleman et al., (2007):

$$\beta = 0.78\sigma_2$$

$$u_2 = \mu_2 - \Upsilon\beta$$

$$u_1 = u_2 + \ln(n)\beta$$

$$x_e = u_1 + \beta\Upsilon \tag{4.5}$$

**Method of moments**

In the usual process of the Gumbel fitting, the reduced variate (Gumbel) was appeared to be biased due to the ranking of extreme values. Therefore, Gringortorn has introduced a reduced variate in which the biasedness is reduced. Alternatively, the method of moments is another popular method of predicting the parameters in an iterative process. Hosking et al., (1985) introduced empirical equations to avoid the iterative procedure. This method was utilized to predict the peak floods, as provided in the (WMO, 1989) report. The same process is utilized here to compute the peak pressure coefficients. However, WMO mentions a unique probabilistic approach based on the moment estimators as follows. The estimated reduced variables may be fitted to Extreme Value I (EV I) or Generalized Extreme Value (GEV) distribution to predict the peak event. The similarities of flood prediction and wind prediction can express the validity of the method of moments. Both predictions do consider a time history. For the wind, the time step selected was 6 s intervals in full scale. The WMO method has been worked out on annual maximum flood. It extracts the peak flood event in consecutive intervals. These moments' estimators give approximations for the Shape (k), scale (u), and location (α). The computed estimators are summarized below in

Table 4.5 for several sensors along their respective critical wind direction. Table 4.6 provides the summary of peak events for selected pressure taps.

Table 4.5: Estimated parameters using GEV and method of moments

| | A8 | | A13 | | B14 | |
|---|---|---|---|---|---|---|
| | GEV | Moments | GEV | Moments | GEV | Moments |
| k | 0.087 | 0.073 | 0.078 | 0.062 | 0.187 | 0.169 |
| α | 0.621 | 0.631 | 1.604 | 1.626 | 1.177 | 1.194 |
| u | 2.463 | 2.452 | 5.297 | 5.270 | 4.504 | 4.483 |

Table 4.6: Estimated peak pressure coefficients under different methods

| Observed worst Peak | GEV III | GEV I | Moments GEV | EV I |
|---|---|---|---|---|
| 5.29 | 5.04 | 5.09 | 4.93 | 5.17 |
| 7.70 | 8.20 | 8.10 | 8.19 | 8.19 |
| 10.11 | 10.63 | 10.47 | 10.51 | 10.63 |
| 12.19 | 12.10 | 12.13 | 11.81 | 12.36 |
| 9.67 | 10.03 | 10.21 | 9.86 | 10.38 |
| 4.83 | 5.20 | 5.55 | 5.28 | 5.67 |
| 6.17 | 6.19 | 6.51 | 6.12 | 6.59 |
| 5.84 | 6.06 | 6.48 | 6.06 | 6.59 |
| 5.91 | 6.07 | 6.64 | 6.09 | 6.75 |
| 12.11 | 11.41 | 11.29 | 11.02 | 11.45 |
| 4.56 | 4.65 | 4.98 | 4.67 | 5.08 |
| 4.13 | 4.22 | 4.51 | 4.15 | 4.58 |
| 6.53 | 6.42 | 6.18 | 6.18 | 6.23 |
| 8.27 | 8.36 | 9.07 | 8.32 | 9.23 |
| 7.26 | 7.25 | 7.30 | 7.23 | 7.37 |
| 7.55 | 7.51 | 8.11 | 7.50 | 8.27 |
| 3.23 | 2.94 | 3.08 | 2.82 | 3.13 |
| 3.19 | 3.18 | 3.21 | 3.09 | 3.28 |
| 7.22 | 6.82 | 6.84 | 6.56 | 6.96 |
| 4.22 | 4.19 | 4.66 | 4.17 | 4.75 |
| 7.13 | 6.51 | 6.49 | 6.13 | 6.49 |
| 3.12 | 3.35 | 3.84 | 3.51 | 3.90 |
| 3.64 | 3.55 | 3.57 | 3.51 | 3.62 |
| 3.17 | 3.11 | 3.11 | 3.03 | 3.14 |
| 2.85 | 2.83 | 2.92 | 2.83 | 2.95 |
| 8.49 | 7.71 | 7.62 | 7.16 | 7.74 |
| 3.33 | 2.46 | 2.49 | 2.60 | 2.45 |
| 3.68 | 2.61 | 2.75 | 2.91 | 2.65 |
| 2.17 | 1.91 | 2.04 | 2.27 | 2.07 |
| 3.74 | 3.23 | 3.04 | 2.94 | 3.02 |
| 1.44 | 1.47 | 1.46 | 1.44 | 1.48 |

Usually, GEV fitting cannot be easily performed manually. Though, the moment estimating can easily be carried out using analytical equations provided by Hosking. However, more than enough computation power exist now to fit these distributions easily using basic programming. There exist a strong correlation among the results obtained from GEV fitting, Moments estimators, and the single worst observations, illustrated in Figures 4.33 and 4.34. For the comparison, single measured peaks were acquired from the BM of the wind tunnel.

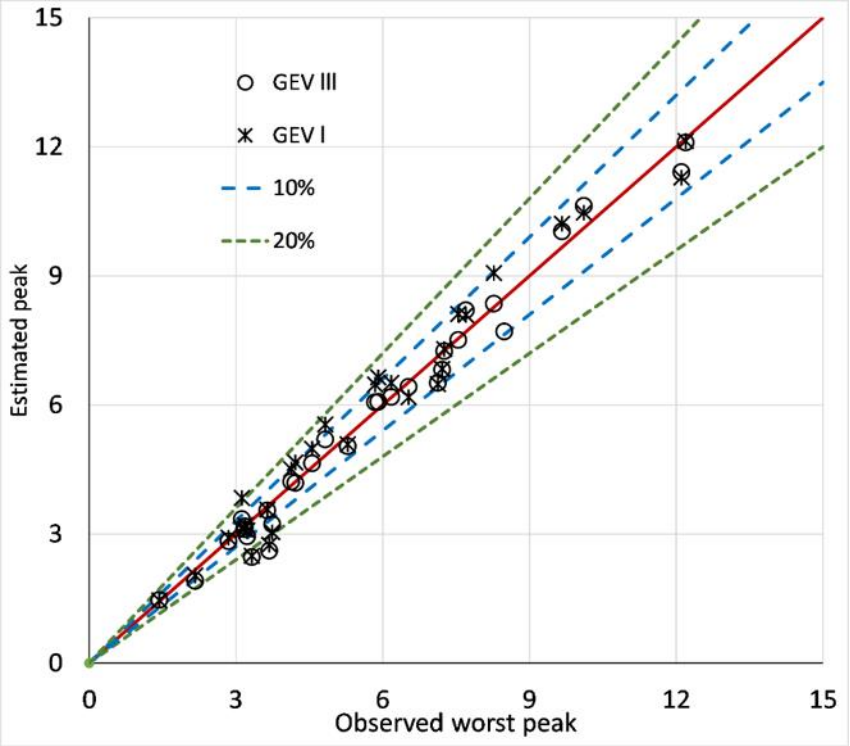


Figure 4.33: Comparison of peak pressure coefficients between GEV method and experimental worst peak

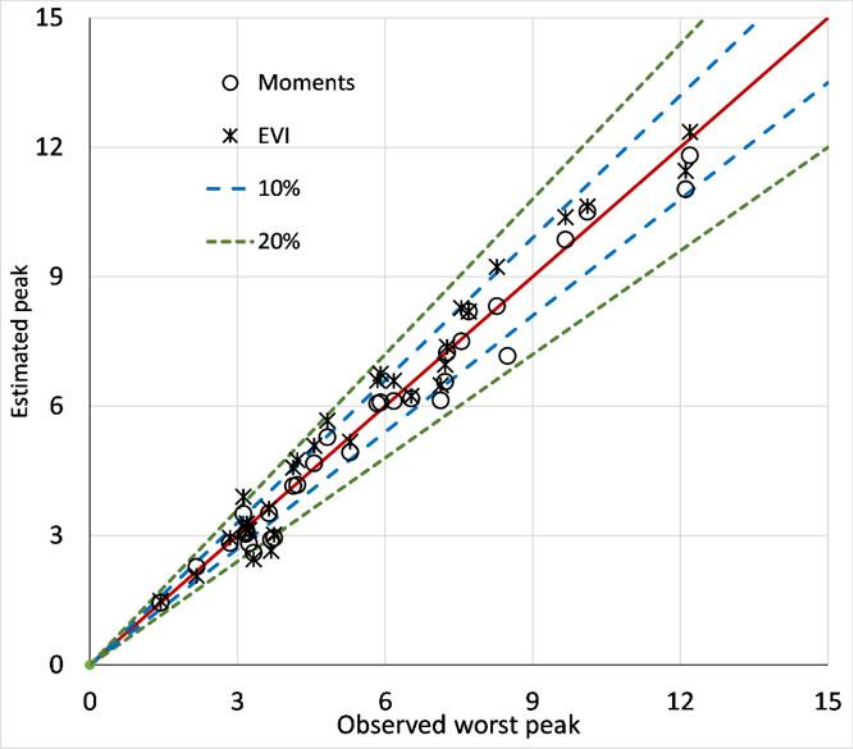


Figure 4.34: Comparison of peak pressure coefficients between moments method and experimental worst peak

It was observed, the methods to estimate peak distribution give a similar range of values retrieved from the wind tunnel experiment. The estimations consist of peak values at various locations on the envelope, including critical locations. However, each model can be explored for its performance under the following indices as stated in Table 4.7. The correlation and the coefficient of determination ($R^2$) are measures of the linearity of the observations. GEV III has obtained the most precision among all the models except for the mean percentage error. Generally, RMSE and SI (Scatter index) indicates how much the observations are likely to deviate from the reference values. The AIC index chooses its best model based on the minimum number. In addition, the methods including GEV I and moment estimators can also perform satisfactorily in the sense of a limited number of time histories. However, the Cook any Mayne methods seem to be slightly over-conservative over the observed peaks. The mean percentage error has gone up to 14%, a reasonably higher compared to other fair explanations.

Table 4.7: Model performance indices

| | GEV III | GEV I | Moments | EV I | Cook and Mayne |
|---|---|---|---|---|---|
| $R^2$ | 0.991 | 0.983 | 0.986 | 0.981 | 0.986 |
| Correlation | 0.996 | 0.992 | 0.994 | 0.992 | 0.994 |
| ME% | -2.839 | 0.241 | -3.396 | 1.509 | 14.721 |
| MAE | 0.285 | 0.432 | 0.356 | 0.472 | 0.945 |
| RMSE | 0.400 | 0.521 | 0.496 | 0.567 | 1.111 |
| SI | 0.060 | 0.081 | 0.072 | 0.087 | 0.107 |
| AIC | -18.645 | -11.568 | -12.867 | -9.267 | 8.841 |

## 4.6 Analysis of peak pressure

The analysis of ($\widetilde{C_P}$ and $\widehat{C_P}$ )would not be exactly similar to the $\overline{C_P}$ analysis. All the wind directions were considered for the peak analysis due to the unpredictability of the observations. However, the ($\widetilde{C_P}$ and $\widehat{C_P}$ ) analysis was based on the $\overline{C_P}$ analysis. Assuming the simultaneous nature of peak pressure coefficients, design guidelines suggest a method to obtain a peak as a function of the tributary area. It is noteworthy, some of the design standards specify the peak pressure coefficient as the product of the mean pressure coefficient and gust effect factor.

The intention is to determine the effect of boundary walls on the peak pressure coefficient. Usual sign convention will be employed in the peak analysis as well. Attention should be paid when the graphs are referred to since the vertical axis contain $-C_p$ values at the locations where generally the negative pressure values dominate. Moreover, considering the correlation obtained before, we will consider the single worst peak for the analysis purpose. The locations selected for the analysis are bolded in Figure 4.35.

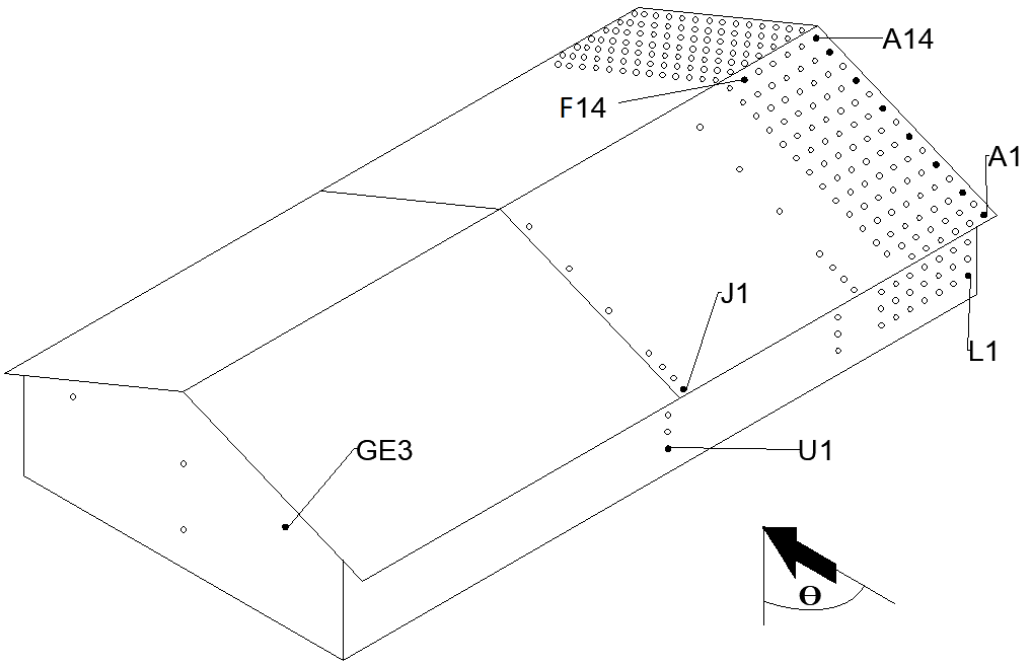


Figure 4.35: Selected pressure taps (bolded) for the analysis of ($\widetilde{C_P}$ and $\widehat{C_P}$ )

### 4.6.1 Peak pressure coefficient of the roof

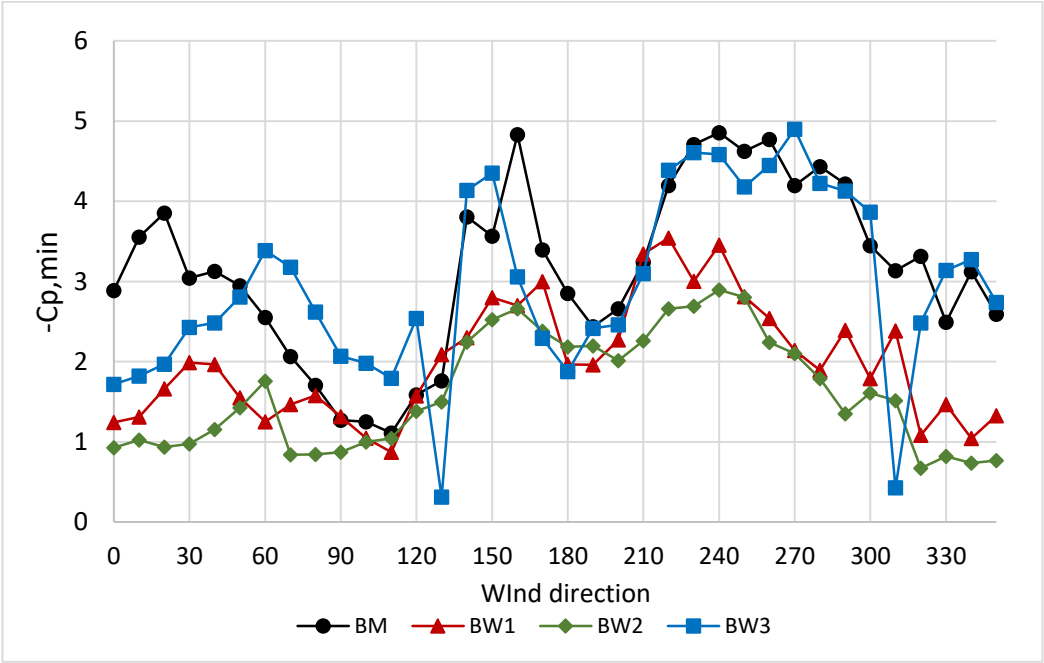


Figure 4.36: Directional variation of $\widetilde{C_P}$ of A1 pressure tap

A1 pressure tap was located as the corner most tap of the leading edge. The mean pressure of the corner indicated the critical direction are the wind azimuths from 210 to 270 and a similar pattern can be observed in the peak pressures. Further, the wind azimuth of 150 has influenced a sudden peak at the corner. Among the critical directions, the peak pressure coefficient will be varying from -3 to -5 as seen in Figure 4.36. Unlike in the mean pressure variation, even when the pressure tap is located on the trailing edge concerning the direction of wind attack, considerable peak events might occur. For the control model, the entire variation of peak pressure coefficient lies between -1 to -5. It is significant to see that BW1and BW2 have been effective to reduce the peak pressure similar to what we observe from the mean pressure analogy. BW3 nearly mimics the variation of the base model except at few locations. This again reminds the importance of keeping a sufficient distance between the house and the boundary to force early separation. BW2 displays a continuous reduction in peak suction compared to other patterns. It should be notified even if the upper extremities of the peaks are reduced, lower extremities remain in the same range as negative values. During the $\overline{C_P}$ comparison, the values came to an even positive side due to the effect of boundary walls. As well the corner most tap A1 had the critical mean values compared to the pressure taps along the leading edge. Next, we will discover the effect of the boundary wall on the pressure tap J1 located on the leading edge of the middle frame. Figure 4.37 shows the variation of peak pressure of pressure tap J1 along various wind azimuths.

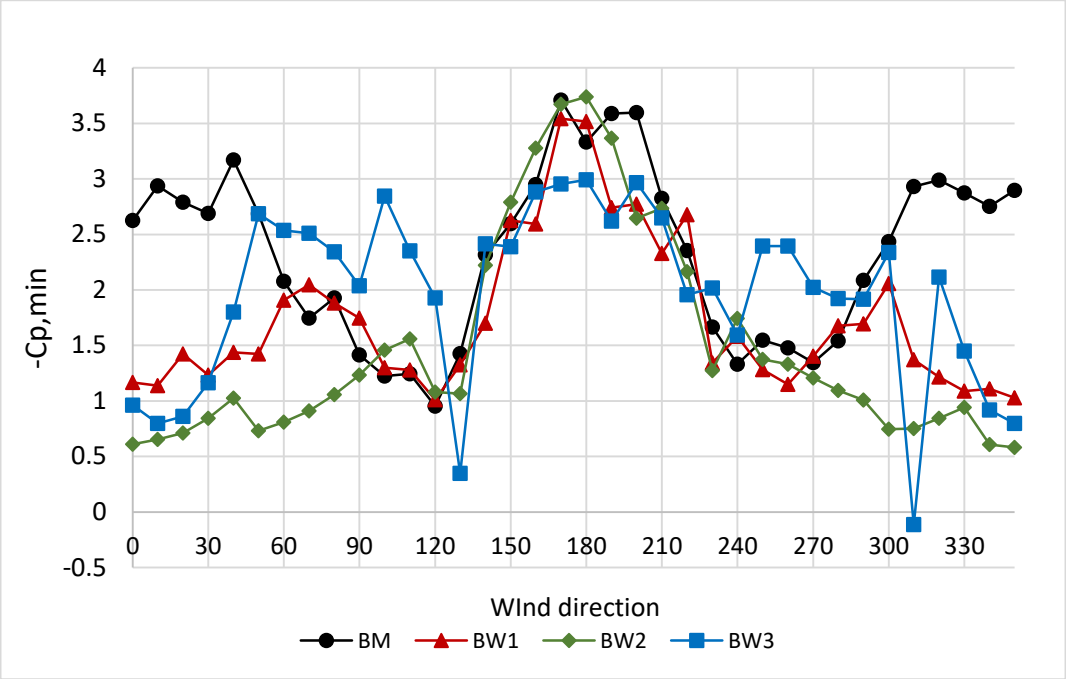


Figure 4.37: Directional variation of $\widetilde{C_P}$ of J1 pressure tap

According to Figure 4.37, the intensity of the suction has slightly reduced when the position of the middle frame along the leading edge is considered. The maximum suction of the base model is below -3.6 and the variation at the corner taps has been changed drastically. Even if BW1 and BW2 could exhibit a favorable reduction in most wind directions, a slight increment has been obtained particularly between the wind azimuths $\theta$ =150°, and $\theta$ =180°. For the critical directions, this pressure tap was located near the downstream wake of the building. These critical values have been effectively decreased when BW3 is present. Also, BW3 holds some abrupt changes in the peak pressure and the maximum peak corresponds to BW3 is below -3. Nevertheless, some values can be seen in several directions that have exceeded the peaks of the base model. The nature of the fluctuation indicates the effect of all boundary walls is significant especially for the along wind attacks. The maximum peaks occurring on zero wind azimuth have reduced up to -1.16, -0.96, and -0.6 for BW1, BW3, and BW2, respectively. From figures 4.36 and 4.37, it is observed that even the critical direction might change along the pressure taps on the leading edge. It might be noted that the abrupt changes in BW3 have caused suction to be eased and even going for slightly positive values. This highlighted the importance of boundary

walls whereas previous studies had observed relatively larger suctions at the eave level. The boundary walls could acquire a fair reduction in adverse events. The peak coefficients along the leading edge (A1 to J1) were sufficiently correlated when the wind azimuth is between $\theta = 0°$ and $\theta = 150°$. Then a disrupted transition in the peak events can be seen which was witnessed by Figures 4.36 and 4.37 above.

Figure 4.38 depicts the C, peak variation on the gable edge pressure taps (A1-A14). Visual correlation between the results can be observed for the wind azimuths between $\theta = 0°$ to $\theta = 180°$, and $\theta = 270°$ to $\theta = 360°$. When the wind angle is between 0° and 90°, the cornering effect is dominating as seen according to the A1 pressure tap. Next, the effect is slowly transferred to the apex of the gable end. These peaks will indeed be the results of intermittent vortex formation and turbulent fluctuations as we observed in the mean pressure comparison. A13 location seems to be the most critical of the entire roof. The maximum negative pressure exerted on that particular tap is higher than the critical suction exert at the corner of most taps. For the most critical location, the corresponding wind azimuth was found to be 220. Next, we will isolate the critical pressure tap and another tap in between the A1 and A14 to distinguish the effect of boundary walls on the peak distribution as shown in Figures 4.38.

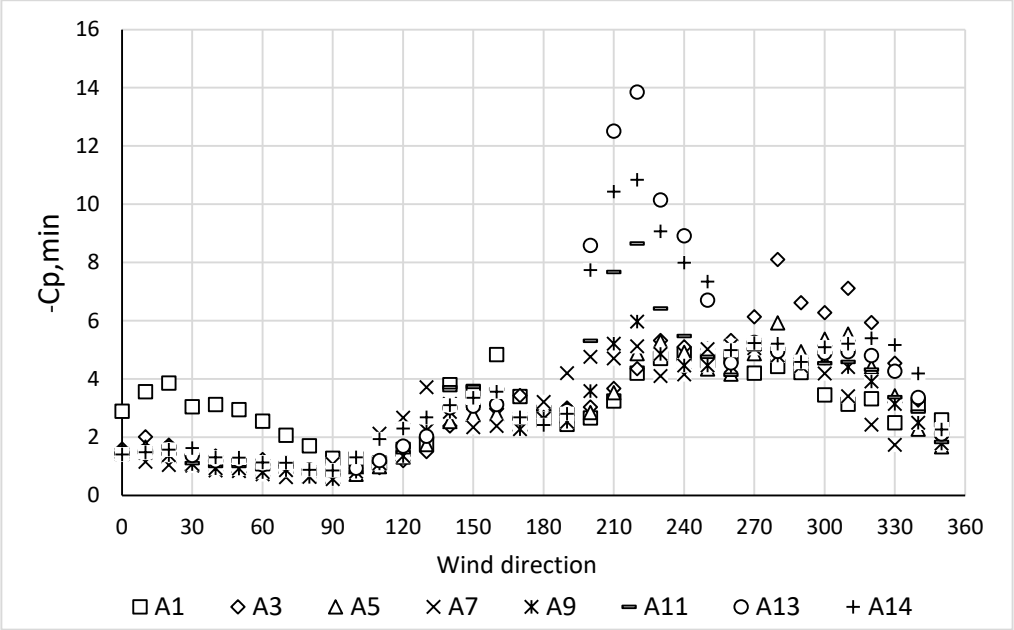


Figure 4.38: Directional variation of $\widetilde{C_P}$ of along the gable end pressure taps

Along the leading edge, a good variation between the results was observed in the presence of boundary walls. The correlation coefficients were below 0.6 and it indicates a substantial effect is present. However, according to Figures 4.40 and 4.41, a good correlation between the control model and boundary walls can be observed. A8 tap and A13 taps represent the middle of the selected tap line from (A1-A14) and near to the apex, respectively. The peaks occurring along most directions are well correlated, meaning that the effect of boundary walls would have been less significant as we discussed in the mean pressure analogy, towards the apex. Therefore, would further relate this by considering the $C_{P\sigma}$ at those locations considering critical directions.

As expected, the $C_{P\sigma}$ represents the most reasonable judgment on the peak pressure variation. In Figure 4.39, $C_{P\sigma}$ value near the apex of the gable end (A14) is shown for the 220 wind azimuth (Blue colour represents higher $C_{P\sigma}$). Thereby, high RMS values are directly associated with large turbulence fluctuations. Therefore, the mean and the peaks occurring in this zone will be critically affected. Rapid fluctuations are more often and the vortex formation might be more disrupted than the corner regions as predicted in the mean analogy.

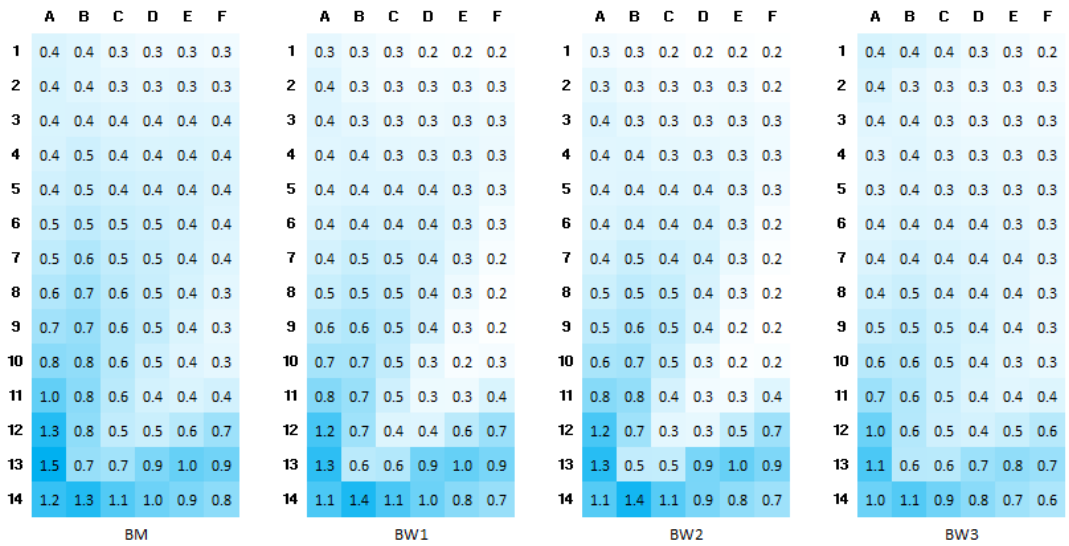


Figure 4.39: Spatial variation of $C_{P\sigma}$ near the apex of gable end at θ=220°

In particular, the critical values show a less significant dependence on the boundary wall patterns. Values obtained for the boundary wall pattern indicate that the fluctuation coefficient tends to reduce and the intensity of the fluctuated zone is reduced. The less significance can be attributed to the high correlation values among the boundary walls and control model. Further, the roof pitch would have a significant impact on these turbulent fluctuations although it was not experimentally proved in this study.

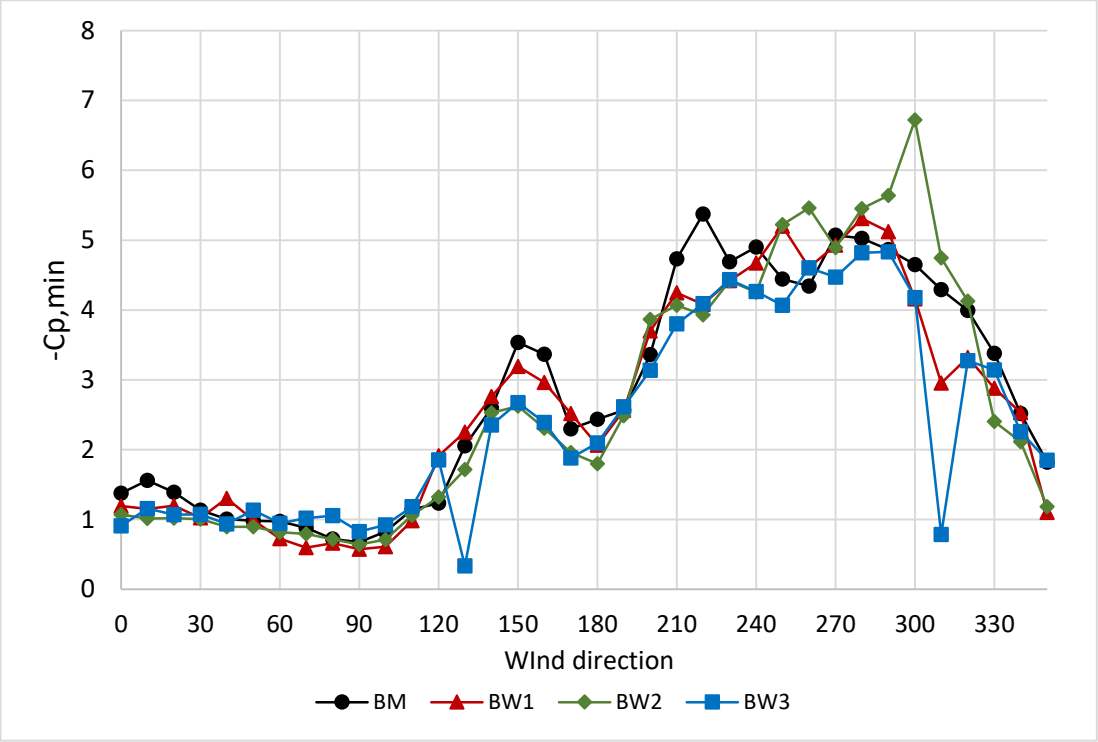


Figure 4.40: Directional variation of $\widetilde{C_P}$ of A8 pressure tap

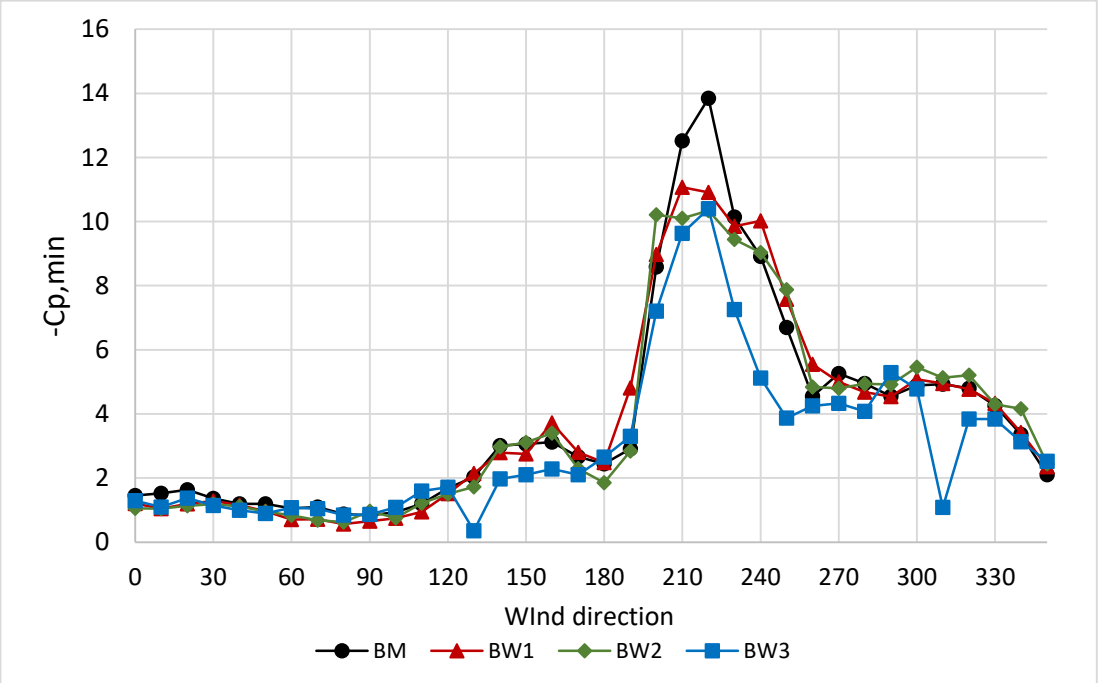


Figure 4.41: Directional variation of $\widetilde{C_P}$ of A13 pressure tap

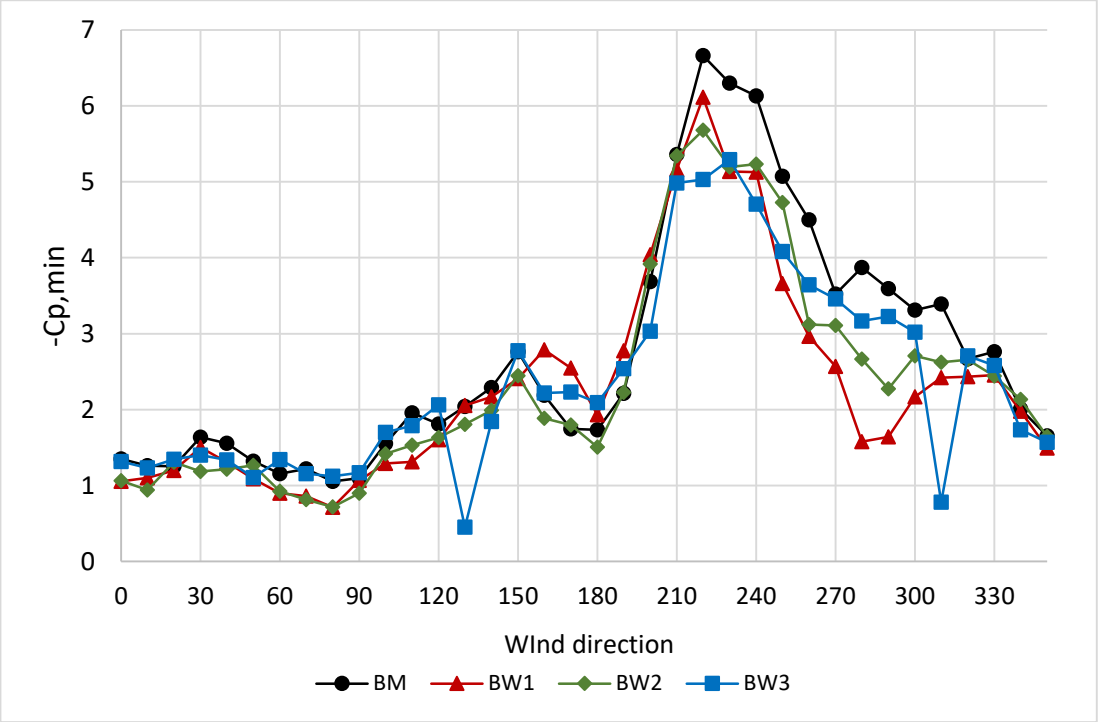


Figure 4.42: Directional variation of $\widetilde{C_P}$ of F14 pressure tap

The peak suction recorded in the A1 tap was around -4.8 and it reduces towards a certain distance and gradually leads to more disrupt peaks. The middle tap A8 had a peak recorded as -5.37 in the base model and towards A13, peak suction becomes -13.8. Pressure tap F14 exerted a peak event of -6.65. From these magnitudes, it can be emphasized that the corner extreme suctions and apex extreme values are not occurring simultaneously and the apex suction is more critical which had been less affected by the boundary walls. Then, towards the interior zones of the ridgeline, the extreme value is getting reduced approximately by 50% and the critical direction along the ridgeline remains the same. The effect of BW3 is seen as the most effective among all the patterns along the ridgeline for wind azimuth 220°. Approximately, the reduction of 25% from the initial peak could have resulted from BW3. It should be notified that the extreme values are more often for the directions closer to the crosswind direction.

### 4.6.2 Peak pressure coefficient on walls

Unlike in the roof structure, peaks on the walls could be considered as negative or positive values. Generally, the critical negative peaks dominate on the roof, as is seen from the experimental results. During the experiment, more negative values had been recorded towards the vertical edges of long walls. The peaks occurring on such locations confirm this above statement as shown in Figures 4.43 and 4.44. For wind azimuth 290°, the edge of the longwall (L1) has exerted -3.47 of peak suction and the middle of the wall (U1) has experienced -1.38 along wind azimuth 210, which is 60% less than the value at the edge.

When there are boundary walls, a clear reduction in the negative peaks is observed in both L1 and U1 taps despite few exceptions. BW3 has influenced disordered behavior in the negative peak of L1 taps. Both the intensity and the direction of the critical values have changed. However, a part of the directional variation (L1) of all boundary walls still can be seen to have fairly correlated with the base model. Such a correlation could not be observed in the U1 pressure tap. Overall, the negative peaks at L1 have been effectively reduced due to BW1 and BW2. The former peak of -3.47 has now reduced up to -2.33 and -2, corresponding to BW1 and BW2.

Similarly, BW1 and BW2 have contributed to reduced negative peaks occurring on location U1 which represents the middle of the long wall of the base model. However, the wind azimuths from 270° to 90° in the clockwise direction, indicates the peaks have been increased in contrast to the BM. Moreover, the increase is highest in BW1. The visual correlation observed in the L1 tap was not present with the values obtained for the U1 pressure tap. As observed in the mean pressure variation, the symmetric nature of the peak fluctuations is still can be viewed in Figure 4.44.

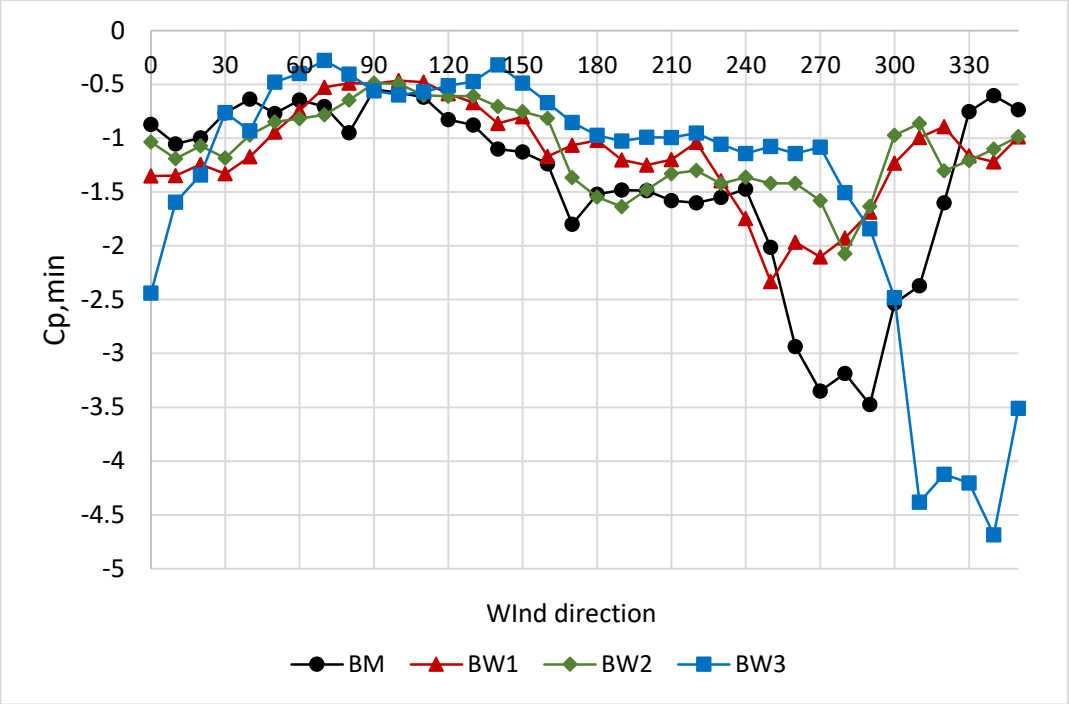


Figure 4.43: Directional variation of $\widetilde{C_P}$ of L1 pressure tap

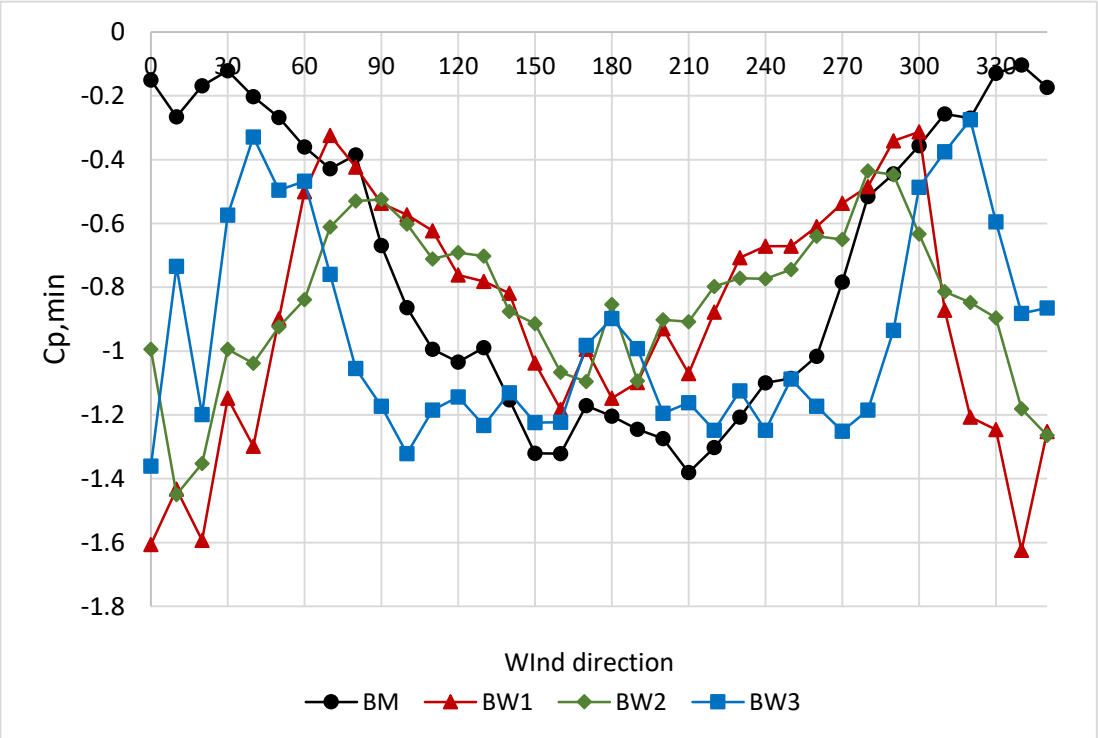


Figure 4.44: Directional variation of $\widetilde{C_P}$ of U1 pressure tap

Afterward, the maximum pressure on the aforementioned locations is illustrated in Figures 4.45 and 4.46. A good correlation between boundary wall patterns with the BM can be observed except for BW3 along several wind azimuths. For the edge of the sidewall, it seems that the maximum pressure has been slightly increased and BW3 shows abnormal discrepancies between the 0° and 180° wind azimuths. The maximum pressure coefficient has reached 3 within those directions. However, between the wind azimuths of 300° to 0° in the clockwise direction, a reduction in the maximum pressure can be obtained for BW2 and BW3.

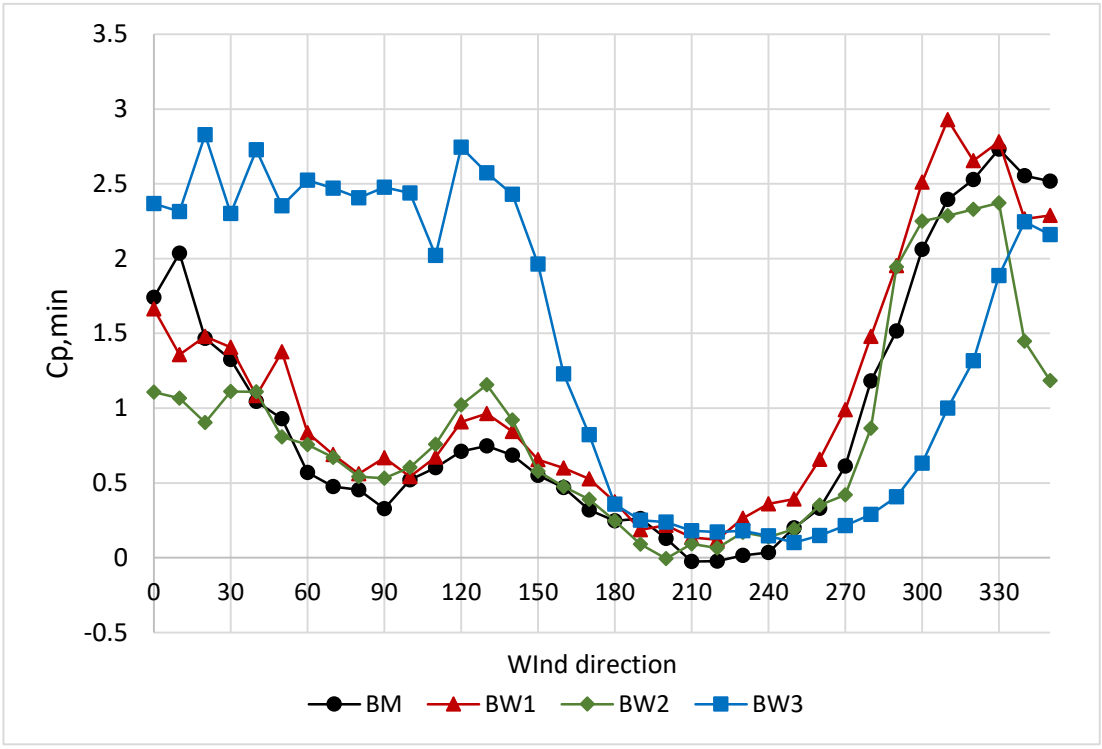


Figure 4.45: Directional variation of $\widehat{C_P}$ of L1 pressure tap

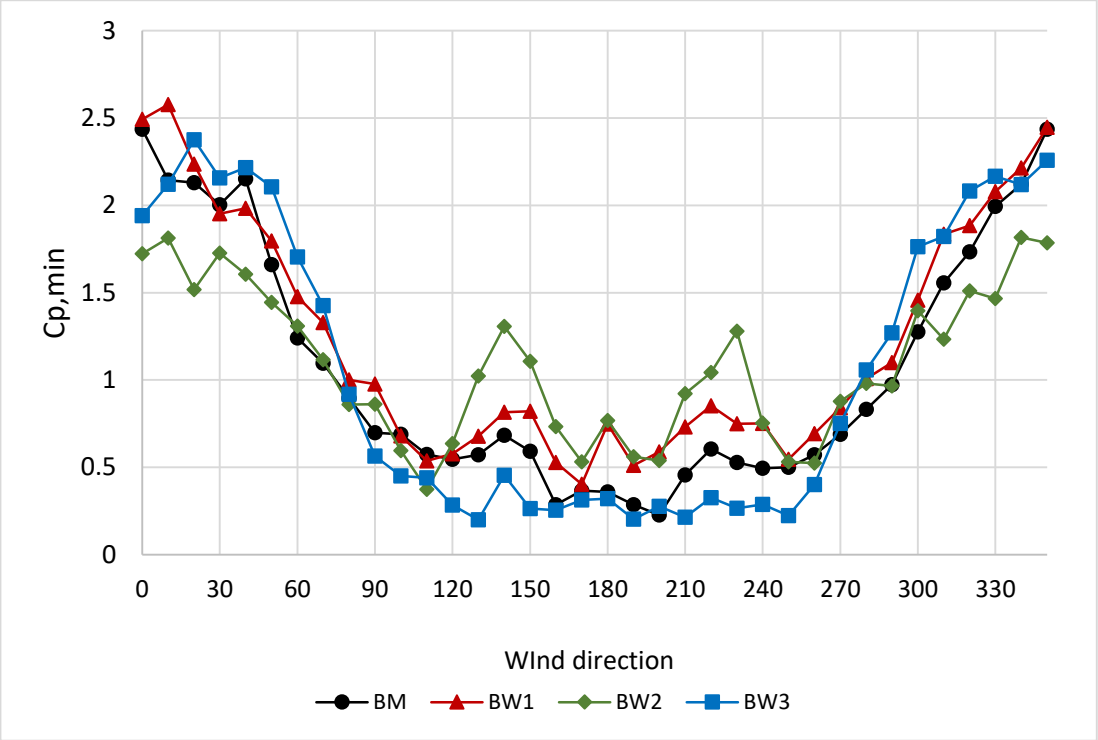


Figure 4.46 Directional variation of $\widehat{C_P}$ of U1 pressure tap

Figures 4.47 and 4.48 display the variation of peak pressure coefficients in the corner of the gable wall (Pressure tap GE3). This tap was specially selected from the gable wall taps since corner regions can accommodate steep pressure gradients and turbulence characteristics. For the zero wind azimuth, the selected tap will be located near the leading edge of the gable wall (Sidewall). Therefore, the intensity of separation and intermittent vortices could be critical in this zone. Figure 4.47 witnesses this statement by displaying relatively larger peaks along with such directions. However, the remaining directions will not be critical, concerning the zero wind azimuth. Another set of secondary extreme values can be observed when the same pressure tap is near the trailing edge of the sidewall, for the 180 wind azimuth.

However, it shall be notified, the intensity of extreme values reduces when the boundary walls are located. The maximum reduction in the critical peaks is observed in BW3. According to the observations, BW2 could reduce 50% of the initial critical values. The secondary peaks between the wind azimuths of 180° and 210° seem to be reduced due to the boundary walls.

Maximum pressure coefficients have indicated critical values for the direct wind approaches normal to the surface. The maximum value obtained is 3.48 for the base model. Nevertheless, the maximum pressure coefficients exhibit less significance in all four cases including the BM. From Figure 4.48, a strong correlation between the results could be observed.

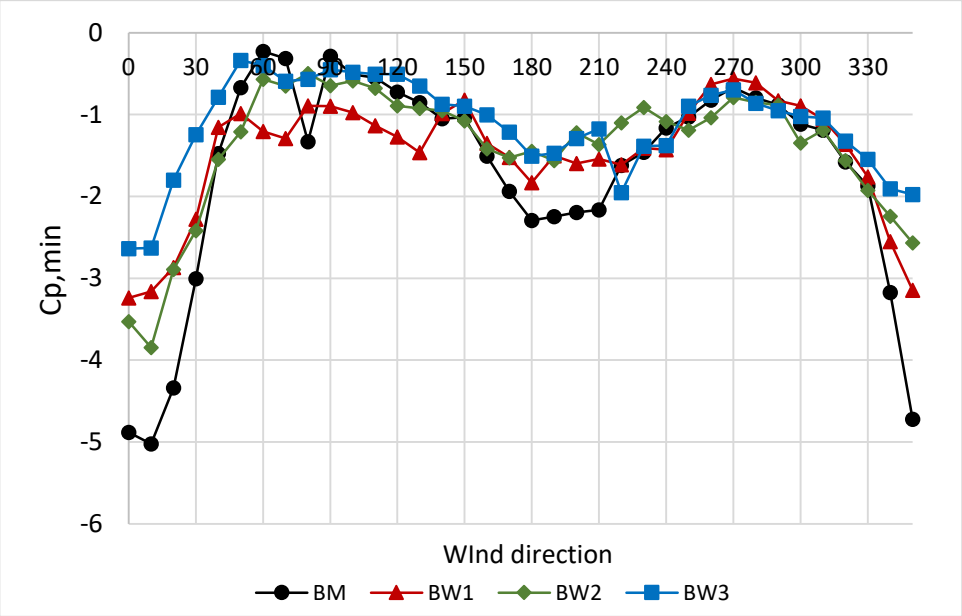


Figure 4.47 Directional variation of $\widetilde{C_P}$ of L1 pressure tap

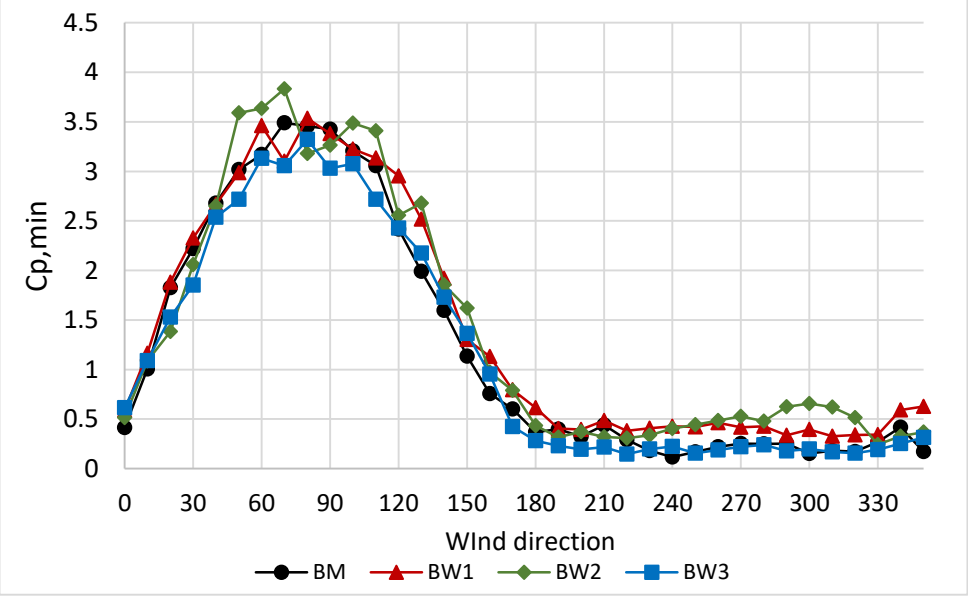


Figure 4.48 Directional variation of $\widehat{C_P}$ of GE3 pressure tap

### 4.7 Summary of analysis on mean and peak coefficients

A significant influence from the boundary walls was observed during mean and peak analysis whereas the summary is presented in Table 4.8 and 4.9.

Table 4.8: Summary of $\bar{C}_p$ analysis compared to BM

| | $\bar{C}_p$ | | |
|---|---|---|---|
| Location | BW1 | BW2 | BW3 |
| Leading edge (Middle) | Effective for the windward slope, Less effect on the downwind slope | | |
| Leading edge(Corner) | Positive pressure dominates | | Similar to BM |
| Ridgeline (Gable end) | Maximum reduction 18% | Maximum reduction 14% | Maximum reduction 25% |
| Ridgeline (Interior) | Less effect <5% | | Maximum reduction 28% |
| Gable wall corners | Overall the positive pressure and suction reduced | | |
| Longwall corners | | | |

Table 4.9: Summary of ($\widetilde{C_p}$ and $\widehat{C_p}$) analysis compared to BM

| | ($\widetilde{C_p}$ and $\widehat{C_p}$) | | |
|---|---|---|---|
| Location | BW1 | BW2 | BW3 |
| Leading-edge (Middle) | Peaks reduced, (Worst peaks less dependent) | Peaks reduced, (Worst peaks less dependent) | Peaks reduced, Worst peak reduction 22% |
| Leading-edge(Corner) | Peaks reduced, Worst peak reduction 27% | Peaks reduced, Worst peak reduction 42% | Similar to BM, Disrupted |
| Ridgeline (Gable-end) | More correlated, Less effect, Worst peak reduction 29% | More correlated, Less effect, Worst peak reduction 29% | More correlated, Less effect, Worst peak reduction 29% |
| Ridgeline (Interior) | Strongly correlated, Less effect, Worst peak reduction 7% | Strongly correlated, Less effect, Worst peak reduction 7% | Strongly correlated, Less effect, Worst peak reduction 18% |
| Gable wall corners | Suction reduces slightly | | Good correlation |
| Longwall corners | Negative pressure decreases and a good correlation exists | | worst suction and pressure occur and a good correlation exists at the middle |

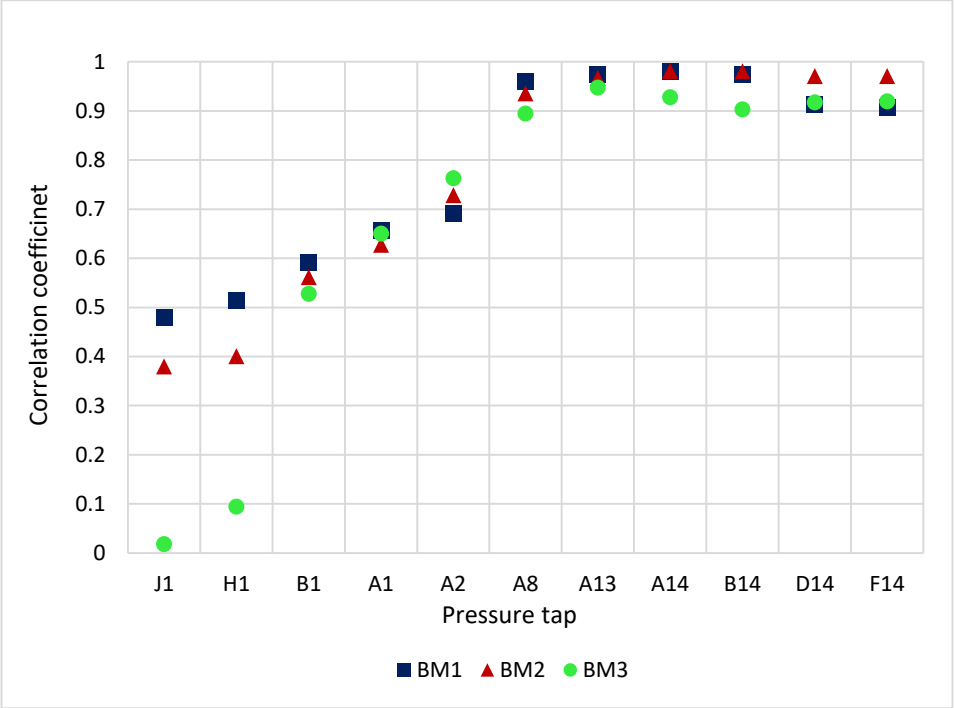


Figure 4.49: Comparison of correlation between the BM and boundary wall patterns

Figure 4.49 displays the correlation of each boundary wall pattern with the BM. Thus, it is convinced that near to the middle of the leading edge, the effect of the boundary walls on peak pressure coefficients is significant. Further, there is a notable difference between each boundary wall. However, towards the corner of the roof and apex of the gable end, the effect of boundary walls on peak pressure coefficients appeared to be less pronounced. In addition, the correlation between the boundary walls has increased, leading to less effect from the different lateral and upstream separation distances.

## 4.8 Synchrony of extreme events

Parackal (2018) has emphasized the progressive failures are more often associated with the correlation of loads occurring on surrounding connections. If the failure initiates at a particular location, adjacent connections are more prone to be subjected to load redistribution, leading to catastrophic events. Therefore, such progressive or cascading failure might depend heavily on the correlation of neighboring locations. Some of the zones might heavily under pressure while other zones are not. Synchrony

of peak events exhibits the measure of time lags of each peak so that averaging peak events over a larger area will not be practical. In this section, we will be addressing the simultaneous nature of peak events and the effect of the boundary walls.

### 4.8.1 Cross-correlation of time histories

Eq. (4.6) defines the cross-correlation coefficient ($r_{ij}$) between each time history. It is a function of the lag time ($\tau$) of a particular signal in contrast to another signal. $p^{'}$ refers to the fluctuation component of the pressure while subscript i and j denote two respective locations. 'T' is the time in which is the signal is analyzed and 't' is the time increment. 'σ' refers to the standard deviation of pressure.

$$r_{ij}(\tau) = \frac{1}{T.\sigma_{pj}.\sigma_{pi}} \int_0^T p_i'.\, p_j'(t+\tau)dt \tag{4.6}$$

Pressure at a particular location, usually correlates with the critical location, indicating small lag or lead times. It explains the pressure fluctuations approach a particular location slightly after or before the critical connection experience the fluctuations. Therefore, the averaging of peak pressure should be well considered since the lag or lead time may possess a considerable time lag when the full envelope is considered. It can be graphically represented as follows in Figure 4.50.

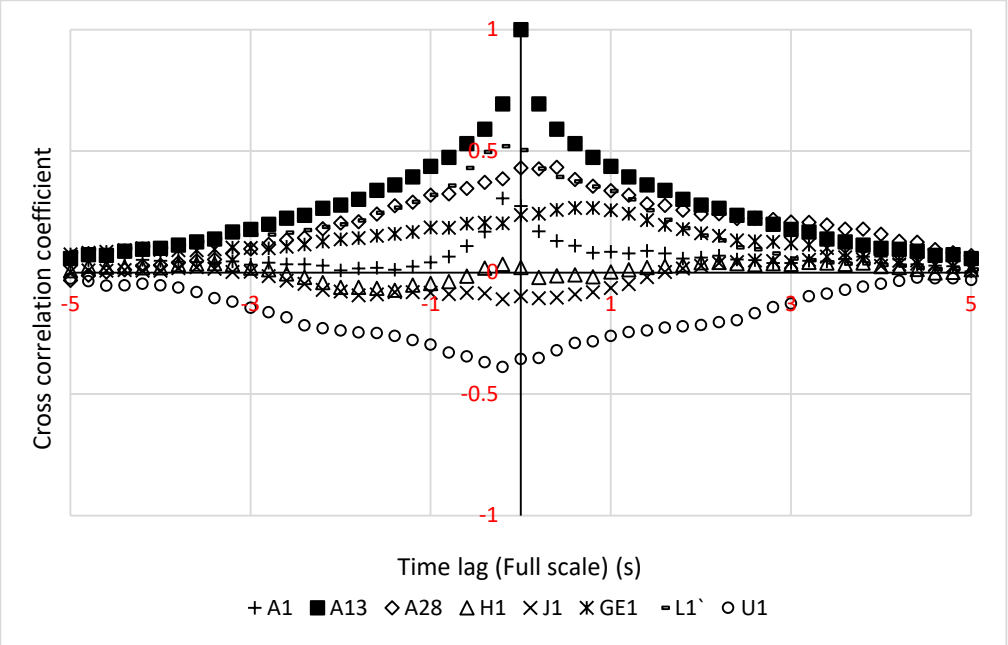


Figure 4.50: Cross-correlation coefficient

Accordingly, the cross-correlations values can be expressed relative to the critical pressure tap A13. Thus, it seems the peaks of the roofs at several locations (A1 and A28) have almost zero lags which means the peaks at these 3 locations will arrive at the almost same time. However, the correlations coefficient values are less below 0.5. If the H1 pressure tap is considered, the cross-correlation coefficient shows uniform variations, indicating the peaks will not be critical compared to the A13 location. In particular, pressure tap GE1 shows a 1 seconds lag time of the peak along this critical direction. In addition, pressure tap J1 exhibits a negative correlation value that explains an occurrence of positive peak values. The same happens with the pressure tap (U1) on the long wall surface.

Further, we will move to the critical region to identify the behavior of peak events and their mutual correlation with respect to the most critical locations. For that purpose, nine pressure taps have been chosen. Figure 4.51 shows the correlation values and corresponding time lag of peak, obtained for each wall pattern including the control model. (Blue colour indicates the higher values while the lower values are noted in white colour)

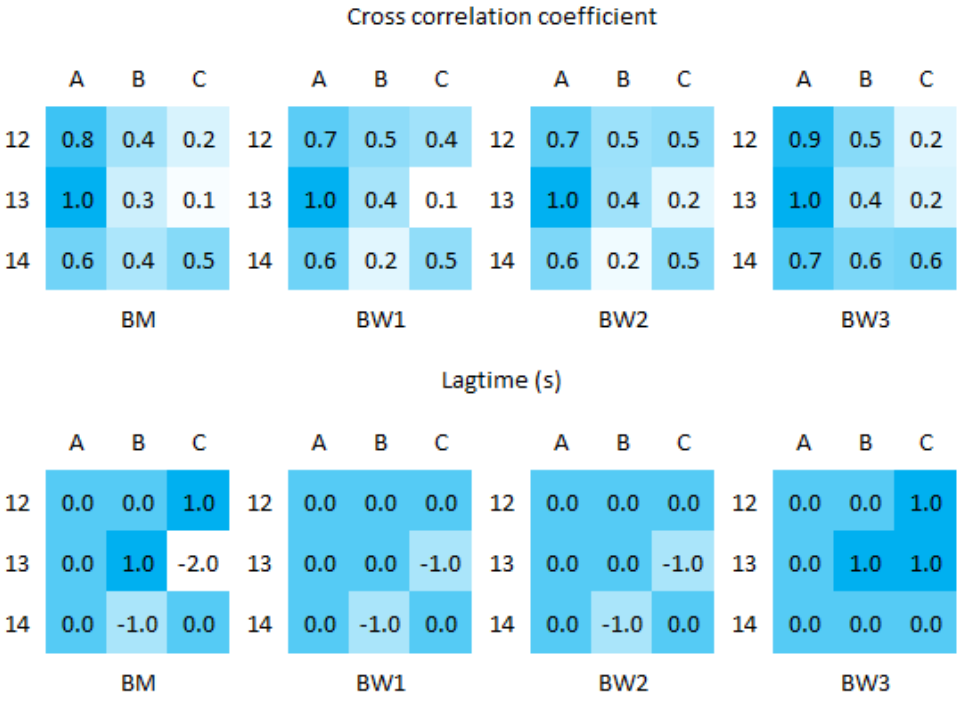


Figure 4.51: Cross-correlation values and corresponding lag time (s)

Thus, it implies the synchrony of the peaks has increased by comparing the base model. The lead time of 2 seconds has now been altered by a lag of 1 s. As well, the peaks have been slightly more correlated which is justified by the cross-correlation coefficients. Therefore, it can be stated, apart from the magnitude of the peak events, the correlation and the synchrony of peak events occurring on neighboring locations, are altered due to the presence of boundary walls.

## 4.9 Summary of the Chapter

In this chapter, the code comparison, mean pressure coefficient analysis, peak pressure estimation, the analysis on peak pressure coefficient, and the synchrony of peak events have been discussed. The mean analysis could emphasize the values exerted on the isolated envelope could be brought down by having a boundary wall. Moreover, the peak events were individually identified as the intermittent vortex and eddy formations. Such peak events move across the surface by distributing peaks over adjacent locations. Unlike in the mean pressure coefficients, peak pressure coefficients exhibited a substantial correlation along the respective directions even in the presence of boundary walls. Nevertheless, the peak values at critical locations have been reduced in terms of wall patterns. Further, the synchrony of peak events has been altered with respect to the isolated conditions. Still, the available time history data have shown the generalized extreme value distributions and the method of moments can be effectively used for the peak pressure estimations.

# 5. CFD MODELLING

## 5.1 Overview

Time, cost, and significant expertise are common constraints, identified during either wind tunnel or full-scale testing. Such constraints can be avoided moderately by shifting into analytical simulations. Thus, CFD provides a strong phase to perform a wide variety of simulations inside a processing unit. As describes in chapter 2, the accuracy of CFD models shown to be improving with time and computational power. Even, the complex environmental conditions and the aerodynamic effects can be evaluated using CFD techniques. The main reason behind adhering to CFD tools is to perform a parametric study from which the experimental observations can be further confirmed. Foremost, the wind tunnel conditions should be properly calibrated inside the CFD model, using the wind tunnel conditions.

Flow simulations were carried out using commercially available software, ANSYS Fluent. The geometry and the mesh were created using ANSYS Gambit 2.4.6. Numerical simulations were performed at $\theta = 0°$ and $\theta = 90°$. The standard k-ε turbulence model was chosen for the analysis. The input velocity profile is not uniform in the boundary layer wind tunnel. Therefore, the velocity profile and turbulent kinetic energy profile should be separated complied and fed into the fluent system (Refer Annex 06).

## 5.2 Computational Domain

The region which needs to be simulated determines the size of the fluid domain. It should have sufficient downstream fetch to avoid abnormal pressure fields and reverse flow conditions. The blockage ratio was maintained below 3% to prevent flow from being accelerated. The upstream fetch between the inlet and the model should be modeled with the appropriate roughness length. Further, the length of upstream fetch has been suggested as 5H while the downstream fetch is preferred to be 15H (H- is the height of the building). For the current study, H was selected as the largest dimension corresponding to the model. To demonstrate the grown boundary layer, the height of

the domain was selected as 6H in this case. It should be noted, an unnecessarily larger domain will result in more computation burden. Figure 5.1 shows the dimensions of the computational domain which we selected.

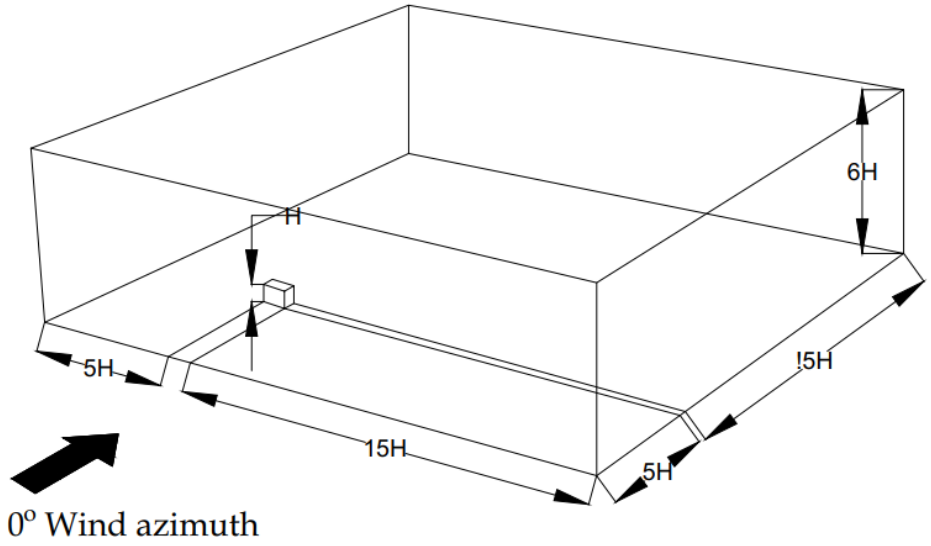


Figure 5.1: Dimensions for the computational domain

### 5.3 Meshing

In analytical simulations, the quality of the mesh affects the accuracy of the solutions. As specified in chapter 02, the mesh is the most important aspect of the CFD modelling sequence. Finer mesh can involve a higher computational time. Generally, for bluff-body aerodynamics, the grid resolution is essential to capture the important flow attributes such as separation and reattachment, velocity gradients, etc. Therefore, during the modelling process, the finer mesh was defined near the edge of the buildings and boundary walls. The final grid volume is shown in Figure 5.2.

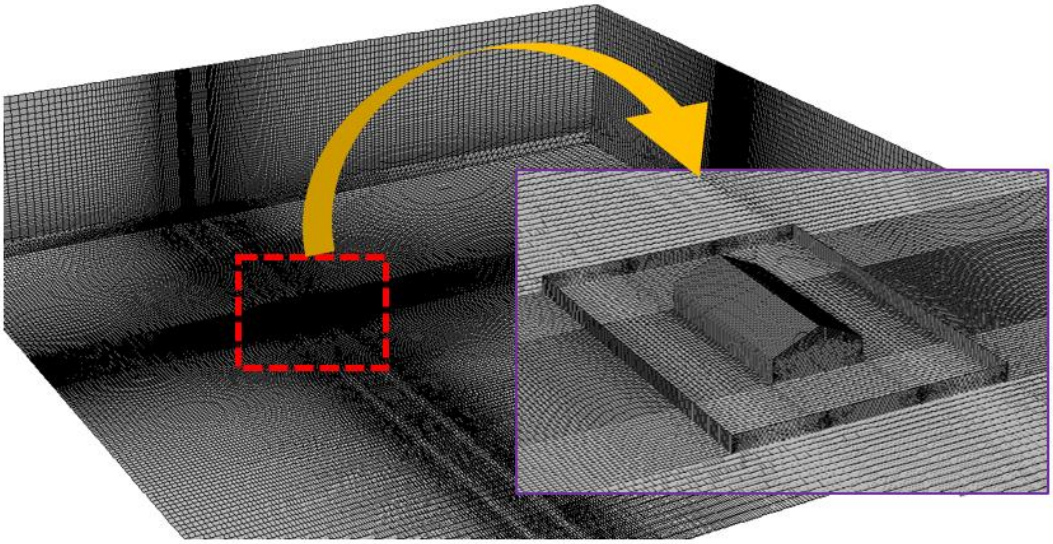

Figure 5.2: Final mesh of the computational domain

### 5.4 Boundary conditions

Appropriate boundary conditions are required to demarcate the fluid domain. The inlet was modelled as a velocity inlet while the pressure outlet option was selected for the outlet. Left, Right, and Top boundaries were modelled as symmetries. The house model, boundary walls, and the ground were modelled as wall type. However, the roughness length ($K_S$) of the ground was calculated and provided into the fluent system using the following equation. Roughness height ($z_o$) can be calculated from the wind tunnel measurements, which approximates the actual terrain profile (sub-urban exposure). $C_S$ represents the sand grain roughness coefficient which was assumed as 7, as we are using compiled UDF function. Moreover, the no-slip behavior was assumed for the ground conditions.

$$K_s = \frac{9.793 z_o}{C_s} \tag{5.1}$$

Other boundary conditions were estimated using the following equations provided by Gorle et.al, (2009) ( k – Turbulence kinetic energy, A and B are constants, κ – von-Karman constant, $U_*$ - Friction velocity.

$$k = \sqrt{A.ln(Z + Z_o) + B} \qquad \text{(From Chapter 2)}$$

$$C_\mu = \frac{U_*^4}{A.ln(Z+Z_o)+B} \qquad \text{(From Chapter 2)}$$

$$\varepsilon = \frac{\sqrt{C_\mu}U_*}{\kappa((Z+Z_o)}.(A.ln(Z + Z_o) + B) \qquad \text{(From Chapter 2)}$$

## 5.5 Turbulence model

In this study, the turbulence was approximated using the standard k-ε model. Turbulence kinetic energy (k) profile and energy dissipation rate (ε), obtained from the wind tunnel measurements using the following Eq. (2.19) and Eq. (2.21). There are different numerical equations available to estimate kinetic energy profiles using wind tunnel data. There are various turbulence models are available in the fluent inbuilt system.

## 5.6 Validation with experimental profiles

For any CFD modelling, the validation sequence is very important. Otherwise, the accuracy of the results will not be justified. Since we employ a UDF function (Refer Annex 06) to define the velocity and turbulent kinetic energy profiles at the inlet, validation of those profiles near the building is required. After wind obstructing the building and boundary walls, their profiles will change. Therefore, a suitable upstream location was selected (near to the model) to export the required profile data. Figures 5.3 to 5.5 illustrate the comparison of profiles at x = -0.2 m for the BM. For the comparison, we considered the ABL layer up to 0.5m from the ground.

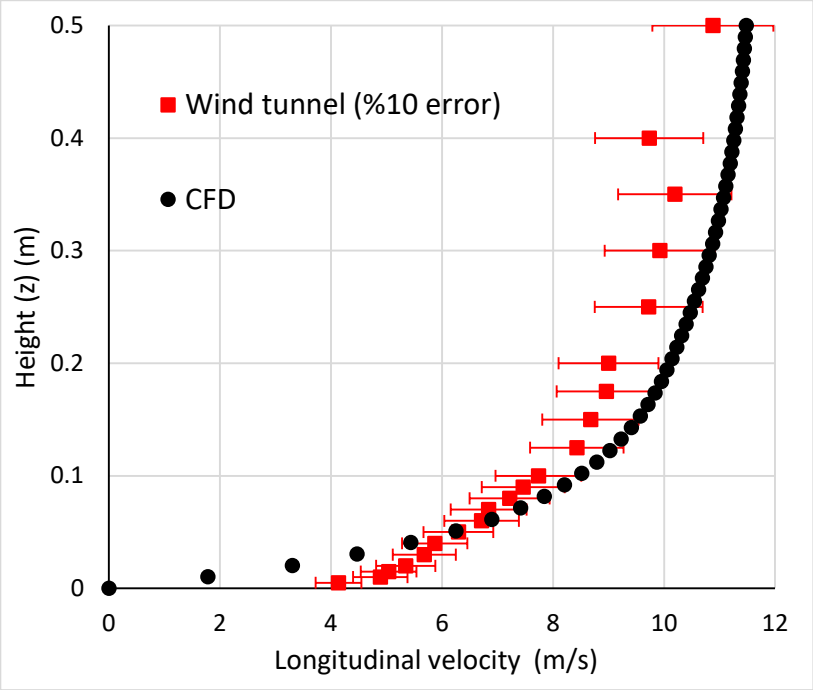


Figure 5.3. Comparison of the longitudinal velocity profile

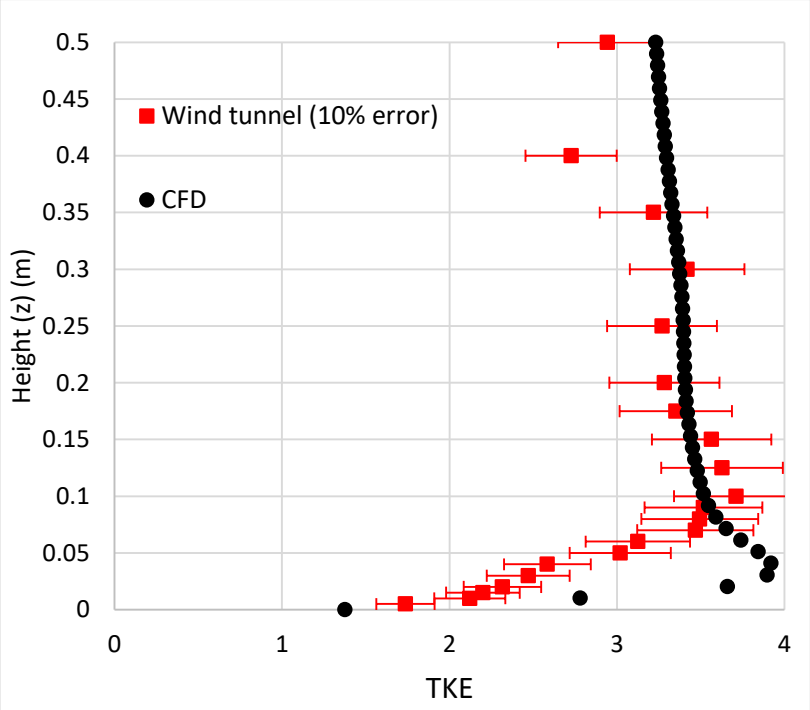


Figure 5.4. Comparison of the turbulent kinetic energy (TKE) profile

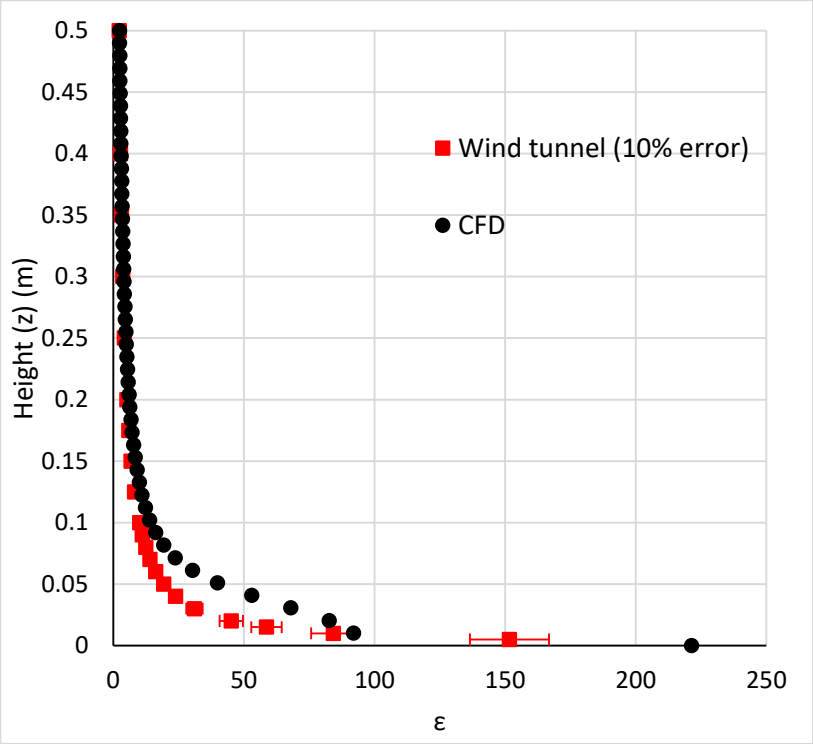


Figure 5.5. Comparison of turbulence dissipation rate (ε) profile

We obtained a good agreement between the wind tunnel results and CFD simulations. The logarithmic velocity profile which was defined at the inlet was appeared near the building model (see figure 5.3). The obtained CFD simulations were most of the time within 10% deviation from the wind tunnel observations. Similar observations were noted for the profiles of turbulent kinetic energy and turbulence dissipation profiles. Therefore, it witnesses the conditions inside the simulations follow the actual surrounding conditions inside the wind tunnel. Incorrect meshing or insufficient upstream detailing would give incorrect profiles, especially near the building model.

To support our study, the static pressure field around the house (with and without boundary walls) was investigated. Figure 5.6 to 5.9 represents the correlation between the pressure coefficients of wind tunnel measurements and CFD models, obtained at several locations at $\theta = 0°$ and $\theta = 90°$.

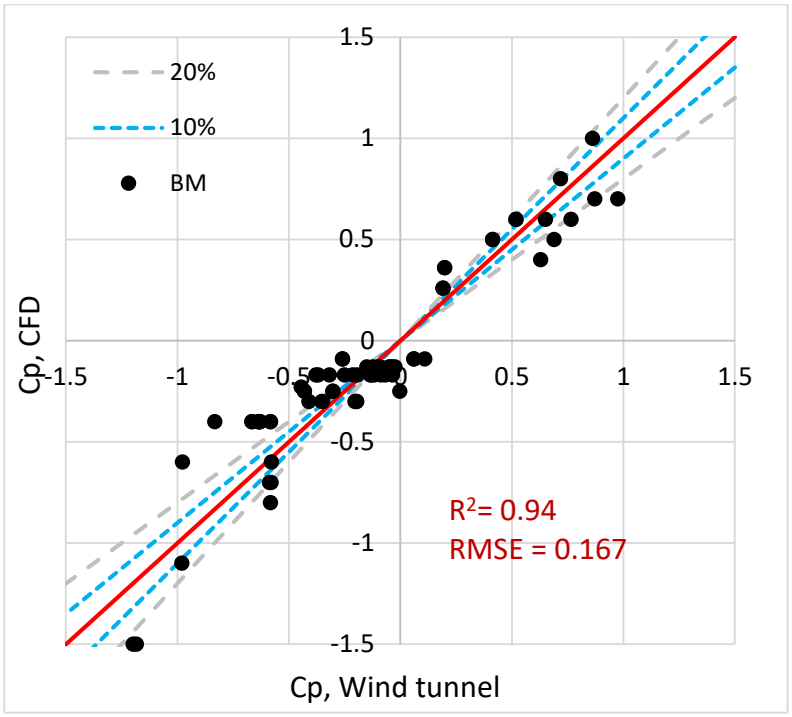


Figure 5.6: Comparison of $\overline{C_P}$ observed between wind tunnel results and CFD simulations for BM

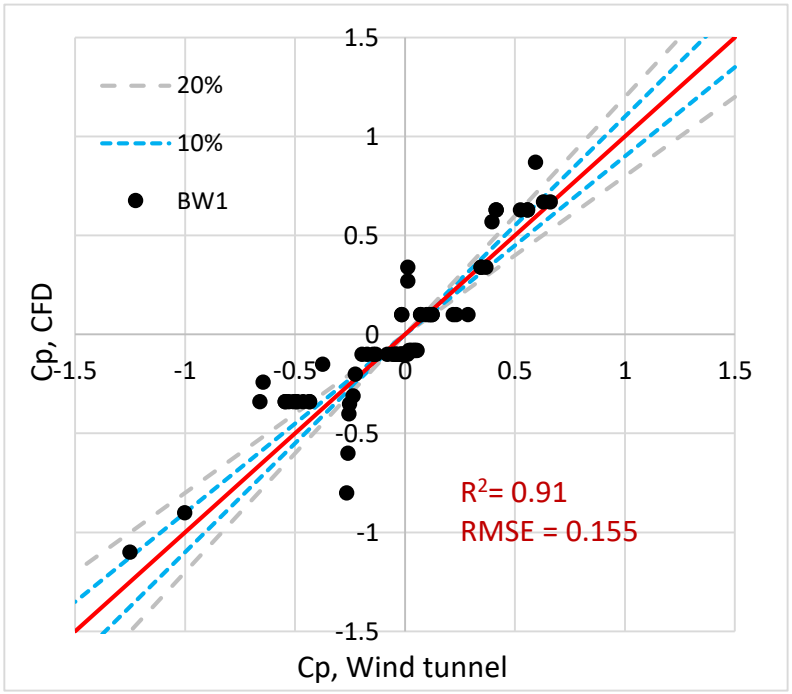


Figure 5.7: Comparison of $\overline{C_P}$ observed between wind tunnel results and CFD simulations for BW1

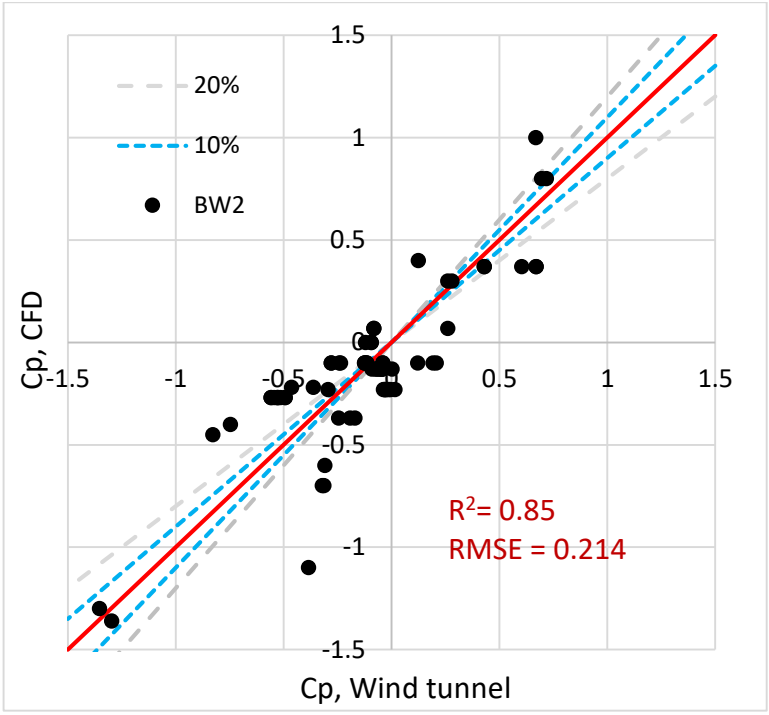


Figure 5.8: Comparison of $\overline{C_P}$ observed between wind tunnel results and CFD simulations for BW2

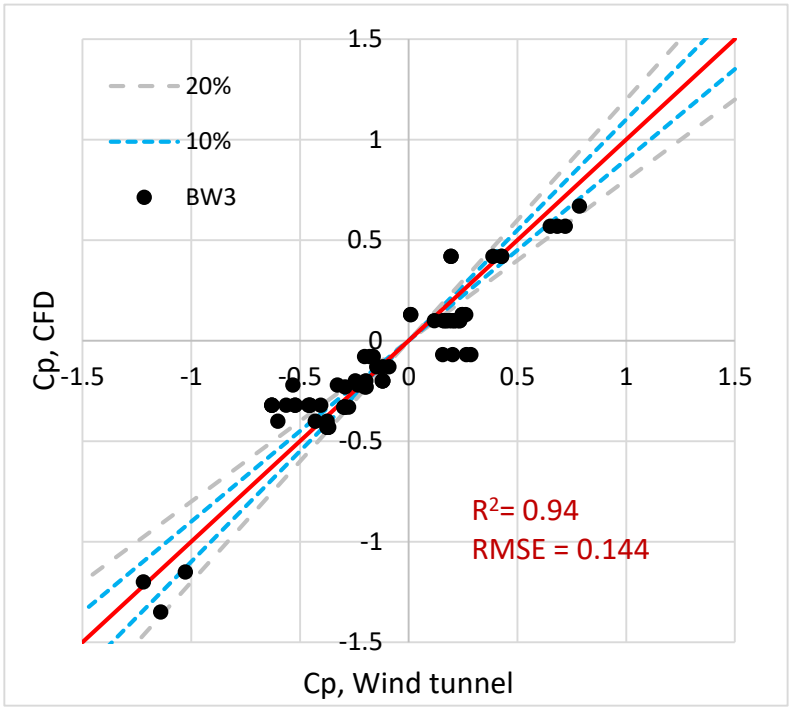


Figure 5.9: Comparison of $\overline{C_P}$ observed between wind tunnel results and CFD simulations for BW3

A good correlation was obtained between the $\overline{C_P}$ values obtained from the wind tunnel and CFD simulations. For the BM, the positive values appeared to be within 20% deviations concerning experimental values. However, notable discrepancies were obtained especially for negative values. RMSE and $R^2$ values have reached 0.167 and 0.94, respectively. It should be notified, moderately significant differences existed between the wind tunnel and CFD model for BW1. $\overline{C_P}$ values were more often following a 20% error margin. Both positive and negative Cp values of the CFD appeared to be more uniform, compared to the variations observed during the wind tunnel experiment. Compared to BW2, the CFD model has given some disrupt variations. The RMSE and $R^2$ values explain the correlation between the wind tunnel results and the CFD model has decreased a bit. In particular, negative values appeared to be more deviating from the wind tunnel observations. It is noteworthy, more deviations were observed along wind direction. The crosswind case had a moderately good agreement with the experimental values. When the BW3 is considered, $R^2$ and RMSE values have reached 0.94 and 0.144, respectively. Interestingly, both crosswind and along wind simulations had a good agreement with the wind tunnel results, similar to the BM. Further, the lowest RMSE was obtained on this occasion. Both positive and negative values appeared to be within the 20% error limit, concerning experimental observations.

In particular, the $\overline{C_P}$ values on the leeward roof seem to be relatively more uniform and less conservative. Moreover, at the ridge, all the models indicated relatively large suctions values. However, such negative values were not observed, even near the ridgeline. Therefore from the aid of CFD simulations, it can be justified the reduction of $\overline{C_P}$ values due to the influence of boundary walls. Such a simulation can be used even with varying distances to perform complex analysis. More importantly, Figures 5.10 to 5.17 display the obtained pressure contours at $\theta = 0°$ and $\theta = 90°$ for the models with and without boundary wall with the respective contours obtained from the wind tunnel. Therefore, the CFD model successfully claimed the obtained results are accurate.

## 5.7 Static pressure field of $\overline{C_P}$

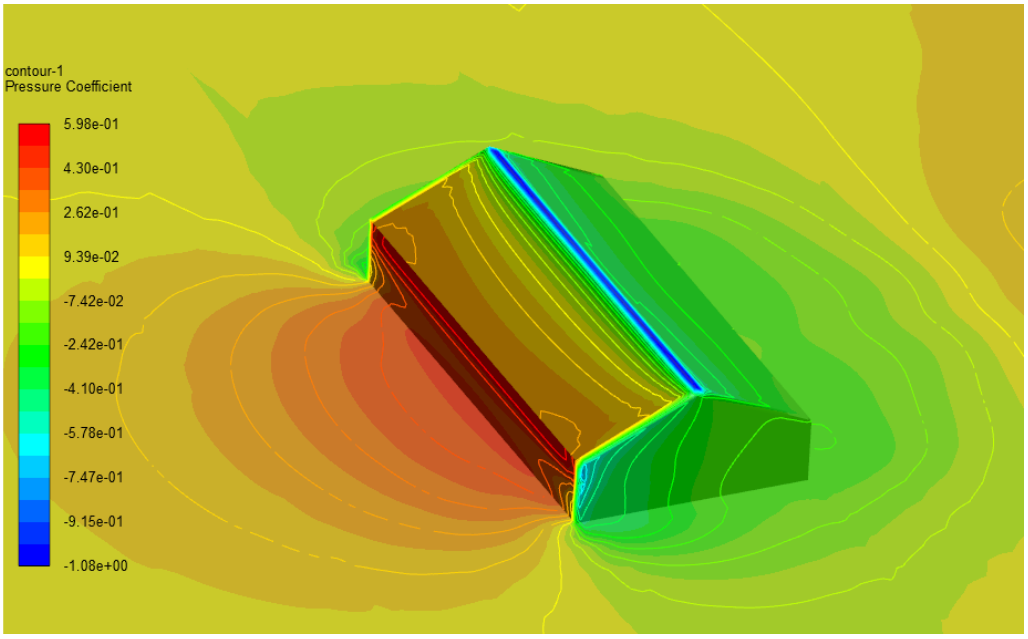


Figure 5.10. Variation of $\overline{C}_p$ for BM at θ = 0°

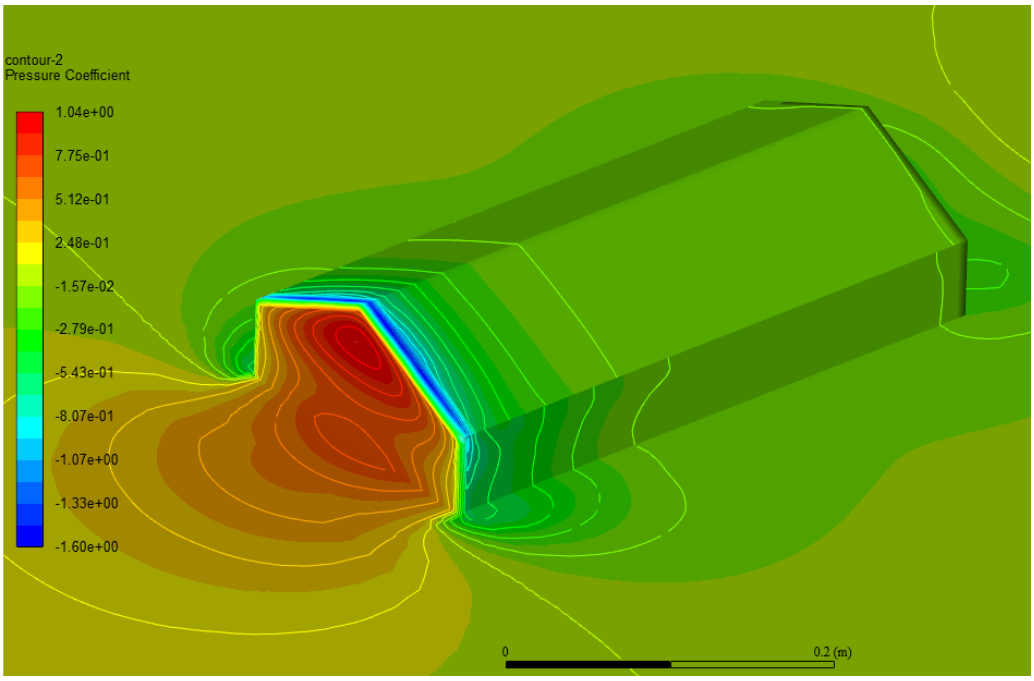


Figure 5.11. Variation of $\overline{C}_p$ for BM at θ = 90°

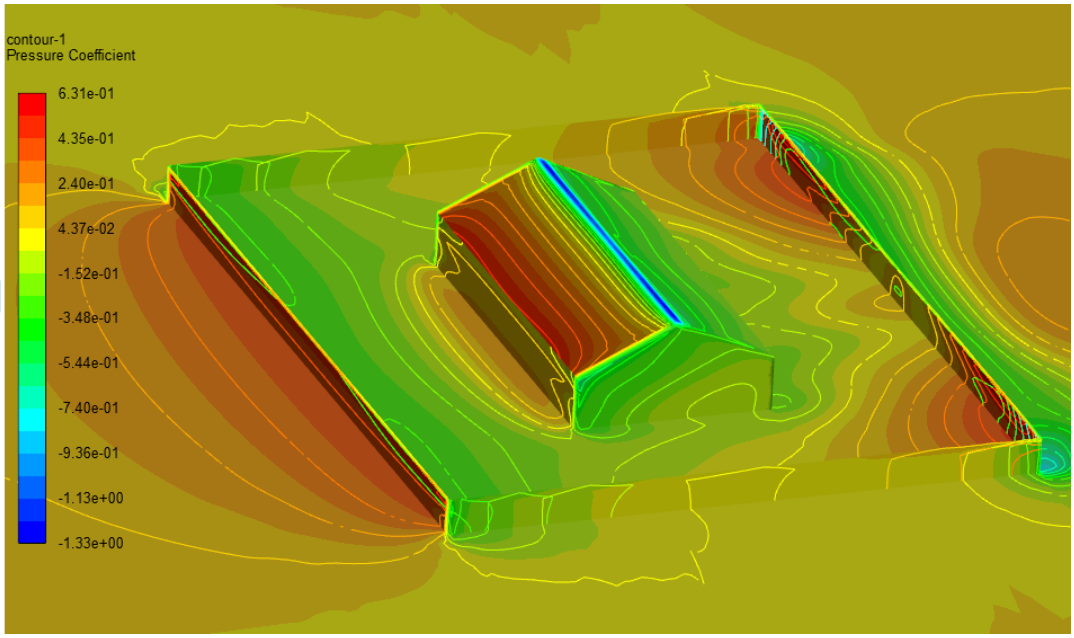


Figure 5.12. Variation of $\bar{C}_p$ for BW1 at θ = 0°

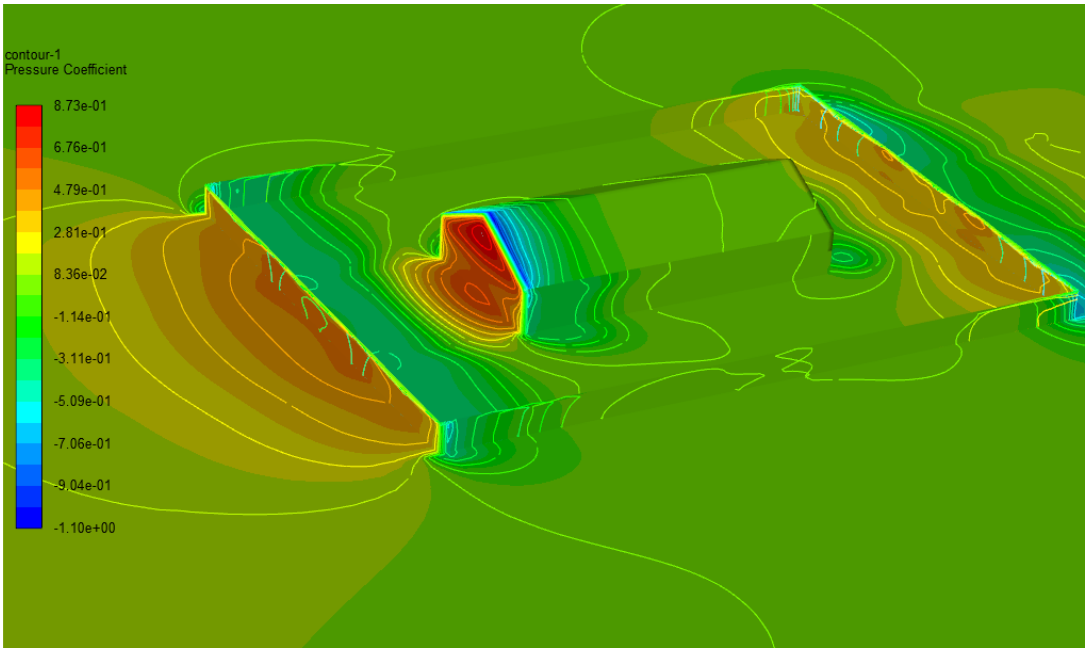


Figure 5.13. Variation of $\bar{C}_p$ for BW1 at θ = 90°

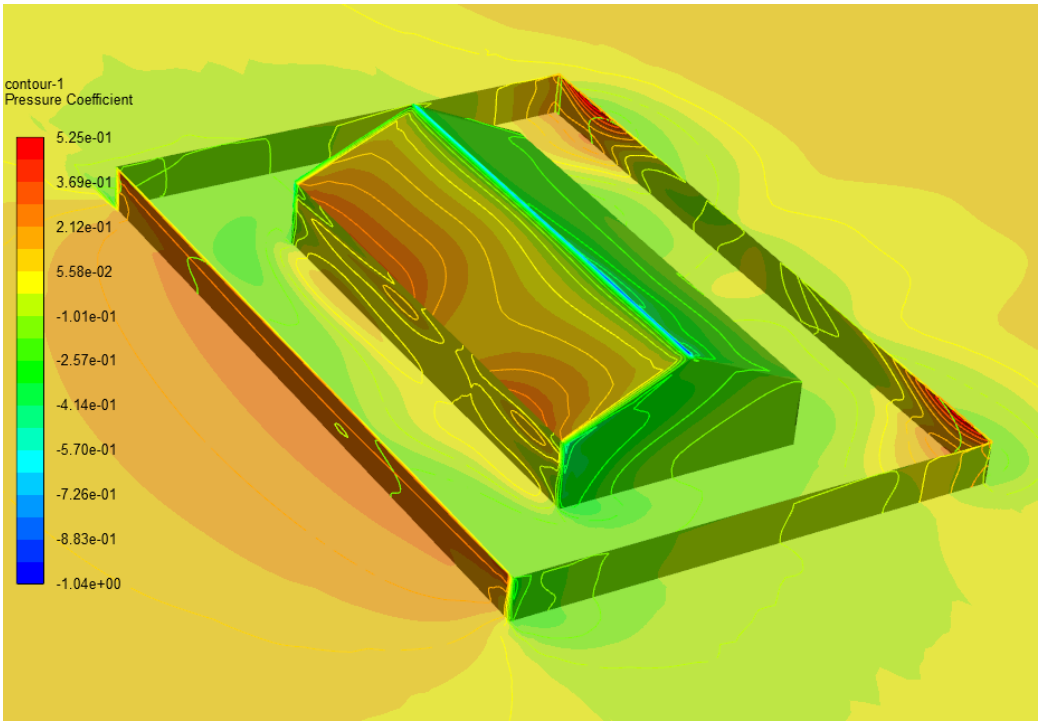


Figure 5.14. Variation of $\bar{C}_p$ for BW2 at θ = 0°

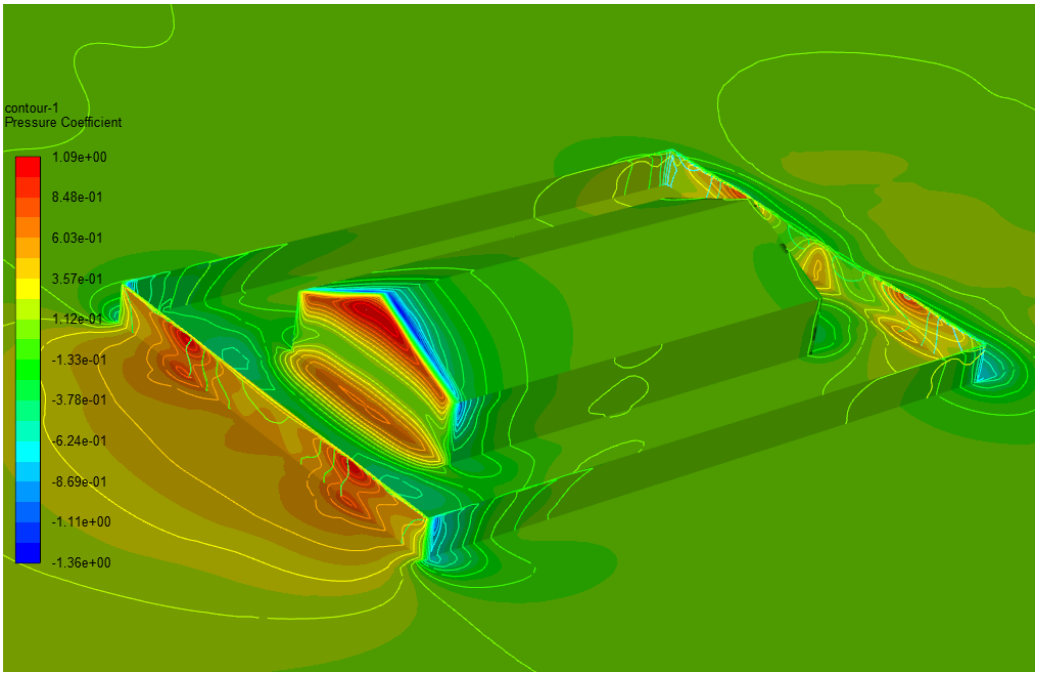


Figure 5.15. Variation of $\bar{C}_p$ for BW2 at θ = 90°

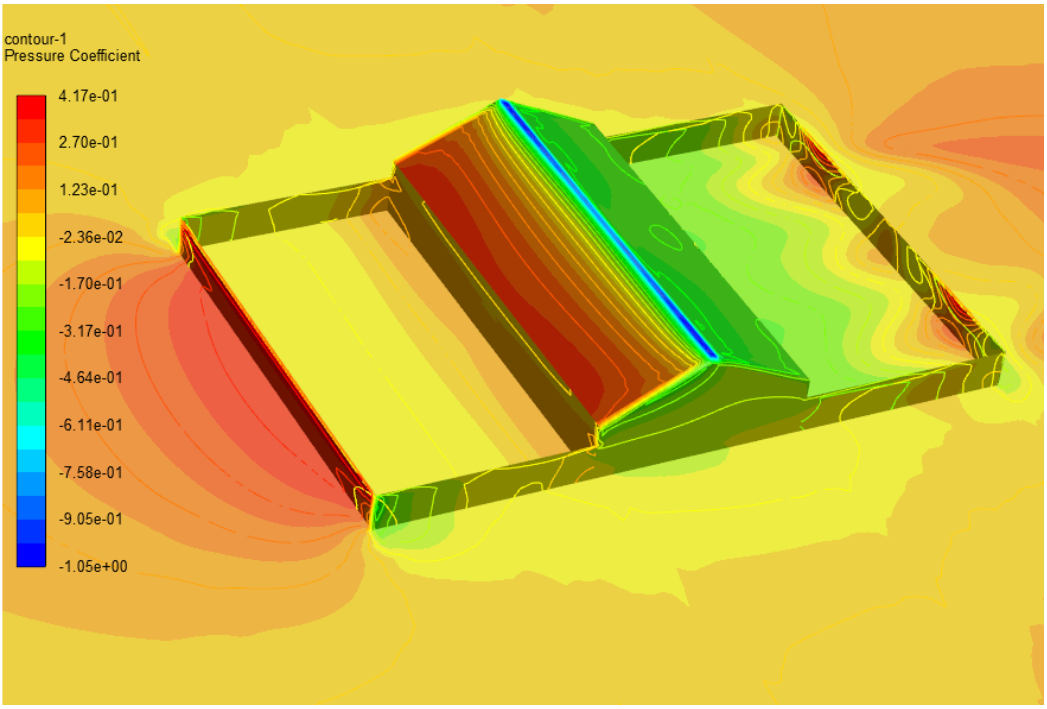


Figure 5.16. Variation of $\bar{C}_p$ for BW3 at θ = 0°

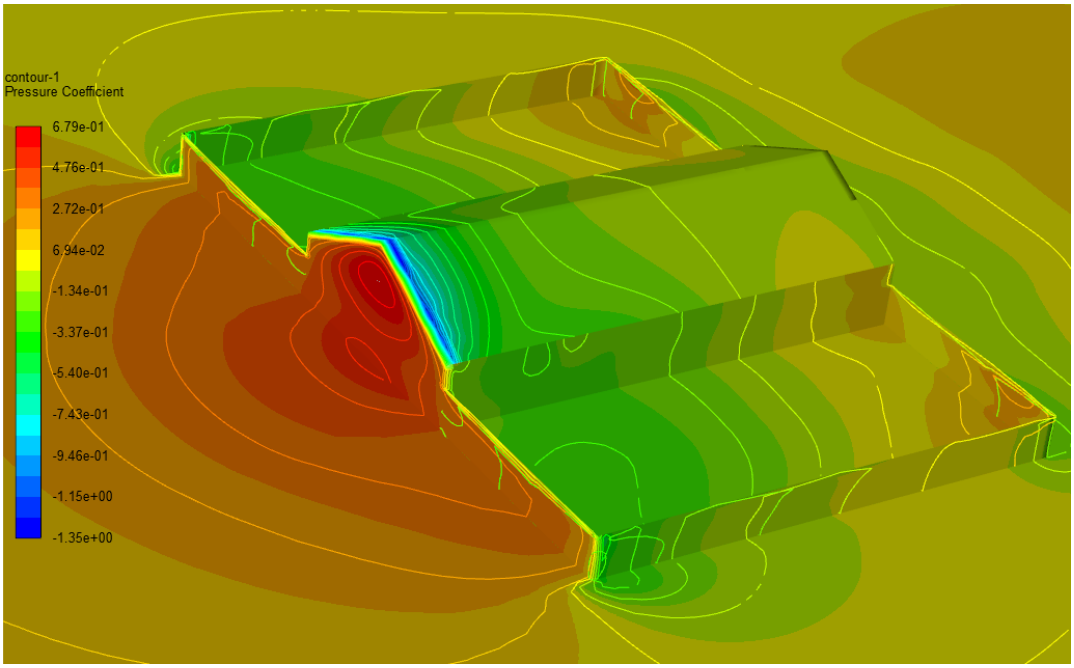


Figure 5.17. Variation of $\bar{C}_p$ for BW3 at θ = 90°

## 5.8 Summary of the Chapter

This chapter described the CFD simulations performed on the low-rise gable-roofed building with boundary walls. Foremost, the mesh was the most important aspect that affects the accuracy of the CFD results. The simulated velocity, turbulent kinetic energy, and turbulent dissipation rate profiles (upstream of the buildings) were in good agreement with the wind tunnel results. The $\bar{C}_p$ values obtained from the CFD simulations at $\theta = 0°$ and $\theta = 90°$ confirmed the effect of boundary walls on the flow field follows the experimental observations. Therefore, we claim a reduction in the external pressure coefficients of a low-rise gable-roof house in the presence of boundary walls.

# 6. CONCLUSIONS AND RECOMMENDATION

Recent advancements in the wind engineering field identified the pressure field around a low-rise building strongly depends on the surrounding interference. Compared to large-scale objects, smaller objects such as boundary walls can modify the wind flow around a low-rise structure. This thesis has conferred a detailed wind tunnel study on the external pressure variation of low-rise contemporary houses in the presence of boundary walls.

Compared to the wind tunnel results, the exsisting pressure coefficients (AS/NZS 1170.2 2011, ASCE 07-2016, EN 1991-1-4 2005, NBCC 2015) appeared to be moderately conservative. In fact, the boundary walls altered not only the magnitude of pressure but also the distribution over the surface. The experiment claimed the largest reduction in the pressure coefficients when the boundary walls were located at a 2H distance away from the house (H is the full height of the building). Further, the distinct configurations of boundary walls confirmed, both lateral and upstream separation distances uniquely influence the pressure field.

A similar reduction in the pressure coefficients was observed during the direction analysis of the mean pressure coefficients. Especially, the negative pressure at perimeter zones of roofs and walls has reduced its intensity in the presence of boundary walls. It was observed the intensity of flow separation has also decreased on both walls and roofs, and flow reattachments were visible towards the trailing edge of the walls. The isolated model captured intense diagonal bands of vortices at roof corners and the apex of the gable end. Interestingly, the boundary walls have influenced reducing the intensity of formed vortices at those locations. However, the vortex intensity at the apex of the gable end appeared to be more disrupted and less dependent on boundary walls.

The external pressure distribution on the building envelope can be introduced as a complex process that is contributed by flow separation, reattachment, and turbulence intensities. Wind tunnel results witnessed that, highly fluctuating loads can be expected and these loads are caused by intermittent extreme events, influenced by the

above factors. These peaks are moving on the surface having distinct lag times. Compared to the mean pressure coefficients, peak pressure coefficients exhibited moderately low dependency on the boundary walls. However, the worst peak at vulnerable locations has decreased due to the effect of boundary walls. Moreover, the correlation between boundary walls has increased, which highlights the less dependency of the results to different lateral and upstream separation distances. Further, the synchrony of the peak events has increased slightly with the effect of boundary walls in the near vicinity.

Further, this study was able to achieve a witness the modification on the flow field in the presence of boundary walls, using CFD simulations. The numerical simulation confirmed the boundary walls can influence the magnitude of external pressure to be reduced. The velocity profile, Turbulence kinetic energy profile, and the turbulence dissipation rate profile were in good agreement with the obtained profiles in the wind tunnel. Similarly, comparable pressure coefficient values were obtained from the CFD post-processing in contrast to experimental observations. However, there were several occasions where the pressure coefficients exceed the 20% error limit.

Interestingly, the boundary walls altered the magnitude and the spatial variation of the external pressure distribution on low-rise gable-roofed houses. Design wind loading standards have failed in capturing such variations due to the nearby shielding objects. Moreover, including this research study, there are very few attempts reported in the literature regarding the interference effect of boundary walls on low-buildings. Despite the magnitude, mean pressure and peak pressure coefficients reduced in the presence of boundary walls, particularly in perimeter zones. Therefore, the study suggests recent revisions in the wind loading standards to compensate for the effect in the presence of surrounding boundary walls. However, such an attempt should be made considering various geometry configurations, through a series of experiments. Hence, further experimental works are strongly suggested on the external pressure variation of low-buildings (Gable, Hipped, Flat roofed) with various boundary wall (porous/non-porous) configurations with varying lateral and upstream separation.

# 7. REFERENCES


AIJ. (2004). *Recommendations for loads on buildings." AIJ-RLB-2004*.

Alrawashdeh, H., & Stathopoulos, T. (2015). Wind pressures on large roofs of low buildings and wind codes and standards. *Journal of Wind Engineering and Industrial Aerodynamics*, *147*, 212–225. http://dx.doi.org/10.1016/j.jweia.2015.09.014

*ASCE/SEI 7, 2016. Minimum Design Loads for Buildings and Other Structures.* (2016). Structural Engineering Institute of ASCE.

*AS/NZS 1170.2 (2011) Structural Design Actions, Part 2: Wind Actions", Australian/ New Zealand Standard*. (n.d.).

AWES. (1994). *Quality assurance manual–Cladding pressure and environmental wind studies*. AWESQAM-1-1994, Sydney.

Bailey, A. (1933). *Wind pressures on buildings*. The Institution of Civil Engineers.

Bailey, A., & Vincent, N. D. G. (1943). Wind pressure on buildings, including effects of adjacent buildings. *J. Inst. Or. Eng*, *20*, 243.

BCJ. (2008). *Guide book on wind tunnel testing of building structures for practitioners (translated)*.

Bitsuamlak, G. T., Warsido, W., Ledesma, E., & Chowdhury, A. G. (2013). Aerodynamic Mitigation of Roof and Wall Corner Suctions Using Simple Architectural Elements. *Journal of Engineering Mechanics*, *139*, 396–408.

Blocken, B., Stathopoulos, T., & Carmeliet, J. (2007). CFD simulation of the atmospheric boundary layer: Wall function problems. *Atmospheric Environment*, *41*(2), 238–252. https://doi.org/10.1016/j.atmosenv.2006.08.019

Boughton, G., Henderson, D. J., Ginger, J. D., Holmes, J. D., Walker, G. R., Leitch, C., Somerville, L. R., Frye, U., Jayasinghe, N. C., & Kim, P. (2011). *Tropical cyclone Yasi structural damage to buildings* (No. TR57).

Boughton, G., & Reardon, G. F. (1982). *Simulater wind tests on a house*, (No. TR14). Cyclone testing station, James cook university.

Boughton, G., & Reardon, G. F. (1983). *Testing a high set house designed for 42 m/s winds* (No. 19). Cyclone testing station, James cook university.

Boughton, G., & Reardon, G. F. (1984). *Simulated wind load test on the Tongan hurricane house* (No. TR23). Cyclone testing station, James cook university.

Bounkin, K., & Tcheremoukhin, A. (1928). Wind pressures on roofs and walls of buildings. *Central Aero-Hydrodynamical Inst*.

Cebeci, O. Z. (1987). Strength of concrete in warm and dry environment. *Materials and Structures*, *20*(4), 270–272. https://doi.org/10.1007/BF02485923

Celik, I. B. (1999). *Introductory Turbulence Modeling. Lectures Notes, Mechanical & Aerospace Engineering Deartment,West Virginia University*.

Cermak, J. E. (1975). Applications of fluid mechanics to wind engineering- A freeman scholar lecture. *Journal of Fluids Engineering*, *97*(1), 9–38. https://doi.org/10.1115/1.3447225

Chang, C. H., & Meroney, R. N. (2003). The effect of surroundings with different separation distances on surface pressures on low-rise buildings. *Journal of Wind Engineering and Industrial Aerodynamics*, *91*(8), 1039–1050.

Chen, J. H. (2012). A Study on the Selection of Optimal Roof Type for Low-rise buildings group—In a View of Wind Pressures Action. *Procedia Engineering*, 1149–1154.

Cook, N. J., & Mayne, J. R. (1979). A novel working approach to the assessment of wind loads for equivalent static design. *Journal of Wind Engineering and Industrial Aerodynamics*, *4*(2), 149–164.

Dagliesh, W. A., & Templin, J. T. (1980). Comparisons of wind tunnel and full-scale building surface pressures with emphasis on peaks. *Proc., 5th Int. Conf. on Wind Engineering*.

Davenport, A. G. (1964). Note on the distribution of the largest value of a random function with application to gust loading. *Proceedings of the Institution of Civil Engineers, Paper No.6739*, *28*, 187–196.

Davenport, A. G., & Isyumov, N. (1967). The application of the boundary layer wind tunnel to the prediction of wind loading. *Proc. International Research Seminar on Wind Effects on Buildings and Structures*, 201–230.

*EN 1991-1-4, Eurocode 1, 2005: Actions on Structures-General Actions-Part 1-4. Wind Actions, European Standard*. (2005).

Fouad, N. S., Mahmoud, G. H., & Nasr, N. E. (2018). Comparative study of international codes wind loads and CFD results for low rise buildings. *Alexandria Engineering Journal*, *57*, 3623–3639.

Franke, J., Hellsten, A., Schlunzen, K. H., & Carissimo, B. (2011). The COST 732 Best Practice Guideline for CFD simulation of flows in the urban environment: A summary. *International Journal of Environment and Pollution*, *44*(1–4), 419–427. https://doi.org/10.1504/IJEP.2011.038443

Gavanski, E., Gurley, K. R., & Kopp, G. A. (2016). Uncertainties in the Estimation of Local Peak Pressures on Low-Rise Buildings by Using the Gumbel Distribution Fitting Approach. *Journal of Structural Engineering*. https://doi.org/10.1061/(ASCE)ST.1943-541X.0001556

Geurts, C. P. W. (2001). Transparency of pressure and force coefficients. *Proc., 3rd European and African Conf. on Wind Engineering*, 165–172.

Geurts, C. P. W., Kopp, G. A., & Morrison, M. J. (2013). A review of the wind loading zones for flat roofs in code provisions. *Proc., 6th European and African Conf. on Wind Engineering*, 1–6.

Ginger, J. D., Reardon, G. F., & Whitebread, B. J. (1999). Wind load effects and equivalent ressures on low-rise house roofs. *Engineering Structures*, *22*, 638–646.

Gorlé, C., van Beeck, J., Rambaud, P., & Van Tendeloo, G. (2009). CFD modelling of small particle dispersion: The influence of the turbulence kinetic energy in the atmospheric boundary layer. *Atmospheric Environment*, *43*(3), 673–681. https://doi.org/10.1016/j.atmosenv.2008.09.060

Habte, F., Chowdhury, A. G., & Zisis, I. (2017). Effect of wind-induced internal pressure on local frame forces of low-rise buildings. *Engineering Structures*, *143*, 455–468.

Hargreaves, D. M., & Wright, N. G. (2007). On the use of the k–ε model in commercial CFD software to model the neutral atmospheric boundary layer. *Journal of Wind Engineering and Industrial Aerodynamics*, *95*(5), 355–369. https://doi.org/10.1016/j.jweia.2006.08.002

Henderson, D. J., Ginger, J. D., Leitch, C., Boughton, G., & Falck, D. (2006). *Tropical cyclone Larry- Damage to buildings in the innisfail aera* (No. TR51). Cyclone testing station, James cook university.

Ho, T. C. E., Surry, D., & Davenport, A. G. (1991). Variability of low building wind loads due to surroundings. *Journal of Wind Engineering and Industrial Aerodynamics*, *38*, 297–310.

Holmes, J. D. (1983). *Wind loads on low-rise buildings—A review*. CSIRO.

Holmes, J. D. (1985). Wind action on glass and Brown's integral. *Engineering Structures*, *4*, 226–230.

Holmes, J. D. (1986). Wind Pressures on Tropical Building Low-Rise Building. *Journal of Wind Engineeringand IndustrialAerodynamic*, *53*(1–2), 105–123.

Holmes, J. D. (2001). *Wind Loading of Structures*. Taylor & Francis.

Holmes, J. D., & Cochran, L. S. (2003). Probability distributions of extreme pressure coefficients. *Journal of Wind Engineering and Industrial Aerodynamics*, *91*, 893–901. https://doi.org/10.1016/S0167-6105(03)00019-9

Holmes, J. D., & Ginger, J. D. (2012). Internal pressures – the dominant windward opening case – a review. *Journal of Wind Engineering and Industrial Aerodynamics*, 70–76.

Holmes, J. D., & Moriarty, W. W. (1999). Application of the generalized Pareto distribution to extreme value analysis in wind engineering. *Journal of Wind Engineering and Industrial Aerodynamics*, *83*(1–3), 1–10.

Hosking, J. R. M., Wallis, J. R., & Wood, E. F. (1985). Estimation of the Generalized ExtremeValue Distribution by the Method of Probability-Weight. *TECHNOMETRICS*, *27*(3), 251–261.

Hoven, V. D. (1957). Power spectrum of horizontal wind speed in the frequency range from 0.0007 to 900 cycles per hour. *Journal of Meteorology*, *14*, 160–164.

Hoxey, R. P. (1991). Structural Response of a Portal Framed Building under Wind Load. *Journal of Wind Engineering and Industrial Aerodynamics*, *38*, 347–356.

Hussain, M., & Lee, B. E. (1980). A wind tunnel study of the mean pressure forces acting on large groups of low-rise buildings. *Journal of Wind Engineering & Industrial Aerodynamics*, *6*, 207–225.

ISO. (2009). *Wind actions on structures. ISO 4354:2009.*

Jayasinghe, N. C. (2012). *The distribution of wind loads and vulnerability of metal clad roofing structures in contemporary Austalian houses* [PhD thesis, James Cook University]. http://researchonline.jcu.edu.au/39226/

Jenson, M. (1958). The Model-law for Phenomena in Natural Wind. *Ingenioren*, *2*, 121–128.

Jenson, M. (1967). Some lessons learned in building aerodynamics research. *Proc. Int. Res. Seminar on Wind Effects on Buildings and Structures*.

John, A. D. (2009). *Effect of architectural features on wind load in buildings* [PhD thesis]. Department of Civil Engineering, Indian Institute of Technology Roorkee.

John, A. D., Gairola, A., & Mukherjee, M. (2009). Effect of Boundary Wall on Wind Pressure Coefficients on A Low-Rise Building. *Journal of Wind and Engineering*, *6*(1), 10–18.

Kanda, M., & Maruta, E. (1993). Characteristics of fluctuating wind pressure on long low—Rise buildings with gable roofs. *Journal of Wind Engineeringand Industrial Aerodynamics*, *50*, 173–182.

Kasperski, M. (1997). *Specification and codification of design wind loads* [Rep., Fakultat fur Bauingenieurwesen].

Kasperski, M. (2003). Specification of the design wind load based on wind tunnel experiments. *Journal of Wind Engineering and Industrial Aerodynamics, 91*(4), 527–541.

Kim, Y. C., Yoshida, A., & Tamura, Y. (2012). Characteristics of surface wind pressures on low-rise building located among large group of surrounding buildings. *Engineering Structures*, *35*, 18–28.

Kopp, G. A., & Morrison, M. J. (2018). Component and cladding wind loads for low-slope roofs on low-rise buildings. *Journal of Strucutral Engineering*, *144*(4).

Krishna, P. (1995h). Wind loads on low rise buildings—A review. *Journal of Wind Engineering and Industrial Aerodynamics*, *54/55*.

Leitch, C., Ginger, J. D., Harper, B., Kim, P., Jayasinghe, N. C., & Somerville, L. R. (2010). Performance of housing in Brisbane following storms on 16 november 2008. *Australian Journal of Structural Engineering*, *11*(1).

Li, B., Liu, J., Luo, F., & Man, X. (2015). *Evaluation of CFD Simulation Using Various Turbulence Models for Wind Pressure on Buildings Based on Wind Tunnel Experiments*. *121*, 2209–2216.

Li, G., Gan, S., Li, Y., & Wang, L. (2017). Wind-induced interference effects on low-rise buildings with gable roof. *Journal of Wind Engineering and Industrial Aerodynamics*, *170*, 94–106. https://doi.org/10.1016/j.jweia.2017.07.009

Li, Q. S., Hu, S. Y., Da, Y. M., & Li, Z. M. (2009). Extreme-value analysis for field measured peak pressure coefficients on a low-rise building. *The Seventh Asia-Pacific Conference on Wind Engineering, November 8-12, ,*.

Liu, H. (1991). *Wind Engineering, A Handbook for Structural Engineers*.

Liu, S., Pan, W., Zhao, X., Zhang, H., Cheng, X., Long, Z., & Chen, Q. (2018). Influence of surrounding buildings on wind flow around a building predicted by CFD simulations. *Building and Environment*, *140*, 1–10.

Longo, R., Ferrarotti, M., Sánchez, C. G., Derudi, M., & Parente, A. (2017). Advanced turbulence models and boundary conditions for flows around different configurations of ground-mounted buildings. *Journal of Wind Engineering and Industrial Aerodynamics*, *167*, 160–182. https://doi.org/10.1016/j.jweia.2017.04.015

Massimiliano, G., & Vittorio, G. (2002). Damage Accumulation in Glass Plates. *Journal of Engineer Mechanics, ASCE*, *7*, 801–805.

Meecham, D., Surry, D., & Davenport, A. G. (1991). The Magnitude and Distribution of WindInduced Pressures on Hip and Gabled Roofs. *Journal of Wind Engineering and Industrial Aerodynamics*, *38*, 257–272.

Meroney, R. N., & Neff, D. E. (1982). Dispersion of vapour from liquid natural gas spills-evaluation of simulation in a meteorological wind tunnel. *Journal of Wind Engineeringand IndustrialAerodynamic*, *10*(1), 1–19. https://doi.org/10.1016/0167-6105(82)90050-2

Moravej, M., Irwin, P., Chowdhury, A. G., & Hajra, B. (2017). Effects of roof height on local pressure and velocity coefficients on building roofs. *Engineering Structures*, *150*, 693–710.

*NBC2015, 2015. User's Guide-NBC 2015, Structural Commentaries (Part 4). Issued by the Canadian Commission on Buildings and Fire Codes, National Research Council of Canada*. (n.d.).

Ong, R. H., Patruno, L., Yeo, D., He, Y., & Kwok, K. C. S. (2020). Numerical simulation of wind-induced mean and peak pressures around a low-rise structure. *Engineering Structures*, *214*.

Parackal, K. I. (2018). *The Structural Response and Progressive Failure of Batten to Rafter Connections under Wind Loads* [Doctoral Thesis]. James Cook University.

Parackal, K. I., Ginger, J. D., & Henderson, D. J. (2018). Wind load fluctuations on roof batten to rafter/truss connections. *Journal of Wind Engineering & Industrial Aerodynamics*, 193–201.

Parente, A., Gorle, C., Van Beck, J., & Benocci, C. (2010). *RANS simulation of ABL flows: Application of advanced wall boundary conditions to configurations with mixed rough and smooth surfaces*. http://hdl.handle.net/2013/

Parente, A., Gorlé, C., van Beeck, J., & Benocci, C. (2011a). Improved k–ε model and wall function formulation for the RANS simulation of ABL flows. *Journal of*

*Wind Engineering and Industrial Aerodynamics*, *99*(4), 267–278. https://doi.org/10.1016/j.jweia.2010.12.017

Parente, A., Gorlé, C., van Beeck, J., & Benocci, C. (2011b). A Comprehensive Modelling Approach for the Neutral Atmospheric Boundary Layer: Consistent Inflow Conditions, Wall Function and Turbulence Model. *Boundary-Layer Meteorology*, *140*(3), 411. https://doi.org/10.1007/s10546-011-9621-5

Parente, A., Longo, R., & Ferrarotti, M. (2019). *Turbulence model formulation and dispersion modelling for the CFD simulation of flows around obstacles and on complex terrains*. https://doi.org/10.35294/ls201903.parente

Peterka, J. A. (1983). Selection of local peak pressure coefficients for wind tunnel studies of buildings. *Journal of Wind Engineeringand Industrial Aerodynamics*, *13*, 477–488.

Pindado, S., & Meseguer, J. (2003). Wind tunnel study on the influence of different parapets on the roof pressure distribution of low-rise buildings. *Journal of Wind Engineering and Industrial Aerodynamics*, *91*, 1133–1139.

Prasad, D., Uliate, T., & Ahmed, M. R. (2009). Wind Loads on Low-Rise Building Models with Different Roof Configurations. *International Journal of Fluid Mechanics Research*.

Quan, Y., Wang, F., & Gu, M. (2014). A Method for Estimation of Extreme Values of Wind Pressure on Buildings Based on the Generalized Extreme-Value Theory.

*Hindawi Publishing Corporation Mathematical Problems in Engineering*, *2014*. http://dx.doi.org/10.1155/2014/926253

Reardon, G. F., Walker, G. R., & Jancauskas, E. D. (1986). *Effects of cyclone winifred on buildings*, (No. TR27). Cyclone testing station, James cook university.

Richards, P. J., & Hoxey, R. P. (1993). Appropriate boundary conditions for computational wind engineering models using the k-ϵ turbulence model. *Journal of Wind Engineering and Industrial Aerodynamics*, *46–47*, 145–153. https://doi.org/10.1016/0167-6105(93)90124-7

Richardson, G. M., & Surry, D. (1991). Comparisons of wind-tunnel and full-scale surface pressure measurements on low-rise pitched-roof buildings. *Journal of Wind Engineering and Industrial Aerodynamics*, *38*, 249–256.

Roberston, A. P. (1991). Effect of Eaves Detail on Wind Pressures Over an Industrial Building. *Journal of Wind Engineering and Industrial Aerodynamics*, *38*, 325–333.

Rodi, W. (1997). Comparison of LES and RANS calculations of the flow around bluff bodies. *Journal of Wind Engineering and Industrial Aerodynamics*, *69–71*, 55–75. https://doi.org/10.1016/S0167-6105(97)00147-5

Sadek, F., & Simiu, E. (2002). Peak Non-Gaussian Wind Effects for Database-Assisted Low-Rise Building Design. *Journal of Engineering Mechanics*, *128*(5), 530–539. https://doi.org/10.1061/~ASCE!0733-9399~2002!128:5~530!

Shah, K. B., & Ferziger, J. H. (1997). A fluid mechanicians view of wind engineering: Large eddy simulation of flow past a cubic obstacle. *Journal of Wind Engineering and Industrial Aerodynamics*, *67–68*, 211–224. https://doi.org/10.1016/S0167-6105(97)00074-3

Simiu, E., & Yeo, D. (2019). *Wind effects on structures: Modern structural design for wind* (4th ed.). John Wiley & Sons Ltd.

Sockel, H. (1980). Local pressure fluctuations. *Proc., 5th Int. Conf. on Wind Engineering*.

Stathopoulos, T. (1979). *Turbulent Wind Action on Low-rise Buildings* [Ph.D. Thesis]. University of Western Ontario.

Stathopoulos, T. (1984). Wind loads on low-rise buildings: A review of the state of the art. *Engineering Structures*, *6*, 119–135.

Stathopoulos, T., & Baniotopoulos, C. C. (2007). *Wind Effects on Buildings and Design of WindSensitive Structures*. SpringerWeinNewYork.

Stathopoulos, T., & Surry, D. (1983). *Scale Effects in Wind Tunnel Testing of Low Buildings*. *13*, 313–326.

Tamura, Y., & Kareem, A. (2013). *Advanced Structural Wind Engineering*.

Tieleman, H. W. (2003). Wind tunnel simulation of wind loading on low-rise structures: A review. *Journal of Wind Engineering and Industrial Aerodynamics*, *91*, 1627–1649.

Tieleman, H. W., Akins, R. E., & Sparks, P. R. (1981). Comparison of wind tunnel and full-scale wind pressure ,measurements on low-rise buildings. *Journal of Wind Engineering and Industrial Aerodynamics*.

Tieleman, H. W., Ge, Z., & Hajj, M. R. (2007). Theoretically estimated peak wind loads. *Journal of Wind Engineering and Industrial Aerodynamics*, *95*, 113–132. https://doi.org/10.1016/j.jweia.2006.05.004

Tominga, Y., Mochida, A., & Yoshie, R. (2008). AIJ guidelines for practical applications of CFD to pedestrian wind environment around buildings. *Journal of Wind Engineering and Industrial Aerodynamics*, 1749–1761.

Tong, Z., Chen, Y., & Malkawi, A. (2016). Defining the Influence Region in neighborhood-scale CFD simulations for natural ventilation design. *Applied Energy*, *182*, 625–633.

Uematsu, Y., & Isyumov, N. (1999). Review -Wind pressures acting on low-rise buildings. *Journal of Wind Engineeringand IndustrialAerodynamic*, *82*, 1–25.

Vickery, B. J. (1976). *Wind loadson low rise buildings*. D.R.C. Seminar,.

Walker, G. R. (1995). *Report on Cyclone tracy-effect on buildings*. Australian department of housing and construction.

Walker, G. R., & Roy, R. J. (1985). *Wind loads on houses in an urban environment,*. Asia Pacific Syrup. on Wind Engineering, India.

Wieringa, J. (1992). Updating the Davenport rou(jhness classification. *Journal of Wind Engineering and IndustrialAerodynamic*, *41*(44), 357–368.

WMO. (1989). *Statistical distributions for flood frequency analysis* (No. 33). Secretariat of the world meteorological organization - geneva - switzerland.

Xie, Z.-T., & Castro, I. P. (2009). Large-eddy simulation for flow and dispersion in urban streets. *Atmospheric Environment*, *43*(13), 2174–2185. https://doi.org/10.1016/j.atmosenv.2009.01.016

## Annex 1

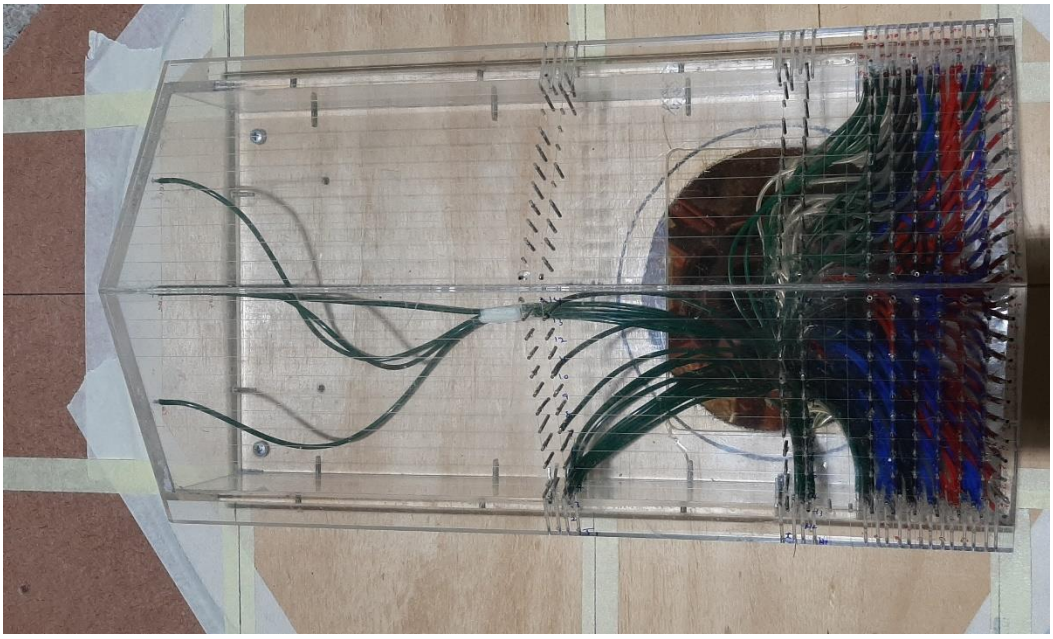

## Annex 2

Hit rate (q) can be used to determine the validity of wind tunnel experiments with already available and reliable wind tunnel data. As well it can be used to validate the CFD results concerning wind tunnel data.

$$q = \frac{1}{N}\sum_{i=1}^{N} \Delta_i$$

$$\Delta_i = \begin{cases} 1 \; for \; \left|\frac{C_{P,wind\ tunnel} - C_{P,CFD}}{C_{P,wind\ tunnel}}\right| \leq 0.25 \; or \left| C_{P,wind\ tunnel} - C_{P,CFD}\right| \leq w \\ 0 \; else \end{cases}$$

w is the uncetinity interval

## Annex 3

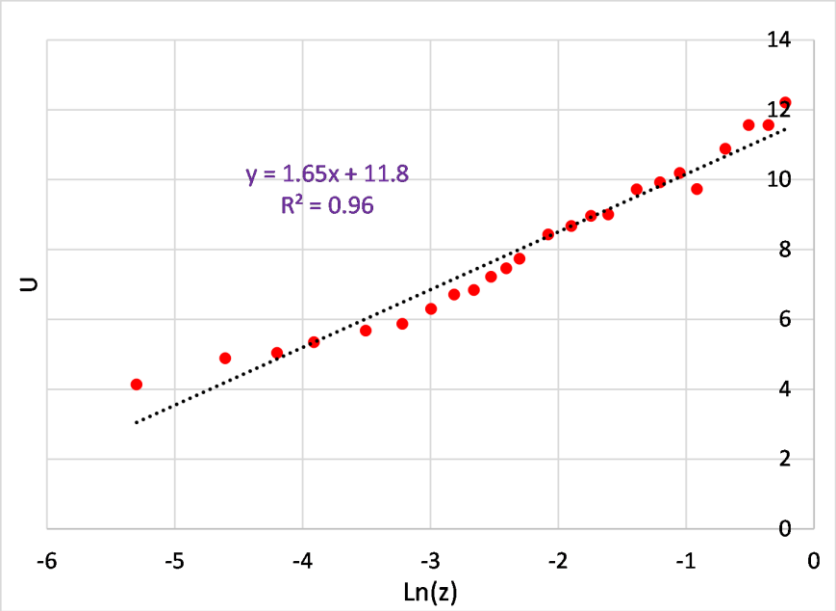


$$\frac{U}{U^*} = \frac{1}{k}\ln\left(\frac{z}{z_o}\right)$$

$$U = \frac{U^*}{k}(\ln(z) - \ln(z_o))$$

$$U = \frac{U^*}{k}\ln(z) - \frac{U^*}{k}\ln(z_o)$$

Considering $y = mx + c$ form:

$$m = \frac{U^*}{k}; c = -\frac{U^*}{k}\ln(z_o)$$

From the gradient:

$$1.65 = \frac{U^*}{0.4}; U^* = 0.66\ m/s$$

From the intercept

$$11.8 = -\frac{0.66}{0.4}\ln(z_o)$$

$$z_o = 0.00079\ m$$

## Annex 4

```
#!/usr/bin/env python
# coding: utf-8
# In[116]:
import numpy as np
import pandas as pd
import os
def import_df(path):
    file = open(path)
    f=[i.strip().split("\t") for i in file.readlines()]
    p,atr=[],["Mean","Std Dev","Minimum","Maximum"]
    for i in f:
        if len(i)==6:p+=[i]
    data = np.array(p)
    df = pd.DataFrame(data[1:,:],columns=data[0,:])
    for i in atr:df[i] = df[i].astype(float)
    return df
D=dict()
f_name=input("Enter the folder Name:")
for dirname, _, filenames in os.walk(f_name):
    for filename in filenames:
        path=os.path.join(dirname, filename)
        p=path.split(" ")
        letter=p[-1][-1]
        for i in p:
```

```
            if  "SujeevaLGableRoof" in i:p1=i.split("_")
        number=p1[-1]
        if letter not in D:
            D[letter]=dict()
        D[letter][number]=import_df(path)
for i in D:
    sum_mean=D[i]['1']['Mean']+0
    sum_Std=D[i]['1']['Std Dev']+0
    sum_min=D[i]['1']['Minimum']+0
    sum_max=D[i]['1']['Maximum']+0
    for j in D[i]:
        if j!='1':
            sum_mean+=D[i][j]['Mean']
            sum_Std+=D[i][j]['Std Dev']
            sum_min+=D[i][j]['Minimum']
            sum_max+=D[i][j]['Maximum']
    F_mean=(sum_mean/sum_mean[0])*(1.52**2)
    F_Std=(sum_Std/sum_mean[0]) *(1.52**2)
    F_min=(sum_min/sum_mean[0]) *(1.52**2)
    F_max=(sum_max/sum_mean[0]) *(1.52**2)
    data = {'Label': np.array(D[i]['1']['Label']),
    new_att=['Label','Mean','Std_Div','Min','Max']
    table= pd.DataFrame(data,columns=new_att)
    table.to_csv(r'I:\wind tunnel calculations\base
case\Results\Final_'+p1[1]+"_"+p1[2]+"_"+i+'.csv', index = False)
```

## Annex 5

```
from scipy.stats import genextreme as gev

# Reading an excel file using Python
import xlrd
# Give the location of the file
loc = ("extreme.xlsx")
def main(rvs):
    shape, loc, scale = gev.fit(rvs)
    return shape, loc, scale
if __name__ == '__main__':
    wb = xlrd.open_workbook(loc)
    sheet = wb.sheet_by_index(0)
        # For row 0 and column 0
    rvs = []
    for i in range(sheet.nrows):
      rvs.append(sheet.cell_value(i, 0))
    shape, loc, scale = main(rvs)
    print(shape, loc, scale)
    l = loc + scale / shape
    xx = np.linspace(l+0.00001, l+0.00001+35, num=71)
    yy = gev.pdf(xx, shape, loc, scale)
    hist, bins = np.histogram(rvs, bins=12, range=(-0.5, 23.5), density=True)
    plt.bar(bins[:-1], hist, width = 2, align='edge')
    plt.plot(xx, yy, 'ro')
    plt.show()
```

## Annex 6

```
#include "udf.h"
#include "mem.h"
#define ustar 0.68
#define z0 0.00079
#define kappa 0.4
#define Cmu 0.042
#define A 0.74
#define B 10.5
#define C1 1.44
#define C2 1.92

DEFINE_PROFILE(inlet_U,t,i)
{
        real x[ND_ND];
        real z;
        face_t f;
        begin_f_loop(f,t)
        {
                F_CENTROID(x,f,t);
                z=x[2];
                F_PROFILE(f,t,i)=(ustar/kappa)*log((z+z0)/z0);;
        }
        end_f_loop(f,t)
}
```

```
DEFINE_PROFILE(inlet_k,t,i)
{
        real x[ND_ND];
        real z;
        face_t f;
        begin_f_loop(f,t)
        {
                F_CENTROID(x,f,t);
                z=x[2];
                F_PROFILE(f,t,i)=sqrt(A*log(z+z0)+B);
        }
        end_f_loop(f,t)
}

DEFINE_PROFILE(inlet_e,t,i)
{
        real x[ND_ND];
        real z;
        face_t f;
        begin_f_loop(f,t)
        {
                F_CENTROID(x,f,t);
                z=x[2];

        F_PROFILE(f,t,i)=((ustar*sqrt(Cmu))/(kappa*(z+z0)))*(sqrt(A*log(z+z0)+B
));
```

```
        }
        end_f_loop(f,t)
}
DEFINE_PRANDTL_D(turb_dissi_prandtl_number,c,t)
{
        real x[ND_ND];
        real z;
        real PTDR;

        C_CENTROID(x,c,t);
        z=x[2];
                PTDR=(kappa*kappa*((-A/2)+(A*log(z+z0)+B)))/(ustar*ustar*(C2-
C1)*(sqrt(A*log(z+z0)+B)));
        return PTDR;
}
DEFINE_PROFILE(Cs_100,t,nv)
{
        face_t f;
        begin_f_loop(f,t)
        {
                F_PROFILE(f,t,nv)=7;
        }
        end_f_loop(f,t)
}
```

## Annex 7

```
from os import getcwd, listdir

from os.path import join, splitext, basename, isfile

from numpy import array, average, mean, std, amin, amax, where, logical_and, zeros

from xlwt import Workbook

def get_data(file_path):

    temp_1d_str_list = []

    temp_1d_float_list = []

    temp_2d_float_list = []

    try:

        _file_name = splitext(basename(file_path))[0]

        with open(file_path, "r") as f:

            for i in range(10):

                line = f.readline()[:-1]  # first 10 lines is metadata

            line = f.readline()[:-1]

            while line != "":

                temp_1d_str_list = line.split('\t')

                for i in temp_1d_str_list:

                    temp_1d_float_list.append(float(i))

                temp_2d_float_list.append(temp_1d_float_list)
```

```
                temp_1d_float_list = []
                line = f.readline()[:-1]
            f.close()
        table = array(temp_2d_float_list)
        del (temp_1d_float_list)
        del (temp_1d_str_list)
        del (temp_2d_float_list)
        return _file_name, table
    except (FileNotFoundError, IOError):
        return "", None
def calc_save_out(table, n, output_file_path):
    row_n_old = table.shape[0]
    col_n_old = table.shape[1]
    row_n_new = (row_n_old // n)
    # check last slice less than n
    have_more = bool((row_n_old % n))
    col_n_new = col_n_old
    workbook = Workbook()
    sheet = workbook.add_sheet("output")
    for i in range(row_n_new):
```

```
        start_i = i * n
        end_i = (i + 1) * n
        for j in range(col_n_new):
            avg_val = average(table[start_i:end_i, j])
            sheet.write(i, j, avg_val)
    if have_more:
        i = row_n_new
        start_i = row_n_new * n
        end_i = row_n_old
        for j in range(col_n_new):
            avg_val = average(table[start_i:end_i, j])
            sheet.write(i, j, avg_val)
    workbook.save(output_file_path)
    return 0
def get_all_files(input_folder):
    return [file for file in listdir(input_folder) if (file.endswith(".ap") and
isfile(join(input_folder, file)))]
def gen_in_file_path(file, input_folder):
    return join(input_folder, file)
def gen_out_file_path(_file, output_folder):
    _output_file = "output_%s" % _file
```

```
    output_file = "%s.xls" % _output_file
    output_file_path = join(output_folder, output_file)
    return output_file_path
def calc_save_out1(table, n, s, output_file_path):
    row_n_old = table.shape[0]
    col_n_old = table.shape[1]
    row_n_new = (row_n_old // n)
    # check last slice less than n
    have_more = bool((row_n_old % n))
    col_n_new = col_n_old
    # for calculate frequencies
    frequencies = {}
    new_table = zeros((row_n_new, col_n_new))
    # get reference column
    ref_col = table[:, 0]
    avg = average(ref_col)
    # divide all values by avg and multiply by 2.31
    k = 2.31 / avg
    table = table * k
    workbook = Workbook()
```

```
sheet = workbook.add_sheet("output")
for i in range(row_n_new):
    start_i = i * n
    end_i = (i + 1) * n
    for j in range(col_n_new):
        avg_val = average(table[start_i:end_i, j])
        new_table[i, j] = avg_val
        sheet.write(i, j, avg_val)
# last row
if have_more:
    i = row_n_new
    start_i = row_n_new * n
    end_i = row_n_old
    for j in range(col_n_new):
        avg_val = average(table[start_i:end_i, j])
        new_table[i, j] = avg_val
        sheet.write(i, j, avg_val)
# get column corosponding to given sensor
sensor_col = new_table[:, s]
mean_val = mean(sensor_col)
```

```
    std_dev = std(sensor_col)
    sheet2 = workbook.add_sheet("frequencies")
    sheet2.write(0, 0, "mean")
    sheet2.write(1, 0, mean_val)
    sheet2.write(0, 1, "standard deviation")
    sheet2.write(1, 1, std_dev)
    sheet2.write(4, 0, "interval")
    sheet2.write(4, 1, "frequency")
    row_offset = 21  # 16 + 5
    for i in range(-16, 16):
        i_lower = i / 2.0
        i_upper = (i + 1) / 2.0
        interval = "%.1f:%.1f" % (i_lower, i_upper)
        row = i + row_offset
        sheet2.write(row, 0, interval)
        lower_limit = i_lower * std_dev + mean_val
        upper_limit = i_upper * std_dev + mean_val
        # get indices of values between the interval
        indices = where(logical_and(sensor_col >= lower_limit, sensor_col <
upper_limit))[0]
        # frequency is the number indices
```

```
        frequency = indices.shape[0]
        sheet2.write(row, 1, frequency)
    workbook.save(output_file_path)


def calc_save_out2(table, n, s, output_file_path):
    row_n_old = table.shape[0]
    col_n_old = table.shape[1]
    row_n_new = (row_n_old // n)
    # check last slice less than n
    have_more = bool((row_n_old % n))
    col_n_new = col_n_old
    # get reference column
    ref_col = table[:, 0]
    avg = average(ref_col)
    # divide all values by avg and multiply by 2.31
    k = 2.31 / avg
    table = table * k
    workbook = Workbook()
    sheet = workbook.add_sheet("output")
```

```
sheet.write(0, 0, "min")
sheet.write(0, 1, "max")
sheet.write(0, 2, "mean")
sheet.write(0, 3, "standard deviation")
for i in range(row_n_new):
    start_i = i * n
    end_i = (i + 1) * n
    min_val = amin(table[start_i:end_i, s])
    max_val = amax(table[start_i:end_i, s])
    mean_val = mean(table[start_i:end_i, s])
    std_dev = std(table[start_i:end_i, s])
    i_ = i + 1
    sheet.write(i_, 0, min_val)
    sheet.write(i_, 1, max_val)
    sheet.write(i_, 2, mean_val)
    sheet.write(i_, 3, std_dev)
# last row
if have_more:
    i = row_n_new
    start_i = row_n_new * n
```

```
        end_i = row_n_old
        min_val = amin(table[start_i:end_i, s])
        max_val = amax(table[start_i:end_i, s])
        mean_val = mean(table[start_i:end_i, s])
        std_dev = std(table[start_i:end_i, s])
        i_ = i + 1
        sheet.write(i_, 0, min_val)
        sheet.write(i_, 1, max_val)
        sheet.write(i_, 2, mean_val)
        sheet.write(i_, 3, std_dev)
    workbook.save(output_file_path)
from tkinter import Tk, Frame, Label, Button, Text, NW, NORMAL, END,
DISABLED, filedialog, Entry
from tkinter.ttk import Combobox
from test_func import get_all_files, gen_in_file_path, get_data, gen_out_file_path,
calc_save_out1, calc_save_out2
import six
# function to get input folder path
def get_in_folder():
    global input_folder
    input_folder = filedialog.askdirectory()
```

```
    if input_folder != "":
        input_folder = input_folder.replace("/", "\\")
        in_path_box.config(state=NORMAL)
        in_path_box.delete(1.0, END)
        in_path_box.insert(END, input_folder)
        in_path_box.config(state=DISABLED)
    return 0
def get_out_folder():
    global output_folder
    output_folder = filedialog.askdirectory()
    if output_folder != "":
        output_folder = output_folder.replace("/", "\\")
        out_path_box.config(state=NORMAL)
        out_path_box.delete(1.0, END)
        out_path_box.insert(END, output_folder)
        out_path_box.config(state=DISABLED)
    return 0


def calculate():
    global n, input_folder, out_path_box
```

```
n = int(n_box.get())
s = int(s_box.get())
if cmb.get() == "Method 1":
    method = 1
elif cmb.get() == "Method 2":
    method = 2
else:
    return
files = get_all_files(input_folder)
done = 0
total = len(files)
if total == 0:
    progress_box.config(state=NORMAL)
    progress_box.insert(END, "Input folder is empty")
    progress_box.config(state=DISABLED)
else:
    for file in files:
        file_path = gen_in_file_path(file, input_folder)
        _file, table = get_data(file_path)
        output_file_path = gen_out_file_path(_file, output_folder)
```

```
            if method == 1:
                calc_save_out1(table, n, s, output_file_path)
            elif method == 2:
                calc_save_out2(table, n, s, output_file_path)
            done += 1
            progress_box.config(state=NORMAL)
            progress_box.insert(END, "Done : (%u/%u) %s\n" % (done, total, file))
            progress_box.config(state=DISABLED)
    return 0
input_folder = ""
output_folder = ""
n = 0
gui = Tk()
gui.resizable(width=False, height=False)
gui.title("Calculator2")
main_form = Frame(gui, width=600, height=500)
main_form.grid(row=0, column=0, sticky='news')
Label(main_form, text="Please select input folder").place(relx=0.015, rely=0.016,
anchor=NW)
Label(main_form, text="Please select output folder").place(relx=0.015, rely=0.12,
anchor=NW)
```

Label(main_form, text="Please enter time step").place(relx=0.015, rely=0.252, anchor=NW)

Label(main_form, text="Please enter sensor number").place(relx=0.376, rely=0.252, anchor=NW)

Label(main_form, text="Please select method").place(relx=0.784, rely=0.252, anchor=NW)

in_path_box = Text(main_form, width=58, height=1)

in_path_box.place(relx=0.02, rely=0.064, anchor=NW)

in_path_box.config(state=NORMAL)

in_path_box.delete(1.0, END)

in_path_box.config(state=DISABLED)

out_path_box = Text(main_form, width=58, height=1)

out_path_box.place(relx=0.02, rely=0.176, anchor=NW)

out_path_box.config(state=NORMAL)

out_path_box.delete(1.0, END)

out_path_box.config(state=DISABLED)

n_box = Entry(gui, bd =5)

n_box.place(relx=0.02, rely=0.31, anchor=NW)

n_box.insert("0", "10")

s_box = Entry(gui, bd =5)

s_box.place(relx=0.38, rely=0.31, anchor=NW)

```
s_box.insert("0", "1")

Button(main_form, text="Browse", width=12, height=2,
command=get_in_folder).place(relx=0.82, rely=0.024, anchor=NW)

Button(main_form, text="Browse", width=12, height=2,
command=get_out_folder).place(relx=0.82, rely=0.136, anchor=NW)

Button(main_form, text="Start", width=12, height=2,
command=calculate).place(relx=0.42, rely=0.39, anchor=NW)

cmb = Combobox(main_form, width="10", values=("Method 1", "Method 2"),
state="readonly")

cmb.place(relx=0.788, rely=0.31, anchor=NW)

cmb.set("Method 1")

progress_box = Text(main_form, width=71, height=12)

progress_box.place(relx=0.02, rely=0.5, anchor=NW)

progress_box.config(state=NORMAL)

progress_box.delete(1.0, END)

progress_box.config(state=DISABLED)

Button(main_form, text="Done", width=12, height=1,
command=gui.quit).place(relx=0.42, rely=0.918, anchor=NW)

gui.mainloop()%
```